2022

Modeling the Tribo-Dynamic Behavior of Roller Contact

Ali Kolivand
Wright State University

MODELING THE TRIBO-DYNAMIC BEHAVIOR OF ROLLER CONTACT

A dissertation submitted in partial fulfillment.

of the requirements for the degree of

Doctor of Philosophy

By

ALI KOLIVAND

Bach., University of Guilan, Iran, 2011

M.S., Azad University (IAU), Iran, 2014

2022

Wright State University

WRIGHT STATE UNIVERSITY
GRADUATE SCHOOL

March 07, 2022

I HEREBY RECOMMEND THAT THE DISSERTATION PREPARED UNDER MY SUPERVISION BY Ali Kolivand ENTITLED **Modeling The Tribo-Dynamic Behavior of Roller Contact**. BE ACCEPTED IN PARTIAL FULFILLMENT OF THE REQUIREMENTS FOR THE DEGREE OF Doctor of Philosophy.

_____
Sheng Li, Ph.D.
Dissertation Director

_____
Ahsan Mian, Ph.D.
Director, Ph.D. in Engineering Program

_____
Barry Milligan, Ph.D.
Vice Provost for Academic Affairs
Dean of the Graduate School

Committee on Final Examination

_____
Sheng Li, Ph.D.

_____
Ahsan Mian, Ph.D.

_____
Joy Gockel, Ph.D.

_____
Harok Bae, Ph.D.

Abstract

Kolivand, Ali. Ph.D., Engineering Ph.D. Program, Department of Mechanical Engineering, Wright State University, 2022. Modeling the Tribo-Dynamic behavior of roller contact.

This study proposes dynamic modeling of lubricated rolling contact and a numerical sub-model for fatigue life prediction of rollers under starved lubrication conditions. Excitation caused by surface defects in rolling disks is numerically calculated and used as a metric in predicting surface pitting failure occurrence. Surface topography of mating surfaces is used as input to the model for determining maximum acceleration, approach velocity, and approach distance of rollers in presence of pits (defects). Resultant bearing force, contacting force versus approach distance are generated and compared for different pit sizes, developing an accurate tool for design purposes. Maximum acceleration and displacement amplitude, bearing force, and contact force are shown to be a direct function of pit size. Further, this study extends on fatigue life prediction of rollers under starved lubrication conditions in which fatigue life is determined by varying tribological conditions: lubrication level, contact pressure, temperature, and surface roughness for different operating conditions.

Table of Contents

List of Figures

Nomenclature

$A_{a_1}^{\max}$	Maximum amplitude of cylinder 1 acceleration
a_1	Acceleration of cylinder 1
a_h	Half Hertzian width
c_1, c_2	Support bearing damping of cylinder 1 and 2
d_P	Pit depth
F_0	Normal force
F_{b1}	Support bearing force of cylinder 1
F_c	Contact force
G	Limit shear modulus
g_0	Curvature gap
h	Film thickness
h_0	Reference film thickness
k_1, k_2	Support bearing stiffness of cylinder 1 and 2
m_1, m_2	Masses of cylinder 1 and 2
n	Shear rate sensitivity coefficient
p	Contact pressure
p_h	Hertzian pressure
R_q	Roughness RMS amplitude
r_1, r_2	Radius of cylinder 1 and 2
S_1, S_2	Surface roughness profiles of cylinder 1 and 2
SR	Slide-to-roll ratio, $SR = (u_1 - u_2)/u_r$

t	Time
u_1, u_2	Surface tangential velocities of cylinder 1 and 2
u_r	Rolling velocity, $u_r = \frac{1}{2}(u_1 + u_2)$
V	Elastic deformation
W	Cylinder width
w_P	Pit width
x	Axis pointing along rolling and sliding direction of contact surfaces
x_1^d, x_2^d	Normal direction displacements of cylinder 1 and 2
x_e	End of EHL computational domain
x_s	Start of EHL computational domain
z	Axis pointing from surface 1 to surface 2 across film thickness
β	Yasuda parameter
η	Lubricant viscosity
η_0	Lubricant viscosity under ambient pressure
ϕ	Flow coefficient
ρ	Lubricant density
ρ_0	Lubricant density under ambient pressure
τ	Shear stress
σ_x	normal stress is x direction
σ_y	normal stress in y direction
σ_{xy}	shear stress in xy plane

σ_a	normal stress amplitude
τ_a	shear stress amplitude
S_b	fatigue strength of material for bending
S_t	fatigue strength of material for torsion
N_f	number of load cycles
$\sigma_{m,\max}$	mean normal stress at plane of max shear stress
S_y	yield strength
EHL	Elasto-Hydrodynamic Lubrication

Acknowledgment

I would like to thank my advisor Dr. Sheng Li for this research opportunity and for his constant support during my Ph.D. program. I appreciate his guidance, advice, and patience throughout the program which was not just limited to my education but also my personal life.

I would like to thank my dissertation committee members Dr. Ahsan Mian, Dr. Joy Gockel, and Dr. Harok Bae, for their constructive input throughout my research and for the time and energy they spent reviewing this work.

I would like to thank my family for their support and encouragement during my entire education.

Finally, special thanks to my wife for her support throughout my Ph.D. program.

Chapter 1. Introduction

1.1 Background and Motivation

Pitting failure and limited fatigue life in rolling elements (Gears, Cams, bearings) in power transmission components are the result of high contact stress and improper lubrication.

Pitting failure is considered a surface failure with different levels. Initial pitting in gears in mesh can be reduced by break-in under low load and speed. It is safe as in most cases it does not progress, rather after break-in time it stops by itself. However, pitting failure can be destructive, in that it continues progressively till the destruction of the surface where over time number of surface pits on the surface becomes more in quantity and larger in size. This case of pitting failure is the result of overloading surfaces in contact.

Different ISO standards provide limits of maximum permissible contact stress to avoid pitting damage and extend gears life. For example, in designing Gear pairs, ISO 6336-2 describes safety values against pitting failure to avoid this phenomenon in gear design.

Pitting depends on contact stress and the number of stress cycles, when occurs creates microlevel dents on the surface. The pitted surface creates unwanted noise, vibration, and surface damage. For components in mesh (gears, cams, bearings), this damage can transmit to other pairs and if not controlled cause the entire system to fail. Rotary components in powertrain systems under load and insufficient lubrication are prone to pitting failure. to detect the existence of surface defects different experimental methods in industry are implemented. Capturing vibration signals from the surface of operating components is a common industry practice, where signals induced by surfaces in contact are recorded with

accelerometers and transformed to the power spectrum of that signal where the impact of each signal can be observed in the frequency domain. Indicating the frequencies caused by pitted surfaces. this practice requires lab equipment and trained individuals to be performed and is expensive. Machine components limits and test equipment limits are other barriers to performing such vibration experiments. Extreme operating conditions are often not possible inside labs as laboratory equipment are limited by operating machines' safeties as well as environmental safety.

High speed/load applications for example, where shaft speed for rotary applications can reach to does not only require expensive equipment but also can cause safety issues. High-speed rolling elements in contact in presence of lubricant generate oil mists, where a micron-size degraded particle of oil cause safety issues if not ventilated properly and disposed of safely, justifying the need for a model that can easily simulate the application under harsh operating conditions without the need to be performed in a lab.

As fatigue life is dependent on many parameters, performing this experiment requires making specimens with different materials, surface finish, treatment, and coatings.

To perform life experiments on components, fatigue tester machines that are equipped with servo-hydraulic machines are often being used. this experiment requires a high number of cycles essentially when the load is not high. through-hardened steels normally are tested to 10^6 million cycles, which under low speed takes a long time to perform.

In addition, fatigue life experiments data requires replications. to statistically achieve a confidence level for parts fatigue life, a full factorial test matrix is performed on specimens. after performing regression, final statistical data are reported with R-Squared (R^2) values,

with high values indicating low variation between samples. A high number of required replications (above 20) to generate certainly in data, adds to the expenses of performing such an experiment, justifying the need for a numerical model that can limit the number of replications.

When it comes to bearing life calculations, the impact of the lubrication method is taken into account by introducing factors in equations for different types of bearings. The load capacity of bearings is based on maximum contact stress, calculated between roller and bearings inner race. Unless sophisticated programs by different manufacturers are used, dynamic equivalent reference load for different ladings is not accurately formulated in ISO standards, making bearing life calculations not accurate.

The complexity of governing equations between rolling components and the inclusion of oil in equations has forced engineers in the industry to experimentally predict fatigue life.

For loss calculations where the lubricant film thickness is important at different speeds and loads, these parameters are often experimentally regressed and estimated.

Experimental equations are often inaccurate and fail to provide good results for small changes in input variables as they are mainly approximated by statistical methods and experimental data.

The lack of numerical solution of motion under lubrication conditions in contacting rollers in the literature on one hand and the importance of the actual contact stress calculation on the other hand justifies the reason for the development of a numerical approach that accurately predicts the magnitude of vibration amplitudes caused by surface defects which indicates the presence of surface pits on rolling elements and actual values of pressure

distribution in contact zone to be used for fatigue life prediction justify the need for the modeling of rollers contact.

1.2 Literature Review

The dynamic behavior of rolling components in service is impacted by different parameters. Parallel and angular Misalignment in coupled rotors create different vibration spectra [1] .intentional modification on rolling elements generates specific dynamic behavior which often includes noise[2]. Modified gear surfaces are associated with dynamic transmission error which has close relation with the excitation of the gear system [3]. time-varying mesh stiffness in the gears system generates different sub-harmonic resonances [4]. Damping in spur gear pairs caused by lubrication film creates different dynamic models for all lubrication regimes [5]. The thermal effect as a result of lubrication inlet flow, input torque, and surface roughness changes the dynamic response of gear pairs [6][7]. the dynamic of gear train in automotive applications is extensively impacted by speed [8]. High service load and harsh operating conditions in gearbox systems cause damaging faults which in turn generates specific dynamic response [9]. Tiny defects on the bearing surfaces can lead to high load and often component failure [10].

As a common industry practice, vibrational signals are used to predict, analyze, and prevent surface failure. Any defects on the surface level induce vibration signals which can be recorded using data acquisition devices. Common surface defects are results of scuffing in high speed/ temperature applications, inconsistent machining, cutting tool faults, etc. utilizing vibrational measurement together with oil-debris data, Lewicki et al. [11] evaluated their effectiveness in pitting failure detection. A statistical metric that is the ratio of the fourth statistical moment to the square of the average variance (of the vibration data) was proposed as a failure condition indicator. Employing helical gear pairs whose tooth surfaces were pre-dented to simulate pitted contact surfaces, Ozturk et al. [12] measured

dynamic signals and analyzed data using the main frequency of the scalogram. Sung et al. [13] and Yoshida et al. [14] examined the dynamic behavior measured from pitted gear contacts, where the wavelet transform technique was shown to be a promising analyzing approach for the diagnosis of tooth surface failure. Adopting different signal analysis techniques, Elasha et al.[15] investigated the vibration of worn gear contacts with the presence of surface defects. The study pointed to the importance of the direction of vibration measurement. Besides the above gearing applications, dynamic signals have also been used in twin disks type of fatigue tests [16] to detect pitting failure. For this type of experimental setup where two rollers roll against each other under a normal force to simulate contact of gears or bearings, accelerometers are frequently implemented to capture any sudden acceleration jump, which indicated the creation of fatigue pits. The test is then stopped automatically according to such a signal. Given the important role of the dynamic behavior of rolling mechanical elements in rolling contact fatigue, this study aims at developing a tribo-dynamic model for lubricated line contacts, with a focus on excitation created by pit/defects.

Regarding the modeling of surface pits induced dynamic behavior, many studies paid particular attention to the contacts of gears. Choy et al. [17] investigated the vibration of gear transmission systems faults, by incorporating the impacts of pits and wear on dynamic responses through the phase and magnitude change in gear mesh stiffness. How these changes arrived however was not clearly given. Chaari et al. [18] modeled a surface pit as a rectangular indentation. The tooth geometry change due to the assumed indentation shape was included in the gear mesh stiffness calculation. Instead of a rectangular shape, Liang et al. [19] adopted a circular one for the surface pit description. Where the impact of the pit

on variation was included also included through a time-varying mesh stiffness excitation. The occurrence of surface pits directly affects contact compliance [13]. thus, the modeling approach adopted by the above studies is legitimate. However, the way the mesh stiffness of contact was calculated [18][19] was through rough approximation, and far from rigorous. the contact between pitted cylinders with a parallel axis is no longer a Hertzian contact. The relationship between normal load and indentation depth of Hertzian contact doesn't apply for pitted cases, especially for big pit sizes which occupy a considerable portion of the normal Hertzian zone. In addition, the tribo-dynamic description of the lubricated contact, i.e. The interactions between tribological behavior and dynamic behavior [5][6][20][21] were excluded in all these works.

pitting failure itself is initiated from fatigue cracks which is mainly the result of high near-surface stress dictated by tribological behavior of the contacting surfaces [22] [23], [24] Rolling contact fatigue (RCL) is therefore the main purpose of this computation. however, the crack propagation is not in the scope of this study. Surface fatigue crack is influenced by different parameters including roughness, lubrication properties, and operating condition. Surface roughness for example plays an essential role in near-surface stress increase as asperity contact near the surface of metal components can substantially increase stress which in turn will reduce fatigue life and initiate cracks on the surface. This phenomenon as explained in [25] is more on rough gear surfaces that are the results of finishing with higher surface roughness in methods like griding and shaving. Asperity contacts along with the lubrication effect have been the subject of many studies in which electrohydrodynamic simulations of contact were carried out. Zhu et al [26] provide a pitting life prediction model in which von misses subsurface stress is used to estimate

rolling bearing and gears fatigue life for line contact components. Results are compared with experimental data for 16 sets of gears. In addition to line contact stress models, there are models for points contact simulation as well, the essential purpose of points contact modeling is mainly for the inclusion of surface modification of gears flank to shift contact pattern in middle areas avoiding edge contact. Epstein et al [27] studied the effect of surface topography on the rough surface by numerical analysis of mixed lubrication for rolling/sliding conditions in which contact pressure is calculated and used for subsurface stress calculation. For the transient condition where pressure, velocity, surface roughness, and velocities become time depend Li et al. [22] develops a transient mixed hydrodynamic model that is specifically for gear contact in which high-stress concentration as a result of intermittent metal to metal contact which is the case in highly loaded gears occurs, the model also provides a subsurface stress formulation in its sub models[28]. Li and Anisetti [21] extended this model to tribo-dynamic behavior of Spur gears where dynamic of gears in mesh bridges to Tribological behavior at contact zone where pressure gradient numerically solved for each time instant by rolling contacting gears iteratively. This model provides the connection between input torque, speed, lubrication level to pressure, film thickness, and contact pressure and subsequently fatigue life on the surface and subsurface of Spur gears in mesh. all of the aforementioned studies focus on surface roughness effect on fatigue life rolling/sliding components and try to model the effect of surface asperities contact which in resultant multiaxial stress field determination.

On surface and subsurface stress field then is used to determine maximum stress using von misses method and fatigue life for different materials as each material has a specific S-N curve.

In view of provided literature, lubrication level is missing, all studies excluding experimental studies develop models assuming the contact zone is fully flooded, and lubricant is provided enough that rolling/sliding surfaces separate and stay in the hydrodynamic zone. However, in cases where the amount of lubrication is not enough due to lubricant inlet blockage, debris creating a clog, leaking in the system, and causing lubricant loss the studies are not covering the fatigue life and are mainly focused on wear, scuffing prediction, and starvation impact on friction. Riggs et [29] investigates the scuffing resistance of gears contact in helicopter application under starved lubrication condition where the amount of lubricant due to unexpected event reduces substantially to the level that EHL condition no longer exists, using a ball on disk tribometer to experiment with the effect of insufficient lubrication in point contact condition in similar speed as gears of application experience. Enthoven et al [30] implement the use of infrared light for measurement of temperature and viscosity in contact point of ball on disk tribometer, results explain the importance of debris build up in the contact zone which consequently blocks the lubrication inlet to the contact zone and rapid scuffing happens, and claims the temperature increase is the subsequent result of inlet oil blockage caused by the debris. Ali et al [31] develops an analytical and experimental method using the ball on disk tribology set up to measure friction coefficient under fully flooded conditions and starved lubrication, the effect of artificially-produced shallow micro-dents on top of contacting surfaces on reduction of friction coefficient was investigated under staved conditions. Lewis et al [32] use a twin disk tribology set up to investigate the effect of different grease lubricity on railway curves where starvation of lubricant leads to a higher wear rate. when it comes to scuffing at macro level size, studies in the literature are sparse and are mostly experimental.

Querlioz et al [33] use the twin disks method to experiment investigate the fatigue life rolling components in contact under starved lubrication conditions, the article states the fact that lubrication level in the industry often is unknown and starvation in many applications is the case. In first part covers the lubrication supply, operating condition to traction coefficients, and in the second part fatigue measurement is presented for different lubrication flow rates and shows the severity of reduction in fatigue life under starved lubrication conditions. In the experiment surfaces if the specimens were intentionally pre-dented to accelerate the macro pitting failure. Addressing the effect of starvation and surface roughness as two important parameters reducing fatigue life, Labiau et al [34] utilizes an analytical method to investigate the effect of these parameters on pressure increase as a function of sinusoidal waviness surface profile and contact condition. The lack a of physics-based model the in the literature regarding starvation and its effect on fatigue life is the main goal of the second phase of this study, where efforts are devoted to the physical and computational description, and examination, of starved lubrication effect on surface crack nucleation for line contacts. To model the tribological behavior between two surfaces that roll against each other with insufficient lubricant supply (starvation), a group of early works assumed perfectly smooth surfaces and excluded temperature variations across EHL conjunctions. Hamrock et al [35] provide an equation for lubrication film thickness for point contact, in which the solution covers different speeds, loads, and explicitly which was varied from one indication point contact to eight, approaching line contact. However, this is the result of fully flooded conditions. In regards to non-Newtonian fluid under starved lubrication conditions, Yang et al [36] provide a model in which the lubrication film thickness for line contact condition for the EHL model was

calculated. According to the study, if the position of the oil-air meniscus is given as input the effective layer of lubricant can be solved, using a similar method if the effective layer of lubricant on a solid surface is given, the computation can find the position of the oil-air meniscus can be calculated. In this study flash temperature for components in line-contact conditions was calculated under starved lubrication conditions using a modified mixed lubrication model, Pu et al [37] include the effect of surface roughness under elliptical contact shape, entraining velocity, starvation, and cavitation in his model. It provides a comprehensive analysis of the lubricant supply on starvation, cavitation, mixed EHL characteristics, and flash temperature. Analysis proves that inlet oil reduction (starvation) leads to film thickness reduction. Also, starvation leads to the rising of flash temperature in contacting surface topographies. Recently Li et al [38] proposed a mixed elastohydrodynamic model in which the effect of starvation of lubricant inlet on flash temperature is investigated. The effect of inlet oil starvation was incorporated by introducing film fraction parameters in the Reynold equation to quantify the severity of starvation for line contact conditions. The model effectively provides flash temperature calculations based on inlet oil supply under different operating conditions These realistic lubricant property descriptions allow the proper and accurate prediction of flash temperature, which dictates the initiation of scuffing failure for high sliding and high-pressure gear contacts. Elrod [39] propose a computational method that is capable of automatically taking care of cavitation regions in lubricated bearing contact. The objective is to reduce computations' complexity of governing equation lubricated contacts considering cavitation. In this work, the generalized Newtonian Reynolds equation with a cavitation algorithm incorporated, proposed by Li and Masse [38] is implemented in

conjunction with an asperity contact equation and a film thickness equation to describe the surface tribological behavior. The cavitation algorithm adopted doesn't require the input of meniscus location, which is usually unknown and difficult to measure. The normal contact pressure and tangential shear distributions yielded from the tribological formulation are used to evaluate the stress fields on and below the contact surface, assuming a half-space contact problem. The stress means and amplitudes are then used to assess the fatigue damage according to a multi-axial fatigue criterion. In this study, the thermal behavior of the lubricated contact, which is commonly included for scuffing failure prediction [38] [20], [40], [41] is excluded. It is also assumed there always exists a thin molecular boundary lubrication film within local asperity contact areas. The associated boundary lubrication friction coefficient is considered to be constant and independent of the starvation condition. The crack propagation after the nucleation of the surface-breaking crack is out of the scope of the current study. Using the model developed, a parametric simulation is performed to show fatigue life variations with starvation severity, surface roughness amplitude, lubricant viscosity (by varying lubricant temperature), and normal load. It is, unexpectedly and very interestingly, observed higher fluid viscosity, which promotes fatigue performance under fully flooded lubrication conditions [24], actually leads to reduced fatigue life when lubrication is sufficiently starved.

It is noted that the frictional heat of contact may become significant under high sliding and heavy loading conditions. The resultant lubricant temperature rise can reduce viscosity and affect power loss[42].on the other aspect, the extreme flash temperature under thermal conditions may exceed critical magnitude, and lead to scuffing failure[20]. neither loss nor scuffing failure is the focus of this study. Thus, the contact pair is considered to operate

under moderate sliding and loading conditions, allowing the exclusion of thermal description. The major excitation considered in this study is a surface pit present on one of the cylinders. Roughness profile variations are also included. Other excitations are out of the scope of the current work. The fluctuation of the contact force caused by the surface pit is used to determine the dynamic displacements and velocities of the contact bodies. These responses, in turn, affect the thickness and flow of the lubrication film, impacting the contact pressure and consequently the time-varying contact force required in the dynamic analysis. By varying the dimension of the surface pit, a set of simulations are performed. It is shown the polished surface roughness profile adopted in this study hardly introduces any vibration. Once the pit is produced, the acceleration signal of the contact body elevates sharply as the pit size grows, pointing to an easy-to-use and effective method for pitting failure detection. Additionally, a comparison between the Tribo-Dynamic simulation and its quasi-static counterpart is performed to show the important role of dynamic responses in the tribological behavior of a contact pair.

Therefore, starting with a generic line contact problem, this study proposes a Tribo-Dynamic model that links the dynamic vibration of a cylinder pair with its lubricated contact behavior at the first stage. And further, extend to fatigue life prediction of rollers under starved lubrication condition as a sub-model for already solved lubricated line contact condition.

1.3 Dissertation Scope and Goals

At the first stage of this study Tribo-Dynamic model of contacting roller is provided. The model includes the lubrication effect in the dynamic behavior of contacting rollers. The numerical solution of the Reynolds equation with time-varying load, speed, and the surface roughness of rollers under line contact conditions for each time instant is linked to the dynamic response of rollers' contact. contact force, maximum acceleration amplitude, approach velocity, and bearing loads are numerically calculated. With the inclusion of surface pits in contacting bodies, the effect of pits size under diff rent speed and load on vibrations response of rollers are investigated.

In the second phase, a sub-model is introduced to use already solved Reynold's equation of lubricated rollers to estimate the fatigue life of contacting bodies. Pressure distribution is calculated and on surface and undersurface stress field is obtained for different lubrication levels and surface roughness. In this sub-model, lubrication level (ranging from starved to flooded condition) is implemented through a **lubrication fraction term** by allocating numbers from 0 to 1. And the effect of surface roughness as a major role player in the fatigue life of contacting bodies is taken into account.

the objectives are summarized as:

1. Tribo-Dynamic modeling of contacting rollers. Solving lubrication equation (Reynolds) for contacting rollers in motion (dynamic motion of rollers).

2. Inclusion of surface pits on rolling bodies and investigating the effect of surface defects on dynamic response, bearing force, contact force, approach velocity, and approach distance.

3. Calculation of pressure distribution in contact zone using developed Tribo-Dynamic model and comparing with the quasi-static model.

4. Introducing a new term in Reynold's equation to simulate starvation in line contact conditions and capturing the effect of starvation on average lubrication film thickness.

5. On surface and subsurface stress field is obtained using pressure distribution between contacting bodies for each instant. And used to estimate the fatigue life of contacting bodies.

6. Average lubrication film thickness is obtained under different starvation severity, pressure, and surface roughness. And used as a metric to explain starvation levels.

1.4 Dissertation Outline

Chapter 2:

Outlining the numerical method for modeling Tribo-Dynamic behavior of lubricated roller. The lubrication equation is solved iteratively in conjunction with the dynamic equation of motions for lubricated rollers. Introducing surface defects in form of surface pits, resultant approach velocity, approach distance, time-varying pressure distribution, contact force, bearing force, and maximum excitation amplitude are calculated and plotted within the contact zone.

Chapter 3:

Covers fatigue life modeling of lubricated rollers. Introducing a new term to simulate starvation in contacting rollers and obtaining resultant contact pressure, average lubrication film thickness, friction coefficient, fatigue life under two-level of Hertzian contact pressure and temperature. The simulation consists of a test matrix with varying parameters of temperature, Hertzian contact pressure, roughness, and supplied lubrication level.

Chapter 4:

Results of numerical simulation for dynamic response evaluation and fatigue life are provided and discussed in detail.

Chapter 5:

Future Work and recommendations regarding utilizing the Tribo-Dynamic method in surface defects monitoring and fatigue life model implementation for improvement of roller elements' life in different applications are provided.

Chapter 2. Theoretical modeling of rollers

2.1 Overview

This chapter illustrates the governing equations of motion and their connection to tribological behavior of contacting surface in presence of pits on the disk's surface.

Using the discretization method, each term the of Reynolds equation is divided into ij terms for finite difference calculation over control volume. impact of lubrication is introduced as a term with a force nature F_C into rollers equation of motion. at each iteration, approach velocity and approach distance calculated from the dynamic simulation is fed into the EHL model and calculated contact force is used to find the next approach velocity and distance.

The numerical solution of the coupled equation of motion and lubrication is the so-called Tribo-Dynamic model, which in response to bearing force, approach distance of rolling disks, and acceleration of rollers are calculated and plotted within the contact zone.

In addition, the correlation of dynamic response with pit size is demonstrated through increasing pit sizes incrementally under specific load and speed.

The model becomes the building block of the next chapter, where the fatigue life of rollers under different starvation levels is numerically calculated.

2.2 Dynamic of contacting rollers

(a)

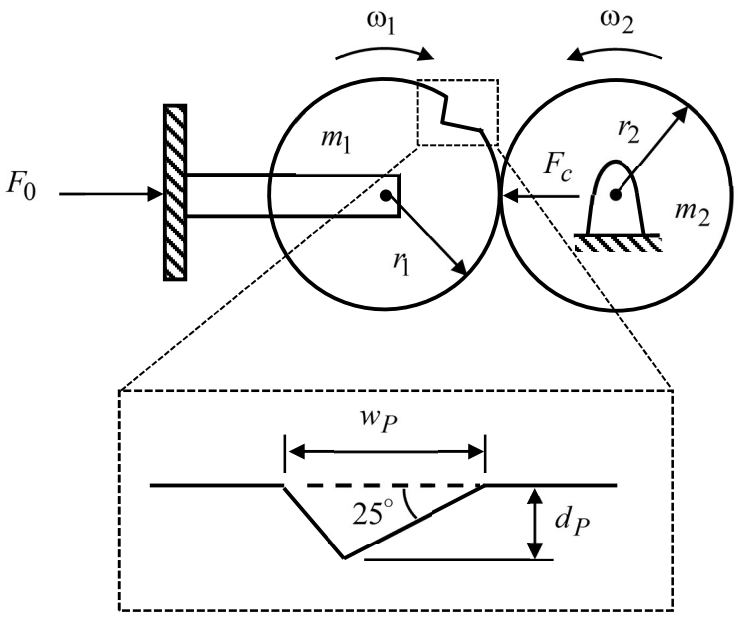

(b)

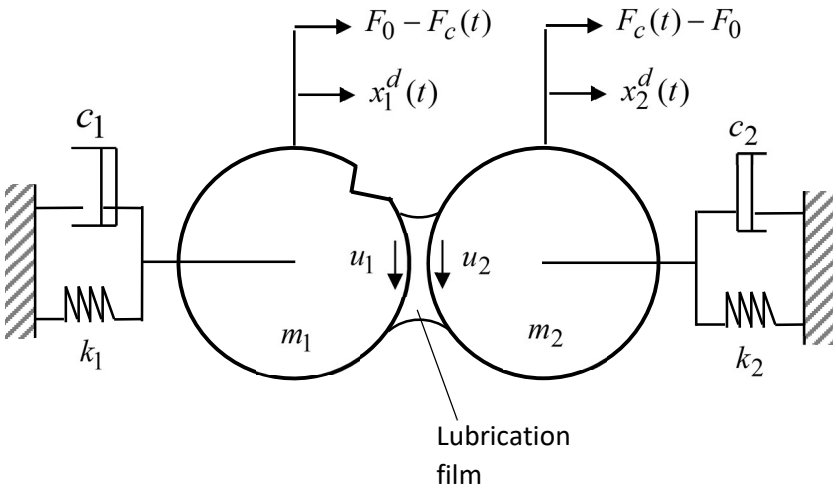

Figure 2-1 Tribo-Dynamic model of line contact formed by two cylinders.

As Figure 2-1 (a) displays the contact between two cylinders, whose masses are m_1 and m_2 , and radii are r_1 and r_2 . A normal force, F_0 , pushes cylinder 1 to come into contact with cylinder 2, producing a contact force, F_c , at the contact interface. A pit is implemented on cylinder 1. According to experimental observations, surface-breaking fatigue cracks commonly propagate at a shallow angle to the surface, ranging from 15^o to 30^o Therefore, at 25^0 propagation angle as shown in Figure 2-1 (a) is adopted for the pit. The other dimensions that define the pit geometry are width, w_p , and depth, d_p , which are depicted in Figure 2-1 (a) as well. For the dynamic description of the two cylinders as illustrated in Figure 2-1 (b) the stiffness and damping of the support bearings are included as k_1 and c_1 for cylinder 1, and k_2 and c_2 for cylinder 2. The displacements of the cylinders along the normal direction of the contact are denoted as x_1^d and x_2^d , respectively. The fluctuation of the contact force, owing to the presence of the pit, serves as the periodic excitation to the cylinder vibrations, which in turn impact the tribological behavior within the contact zone.

Because the contact pressure within the lubricated contact zone dictates $F_c(t)$, a mutual interaction between the tribological behavior and the dynamic response is established. The Tribo-Dynamic description of this contact is formulated as follows.

Considering a two-degree-of-freedom system, the equations of motion of the cylinders in Figure 2-1 are written as:

$$\begin{aligned} m_1\ddot{x}_1^d + c_1\dot{x}_1^d + k_1x_1^d &= F_0 - F_c \\ m_2\ddot{x}_2^d + c_2\dot{x}_2^d + k_2x_2^d &= F_c - F_0 \end{aligned} \tag{1}$$

where the time-varying contact force is dependent on the pressure distribution within the lubricated contact zone, p , as

$$F_c = W\int_{x_x}^{x_e} p(x,t)dx \tag{2}$$

In Eq. (2) x represents the coordinate axis pointing along the rolling and sliding direction of the contact surfaces. x_s and x_e are the start and end of the Elastohydrodynamic (EHL) lubrication (EHL) computational domain; t is time, and W is the axial direction width of the cylinders. This contact pressure is coupled with lubrication film thickness, h , through the one-dimensional generalized Newtonian Reynolds equations

$$\frac{\partial}{\partial x}\left(\phi\frac{\partial p}{\partial x}\right) = u_r\frac{\partial(\rho h)}{\partial x} + \frac{\partial(\rho h)}{\partial t} \tag{3}$$

where, u_r is rolling velocity and defined as the average of tangential velocities of surface 1, u_1, and surface 2, u_2 Figure 2-1 (b); and ρ is lubricant density, whose dependence on pressure is included as

$$\rho = \rho_0\frac{1+\lambda_1 p}{1+\lambda_2 p} \tag{4}$$

The two constants involved in the above equation have the values of $\lambda_1 = 2.266GPa^{-1}$ and $\lambda_2 = 1.683GPa^{-1}$, and represent fluid density under ambient pressure.

Due to the rotational motion of the contact bodies, the surface topography (roughness, defects, fatigue pits, etc.) within the EHL zone is transient. The variations of the surface

profiles of body 1, $s_1(x,t)$, and body 2, $s_2(x,t)$ are included through the film thickness distribution as

$$h = h_0 + g_0 + V - (s_1 - s_2) - \left(x_1^d - x_2^d\right) \tag{5}$$

where h_0 is a reference film thickness, describing the initial rigid body approach of the two surfaces; g_0 is curvature gap between the un-deformed surfaces; V denotes total elastic deformation of the two surfaces due to the normal load applied, and has the expression for a two-dimensional contact of

$$V = \int_{x_s}^{x_e} K(x - x')p(x',t)\,dx' \tag{6}$$

with *K* representing a load influence function. Unlike quasi-static EHL modeling or Tribo-Dynamic EHL studies that consider relative surface motions only in the tangential direction, this study includes the normal direction approach- displacement of the contact bodies, i.e. the relative displacement of the two cylinders, through the term of $\left(x_1^d - x_2^d\right)$ in the lubrication film thickness description of the equation (5). In addition, since the squeeze term in the equation (3) involves the derivative of the film thickness for time as

$$\frac{\partial(\rho h)}{\partial(t)} = \rho\frac{\partial h}{\partial t} + h\frac{\partial \rho}{\partial t} \tag{7}$$

And

$$\frac{\partial h}{\partial t} = \dot{V} - (S_1 + S_2) - \left(\dot{x}_1^d - \dot{x}_2^d\right) \tag{8}$$

the dynamic approach-velocity of the contact pair, $\left(\dot{x}_1^d - \dot{x}_2^d\right)$, is involved in the lubrication fluid flow governed by the Reynolds equation. To include any non-Newtonian effect when sliding is high, for instance, contacts in addendum or dedendum areas away from pitch line of gear teeth, a flow coefficient, ϕ, in the form of

$$\phi = \frac{\rho h^3}{\eta}\frac{1}{\hat{p}_x}\int_h \hat{z}\hat{\tau} f\left(\hat{\tau}\right) dz \tag{9}$$

is incorporated in the equation (3). Here, $\hat{p}_x$ is a dimensionless pressure gradient along the x direction and is written as

$$\hat{p}_x = \frac{h}{G}\frac{\partial p}{\partial x} \tag{10}$$

where G is lubricant Newtonian limit shear modulus. Regarding the other parameters in Eq. (9), $\hat{z} = \frac{z}{h}$, representing dimensionless coordinate axis that points from surface 1 to surface 2 along the film thickness direction; and η is lubricant low-shear viscosity, whose dependence on pressure can be described as

$$\eta = \begin{cases} \eta_0 \exp\left[\alpha_1 p\right], & p \le p_a \\ \eta_0 \exp\left[B_0 + B_1 p + B_2 p^2 + B_3 p^3\right], & p_a \le p \le p_b \\ \eta_0 \exp\left[\alpha_1 p_t + \alpha_2\left(p - p_t\right)\right], & p \ge p_b \end{cases} \tag{11}$$

In this equation, η_0 is viscosity under ambient pressure; α_1 and α_2 are pressure-viscosity coefficients; p_a, p_b and p_t are threshold pressure values defining low, high, and transition

pressure ranges; and $B_j\ (j=0,1,2,3)$ are constants that are used to enforce the continuity of both η and its gradient with respect to pressure at $p=p_a$ and $p=p_b$. Lastly, in Eq.(9), the dimensionless shear stress $\hat{\tau}=\frac{\tau}{G}$, and the rheological function $f(\hat{\tau})$ was experimentally characterized to take the form of

$$f(\hat{\tau})=\left(1+\left|\hat{\tau}\right|^{\beta}\right)^{\frac{1-n}{\beta n}} \tag{12}$$

where n is shear rate sensitivity coefficient, and β is referred to as Yasuda parameter.

For many rolling mechanical elements, such as gears, surface roughness is usually significant, resulting in frequent asperity interactions within the EHL conjunction. When local asperity contacts take place, boundary lubrication film thickness is assumed to be constant, such that the film thickness gradient along the *x* direction becomes zero, i.e.

$$\frac{\partial h}{\partial x}=0 \tag{13}$$

Eqs.(3) and (13) together govern the mixed EHL behavior of the contact.

For the computational simulation of the Tribo-Dynamic behavior, the contact is first assumed to be operating under a quasi-static condition, with the cylinder dynamic displacements and dynamic velocities both setting at zero, i.e., $x_i^d = 0$ and $\dot{x}_i^d = 0$ (i = 1,2), as illustrated in Figure 2-2. During this quasi-static stage, no surface pit is applied. Utilizing (13) and the equilibrium equation of

$$F_0 = W\int_{x_s}^{x_e} p(x,t) \tag{14}$$

which enforces the balance between the applied normal force and the mixed EHL pressure, the reference film thickness, h_0, in Eq. (5) is determined and maintained at this value throughout the Tribo-Dynamic analysis that follows. Any further rigid body approach due to the dynamic vibration is implemented through the approach-displacement term of, $\left(x_1^d - x_2^d\right)$. Under the dynamic condition, the EHL simulation drops the equilibrium equation of Eq. (14) to allow the fluctuation of the contact force, F_c, which is evaluated according to Eq. (2) . With F_c provided by the EHL solution, the equation of motion Eq (1) is solved for the dynamic responses. The updated approach-displacement, $\left(x_1^d - x_2^d\right)$, and approach-velocity, $\left(\dot{x}_1^d - \dot{x}_2^d\right)$, are then fed back into the EHL simulation for the solution at the next time instant. The discretization and linearization of the EHL governing equations are described in 2.3. A Fortran PDE solver is utilized to handle the dynamic governing equation.

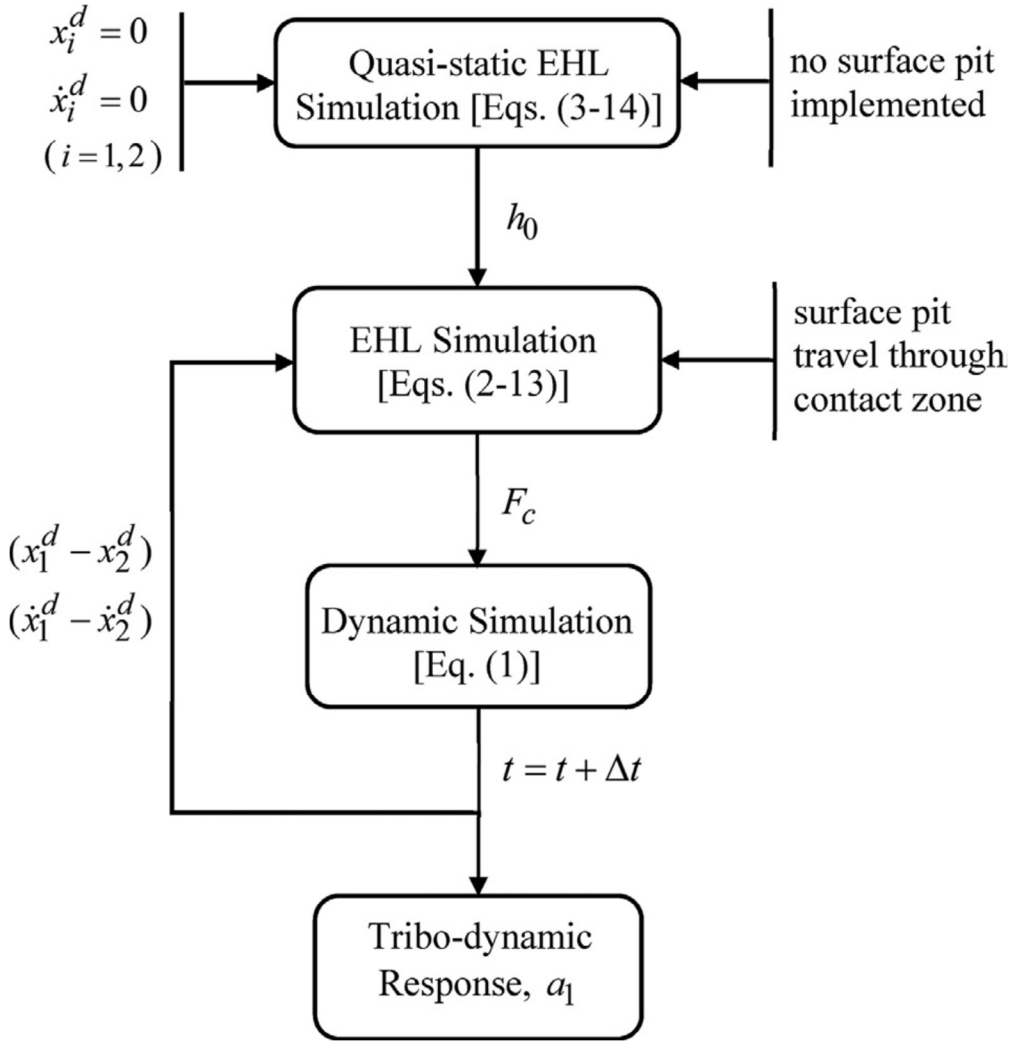

Figure 2-2 Modeling methodology for Tribo-Dynamic line contacts.

2.3 Discretization

As shown in Eq (11) pressure and viscosity terms are exponentially related, in addition to this fact nonlinear behavior of lubricant makes the equation (3) strongly nonlinear. the approach for converging this equation is discretization methods.

Figure 3 is the 2D computational domain which is defined by the size of the Hertzian contact zone $-1.875a \le x \le 1.25a$ and $-1.5b \le y \le 1.5b$, with 2a and 2b length and width of the Hertzian contact area in the x and y direction[43]. for capturing the surface topography effect, the control volume in the x and y directions is divided into N_x in x direction and N_y in y direction total $N = N_x N_y$ respectively. At each time instant t_n, lubricant film thickness, viscosity, density, pressure, and shear stress are assumed to be uniform inside each cell ij.

Using the second-order central difference, the Poiseuille terms, and using the first-order backward difference the Couette term are discretized[44]–[48].

Having the entire contact volume boundaries enclosed $w_1 - w_4$, the pressure flow in x direction is discretized as follows [49]

$$\frac{\partial p}{\partial x}\left(\phi \frac{\partial p}{\partial x}\right) = \frac{1}{x}\left[\phi_{w3}\left(\frac{\partial p}{\partial x}\right)_{w3} - \phi_{w1}\left(\frac{\partial p}{\partial x}\right)_{w1}\right] \tag{15}$$

The pressure gradient and flow coefficient approximated as

$$\left(\frac{dp}{dx}\right)_{w1} = \frac{p_{ij,t_n} - p_{(i-1)j,t_n}}{\Delta x} \tag{16}$$

$$\left(\frac{dp}{dx}\right)_{w3} = \frac{p_{(i+1)j,t_n} - p_{ij,t_n}}{\Delta x} \tag{17}$$

$$\phi_{w_1} = \frac{1}{2}\left[\phi_{x_{(i-1)j,t_n}} + \phi_{x_{ij,t_n}}\right] \tag{18}$$

$$\phi_{w_3} = \frac{1}{2}\left[\phi_{x_{ij,t_n}} + \phi_{x_{(i+1)j,t_n}}\right] \tag{19}$$

The Couette term can be written

$$\frac{\partial}{\partial x}(\rho h) = h\frac{\partial \rho}{\partial p}\frac{\partial p}{\partial x} + \rho\frac{\partial h}{\partial x} \tag{20}$$

The gradient of pressure ($\frac{\partial p}{\partial x}$)can be approximated using backward difference

$$\frac{\partial p}{\partial x} = \frac{p_{ij,t_n} - p_{(i-1)j,t_n}}{\Delta x} \tag{21}$$

And gradient of h($\frac{\partial h}{\partial x}$) in the same manner can be approximated by

$$\frac{\partial h}{\partial x} = \frac{h_{ij,t_n} - h_{(i-1)j,t_n}}{\Delta x} \tag{22}$$

pressure gradient at control volume boundary (w_1) in equation and grid cell center ij take the same form, however, these values are calculated with different distances and are different, especially for rough surface contact.

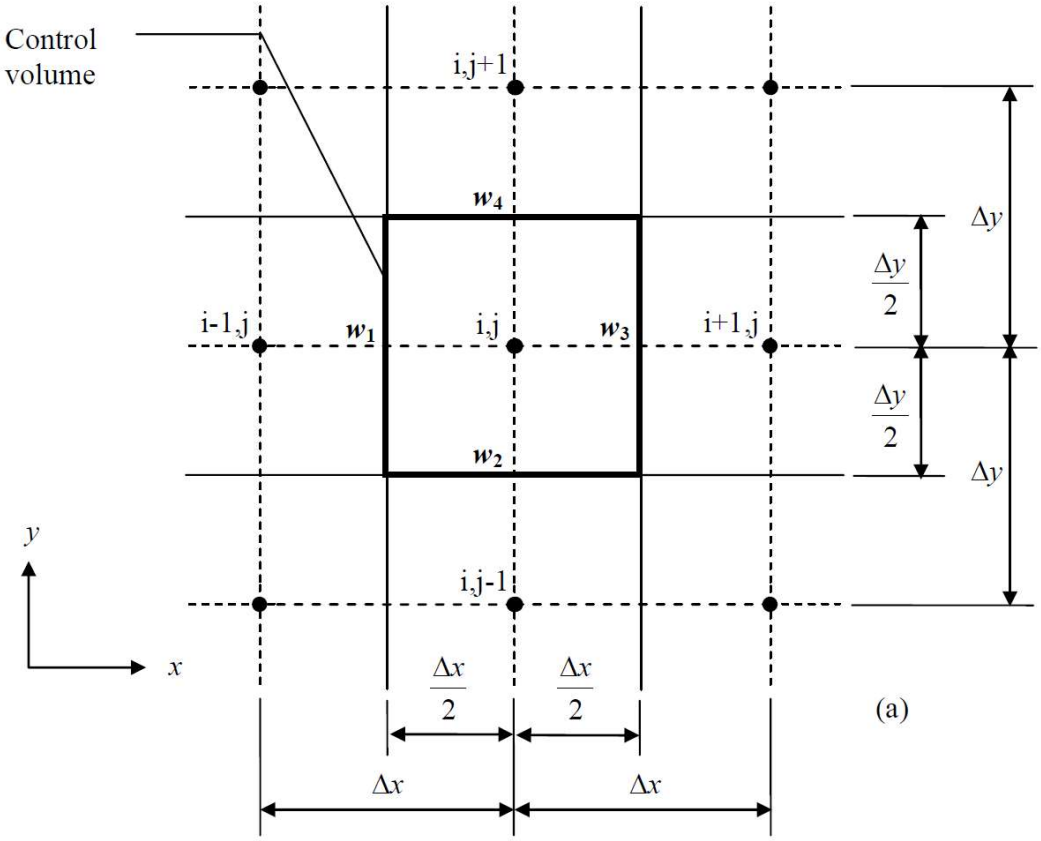

Figure 3 Control volume in the conventional discretization method[49]

Chapter 3. Fatigue life modeling.

3.1 Overview

Extending on the Tribo-Dynamic model, this sub-model is to provide a numerical approach to estimating the fatigue life of rollers in line contact lubrication, where starvation is of importance. A new parameter of lubrication film fraction is introduced to simulate starvation by limiting lubricant supply. Ranging from $0-1$, these parameters forces the lubrication model to starve or fully flood the contacting bodies. Numerically calculated pressure and shear stress under different operating conditions are used in the stress equation for the calculation of maximum shear and normal stress.

By varying lubricant viscosity (temperature), contact pressure, surface roughness, and inlet oil supply value, a test matrix is developed. Resultants are average lubrication film thickness, friction coefficient, and stress field that are plotted and discussed in detail.

Obtained stress field then is used to find the fatigue life of the component; the findings of this section are in line with experimental data provided in [50].

3.2 Modified Reynolds equation

General Reynolds equation for line contact as described in the previous chapter is used. Application of line contact is not only limited to rollers but also valid for spur gear contact as well since two conjugate spur gears in mesh with a good approximation share the same line of contact at each mesh position. Similarly, by defining x direction to be the one pointing in the direction of rolling and sliding, the hydrodynamic lubrication fluid flow bounded between solid surfaces 1 and 2, which move at respective velocities, u_1 and u_2, is described by the modified Reynolds equation as [38].

$$\frac{\partial}{\partial x}\left(\phi\frac{\partial p}{\partial x}\right)=u_r\frac{\partial(\theta\rho h)}{\partial x}+\frac{\partial(\theta\rho h)}{\partial t} \tag{23}$$

where p denotes pressure, h represents the thickness of lubrication film and u_r is usually referred to as rolling velocity or entraining velocity, taking the average of the tangential velocities of the solid surfaces as $u_r=(u_1+u_2)/2$. The lubricant compressibility is included in Eq. (23) through the relationship between lubricant density, ρ, and pressure of [25], [51]

$$\rho=\rho_0\frac{1+\lambda_1 p}{1+\lambda_2 p} \tag{24}$$

where $\lambda_1=2.266\ \text{GPa}^{-1}$, $\lambda_2=1.683\ \text{GPa}^{-1}$, and ρ_0 is fluid density under ambient pressure. The second term on the right-hand side of Eq. (23) is the squeeze term and is dependent on time, t.

In order to incorporate the effect of lubrication level, a fluid film fraction θ is introduced into Eq. (23), according to Elrod [39], this term will take values between 0 to1. with 1

indicating a fully flooded condition where the lubricant is sufficient between contacting surfaces and $\theta < 1$ where pressure is less than ambient pressure creating cavitation/lubrication starvation condition. In conditions where $\theta < 1$ the gap between contacting surfaces is filled with lubrication and air together, creating the condition for cavitation. Similar equations as described in chapter two for flow coefficient, viscosity, and dimensionless shear stress are valid for modified Reynold's equations as well, for continuity of the subject author briefly includes the equations here in this chapter as well.

In the case of rotating components in rolling/sliding motion, the effect of high sliding motion causes a phenomenon referred to as the shear thinning effect. The shear-thinning effect tends to reduce lubrication thickness in the aforementioned components. this effect is included in the term ϕ, as is called flow coefficient and has the form of [38]

$$\phi = \frac{\rho h^3}{\eta} \frac{1}{\hat{p}_x} \int_{-1/2}^{1/2} \hat{z}\hat{\tau} f\left(\hat{\tau}\right) d\hat{z} \tag{25}$$

for gear pairs in contact, for example, this coefficient for mesh positions away from pitch point is considerable. In the vicinity of the pitch point in spur gear contact sliding speed is negligible while before and after the pitch point in the addendum and dedendum area, the sliding ratio is considerable where the nonnewtonian effect is expected to decrease the lubrication film thickness 41].

$\hat{p}_x = (h/G)(\partial p/\partial x)$ represents rolling direction pressure gradient. This dimensionless parameter is normalized utilizing film thickness, *h*, and lubricant Newtonian limit shear stress, *G*. Denoting an axis, which directs across the film thickness from surface 1 to surface 2, as *z*, its dimensionless counterpart, $\hat{z}$, used in Eq.(25), is defined as $\hat{z} = z/h$.

The origin of the $\hat{z}$ axis is set in the middle along with the film thickness, and $\hat{z} = -1/2$ and $1/2$ at surfaces 1 and 2, respectively. The lubricant low-shear viscosity, η, in Eq.(25), is experimentally characterized and found to be dependent on pressure and temperature as [52]

$$\eta = \eta_0 \left(1 + \frac{\hat{\alpha}}{\hat{b}} p \right) \exp\left(\frac{C_F p}{p_\infty - p} \right) \tag{26}$$

where η_0 is low-shear viscosity under ambient pressure, $\hat{\alpha} = a_0 - a_1/T_f + a_2/T_f^2$, $\hat{b} = b_0 + b_1/T_f$, and $p_\infty = c_0 + c_1/T_f$, all of which are functions of fluid temperature, T_f. The other constant C_F is a material parameter. Lastly, in Eq. (25), $f(\hat{\tau})$ is a lubricant rheological function that has the form of [41]

$$f\left(\hat{\tau}\right) = \left(1 + \left|\hat{\tau}\right|^{\beta}\right)^{\frac{1-n}{\beta n}} \tag{27}$$

where $\hat{\tau}$ is dimensionless viscous shear, and $\hat{\tau} = \tau/G$. The two constants involved in Eq. (27), *n* and β, are the shear rate sensitivity coefficient and the Yasuda parameter. They are material properties and, similar to the other constants involved in Eq.(26), are obtained through experimental measurements [41], [53].

Due to significant roughness profiles present on gear tooth surfaces produced by finishing processes, lubrication film is often not sufficiently thick to fully separate the mating surfaces for automotive gearing applications even under fully flooded lubrication conditions. When starvation is concerned, local asperity contacts are expected to be much more frequent. To describe such contacts, the film thickness within the asperity interaction

areas is considered to be constant, such that the film thickness gradient in the rolling direction is [38], [54]

$$\frac{\partial h}{\partial x} = 0 \tag{28}$$

It is noted the surface curvature gap before loading, g_0, and elastic deformation under loading, V [55], together with the roughness height fluctuations of surface 1, s_1, and surface 2, s_2, are included in the above governing equations via the film thickness description of $h = h_0 + g_0 + V - s_1 - s_2$ [38], [54]. Here, h_0 is a reference film thickness and is determined by implementing the equilibrium between applied normal force density, W, and contact pressure as

$$W = \int p dx \tag{29}$$

The numerical solution of the above tribological governing equations yields the normal contact pressure and film thickness distributions across the lubricated contact zone.

3.3 Multi-axial Stress Fields

the surface tangential shear stress is determined as $q = \eta\dot{\gamma} / f(\hat{\tau})$ for fluid areas, where $\dot{\gamma}$ is shear strain rate; and $q = \mu_b p$ for asperity contact areas, where boundary lubrication is assumed and the boundary lubrication friction coefficient, μ_b, is set to take the value of $\mu_b = 0.1$, following Refs. [24], [38], [56]. The normal and tangential tractions, namely p and q, dictate the stress fields on and below the contact surface as demonstrated in Figure 4.

In view of the contact zone size, it is small in comparison to the contact body. Therefore, the half-space assumption is employed, and the stress fields along the contact surface follow [55]

$$\sigma_x = -p(x,t) - \frac{2}{\pi}\int \frac{q(x',t)}{x-x'}dx' \tag{30}$$

$$\sigma_y = -p(x,t) \tag{31}$$

$$\sigma_{xy} = -q(x,t) \tag{32}$$

Below the surface, the stress fields read [55]

$$\sigma_x = -\frac{2y}{\pi}\int \frac{p(x',t)(x-x')^2}{\left[(x-x')^2+y^2\right]^2}dx' - \frac{2}{\pi}\int \frac{q\left(x',t\right)(x-x')^3}{\left[(x-x')^2+y^2\right]^2}dx' \tag{33}$$

$$\sigma_y = -\frac{2y^3}{\pi}\int \frac{p(x',t)}{\left[(x-x')^2+y^2\right]^2}dx' - \frac{2y^2}{\pi}\int \frac{q(x',t)(x-x')}{\left[(x-x')^2+y^2\right]^2}dx' \tag{34}$$

$$\sigma_{xy} = -\frac{2y^2}{\pi}\int \frac{p(x',t)(x-x')}{\left[(x-x')^2+y^2\right]^2}dx' - \frac{2y}{\pi}\int \frac{q(x',t)(x-x')^2}{\left[(x-x')^2+y^2\right]^2}dx' \tag{35}$$

In Eqs. (30) and (33), the *y* axis points downward from the surface into the material, and the integrals are performed over the entire contact zone. Considering a line contact with a large width, which is representative for gear contacts, equations (30) and (33) assume plane strain condition. that surface topography effect is not included in the above stress formulations [57], since the half-space adopted is perfectly smooth. The surface roughness impact on stresses is included only through the normal and tangential tractions, *p* and *q*, yielded from the tribological analysis. To directly take into account the surface topography

variation in the stress field determination, the computationally much more involved boundary element method proposed by Li [57] may be used in the place of Eqs. (30) And (33), however, on the cost of significantly elevated computational efforts.

$p(x',t)$ is surface contact pressure and $q(x',t)$ is the shear stress distribution. Where x' is the surface coordinate along the x direction and t is the time. The y axis is normal to the surface of the thin slice, which points to the material. Stress field equations (33),(34), and (35) are written as the sum of one-dimensional convolution operation between pressure and shear distribution and their corresponding influence functions.

To determine the fatigue life, this multiaxial stress field is required, this stress field is calculated and saved for each time instant for σ_x, σ_y, and σ_{xy}.

Once the stress field relative to the fixed frame is obtained, the critical plane is searched numerically for maximum shear stress.

The stress transformation method is used for finding the maximum shear stress of τ_a Figure 5.

Critical plane search is defined as the plane with maximum shear stress, the method to find this plane is by changing the value of θ and finding the associated τ_a for each time instant.

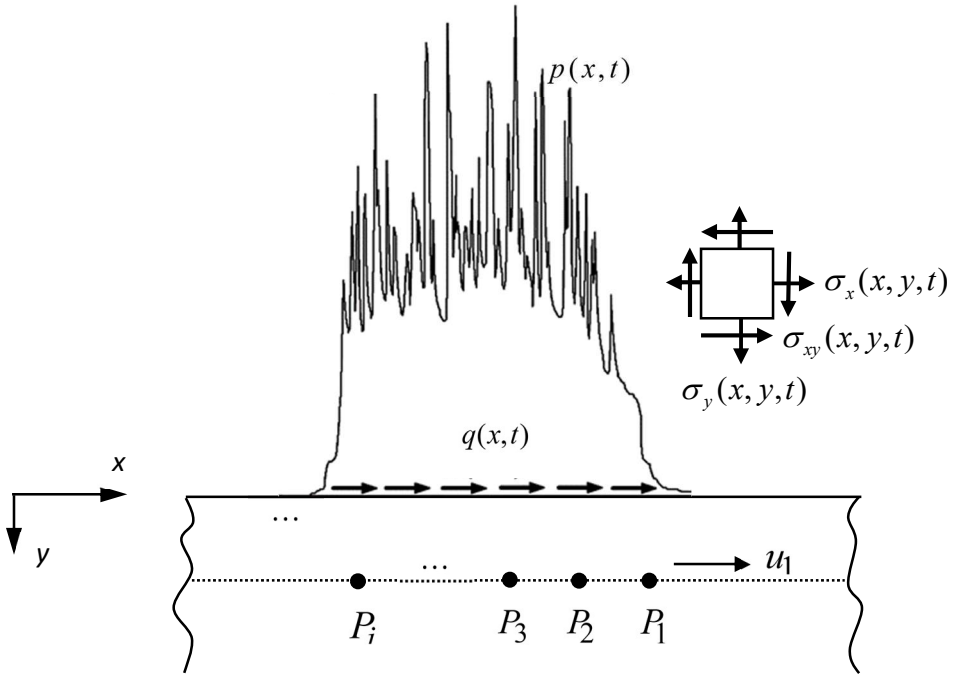

Figure 4 Schematic view of material points (P_i) passing through computational domain

Coordinate transformation method is carried out in x and y direction as follows[49]:

$$\sum{}' X = \frac{1}{2}\left(\sum X + \sum Y\right) + \frac{1}{2}\left(\sum X - \sum Y\right)\cos(2\theta) - \sum{}_{xy}\sin(2\theta) \tag{36}$$

Equation (36) is stress component in X' direction having a rotation of θ.

$$\sum{}' Y = \frac{1}{2}\left(\sum X + \sum Y\right) - \frac{1}{2}\left(\sum X - \sum Y\right)\cos(2\theta) + \sum{}_{xy}\sin(2\theta) \tag{37}$$

Equation (37) is stress component in Y' direction having a rotation of θ.

$$\sum{}' XY = \frac{1}{2}\left(\sum X - \sum Y\right)\sin(2\theta) + \sum XY\cos(2\theta) \tag{38}$$

And Equation (38) is the shear stress component in the $X'Y'$ plane.

Transformed stress components as shown in Figure 5 are used to find maximum shear stress amplitude as follows

$$\begin{aligned}\tau_a = {} & \frac{1}{2}Max\left[\sum{}' XY(\theta,t_1), \sum{}' XY(\theta,t_2), ..., \sum{}' XY(\theta,t_n)\right] - \\ & \frac{1}{2}Min\left[\sum{}' XY(\theta,t_1), \sum{}' XY(\theta,t_2), ..., \sum{}' XY(\theta,t_n)\right]\end{aligned} \tag{39}$$

This will allow finding the maximum shear stress by incrementing θ for small degrees to find the angle at which τ_a is maximum is calculated.

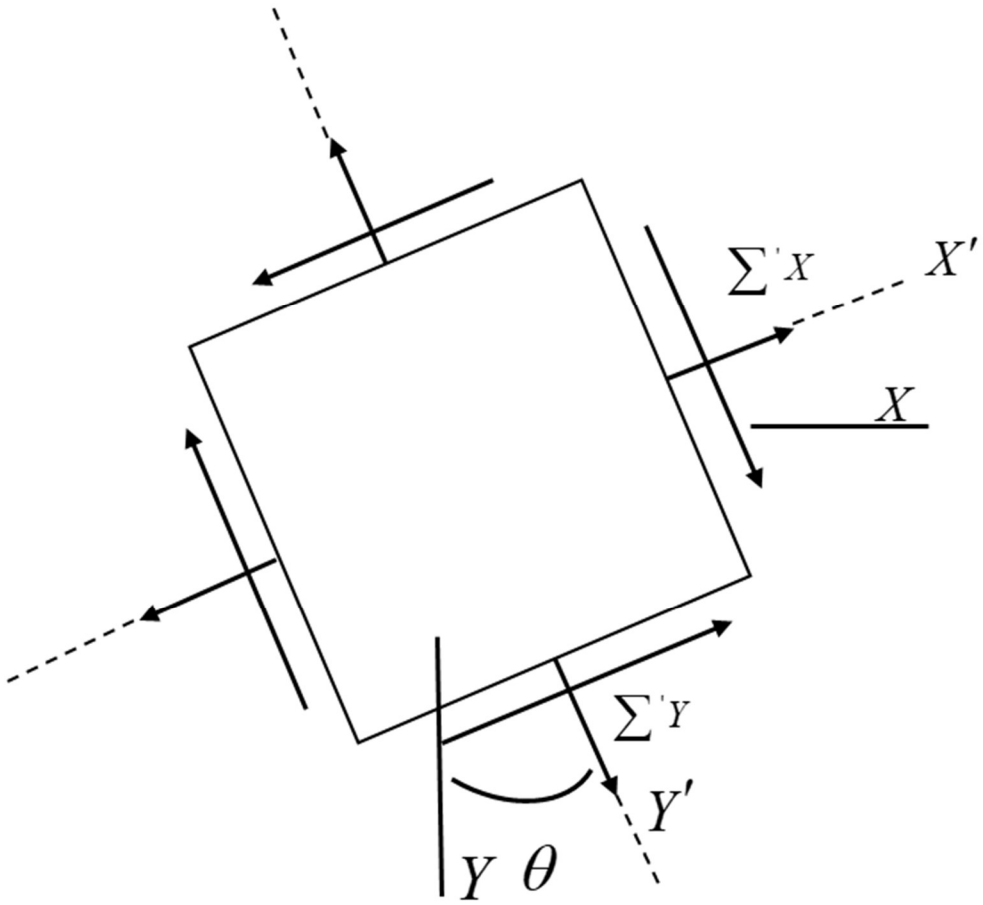

Figure 5 Plane stress transformation

3.4 Fatigue Assessment

Provided the multi-axial stress fields from the previous section, the stress amplitudes of normal and shear components, denoted as σ_a and τ_a respectively, are determined and used to evaluate the fatigue damage according to a failure criterion Criteria designed for the assessment of fatigue damage accumulation are diverse in literature. For contact problems where compressive stresses dominate, critical plane-based failure methods [58]–[61]or Weibull model-based one model based on [62] were employed by different researchers [24], [63], [64] to show surface or near-surface crack nucleation. In view of the agreements between model predictions and experimental measurements[24], [56], [65] the multi-axial method of [66]

$$\frac{1}{S_b(N_f)}\sqrt{\sigma_a^2+\left[\frac{S_b(N_f)}{S_t(N_f)}\right]^2\tau_a^2}=\varsigma\left(1-\frac{\sigma_{m,\max}}{S_y}\right) \tag{40}$$

appeared to yield better results, and thus is employed in this study. In Eq. (10), S_b and S_t represent fatigue strength of polished small specimens operating under fully reversed bending and torsion conditions, respectively. Their quantitative dependence on the number of cyclic loadings, N_f, was obtained through experimental measurements [56].

The mean normal stress effect on fatigue damage is included through the right-hand side of Eq. (40), where $\sigma_{m,\max}$ is the mean normal stress acting on the plane that experiences the maximum shear stress amplitude, S_y is the yield strength, and ς is a material parameter that is dependent on the fatigue strength ratio of S_b/S_t [66]

Chapter 4. Results and discussion

4.1 Overview

In this chapter results of the Tribo-Dynamic model and Fatigue life model are discussed with an explanation/ justification of trends in output change based on a range of input variables.

Starting from the Tribo-Dynamic model, based on different pit sizes and operating conditions, results of acceleration magnitude, approach velocity of contacting rollers, bearing forces, contact force, and pressure distribution comparison are presented for a pair of identical rollers. Surface roughness in this phase of the model is kept similar for each roller. Using a smooth surface topography is simulation.

Extending the Tribo-Dynamic model to the fatigue life model is the second phase, where results of pressure distribution, lubrication film thickness, etc. will be used to access materials fatigue performance.

Results are the comparison of average lubrication film thickness for different starvation levels, t transient pressure distribution for different surface finish and contact pressure, surface shear and film fraction parameters, median fatigue life for different surface finish, and different contact pressure under different starvation levels.

4.2 Tribo-Dynamic model

This study employs a contact formed by two identical cylindrical disks, whose radii are 31.75 mm, and axial direction widths are 6.35 mm. The disks are mounted onto their respective rotational shafts, which are belt-driven and supported by four precision ball bearings. as shown in Table 1, The masses of the disk assemblies (disk, shaft, and lock nut) are 3 kg. The stiffness and damping of the supporting bearings are 7.8×10^8 N/m and 1934.31 Ns/m, respectively. This contact pair operates under the normal force of $F_0 = 2800$ N, which leads to a Hertzian pressure of $p_h = 1$ GPA, and a half Hertzian width of $a_h = 281\mu m$. Adopting a turbine fluid, Mil-L23699, as the lubricant, the supply temperature is controlled at 80 °C. For the properties of the lubricant [associated with Eqs. (11) and (12)], they are referred to Ref [67]. Setting the rolling velocity at $u_r = 8$ m/s, and a slide-to-roll ratio that is defined as $SR = (u_1 - u_2)/u_r$ at -0.5, the disk surface velocities arrive at $u_1 = 6$ m/s and $u_2 = 10$ m/s.

Surface pits dimensions as displayed in Table 2 range from 0 to 700 μm in width and 0 to 268 μm in-depth. Figure 6 shows the location and dimensions of surface pits. The shape of pits is chosen to resemble actual surface pits on rollers (Gear pairs), where surface pits tend to shape an triangular shape. The first case in this table is the normal condition, where there are no pits on the surface and surface roughness in the input to the model. The result of this case is generated as an example of normal operation as compared to other cases where pit size can severely impact dynamic response. The largest pit width in Case *VII* is selected to exceed the size of the nominal Hertzian zone, such that significant vibration can be observed. An increment of 100 μm is used between these two pit width bounds. As

mentioned earlier, the effect of surface roughness is considered in this simulation. surface roughness of $R_q = 0.11\mu m$ is used in this experiment as the baseline. Figure 7 displays the topography of the surface. Achieving very smooth surface roughness values similar to what is used in this model can be done through different surface finish methods. ISF (Isotropic surface finish) for example can create surfaces with such a low surface roughness. The pit profile is superimposed on the roughness profile to arrive at the total surface topography for surface 1, S_1, while only the roughness profile is included for surface 2 topography, S_2 . Assuming that only one surface is experiencing pitting.

These excitations come into play through the film thickness equation (5). The reason that the pit is put on the slower surface ($u_1 < u_2$) is that pitting failure commonly appears in the dedendum of gear teeth, where the surface velocity is lower than that of its mating counterpart.

However, the model is capable of simulating surface pits on both sides. In this computational simulation, the start and end of the computational domain ($x_s \le x \le x_e$) are set as $x_s = -3.375a_h$, and $x_e = 2.625a_h$.

The computational domain is discretized into 1024 elements, leading to a mesh size of 1.6 μm, which is in the same order as the surface roughness measurement resolution, and more than sufficient to describe the surface pit geometry. the dynamic disk approach-displacement, ($x_1^d - x_2^d$), and the dynamic disk approach-velocity, ($\dot{x}_1^d - \dot{x}_2^d$), contribute to

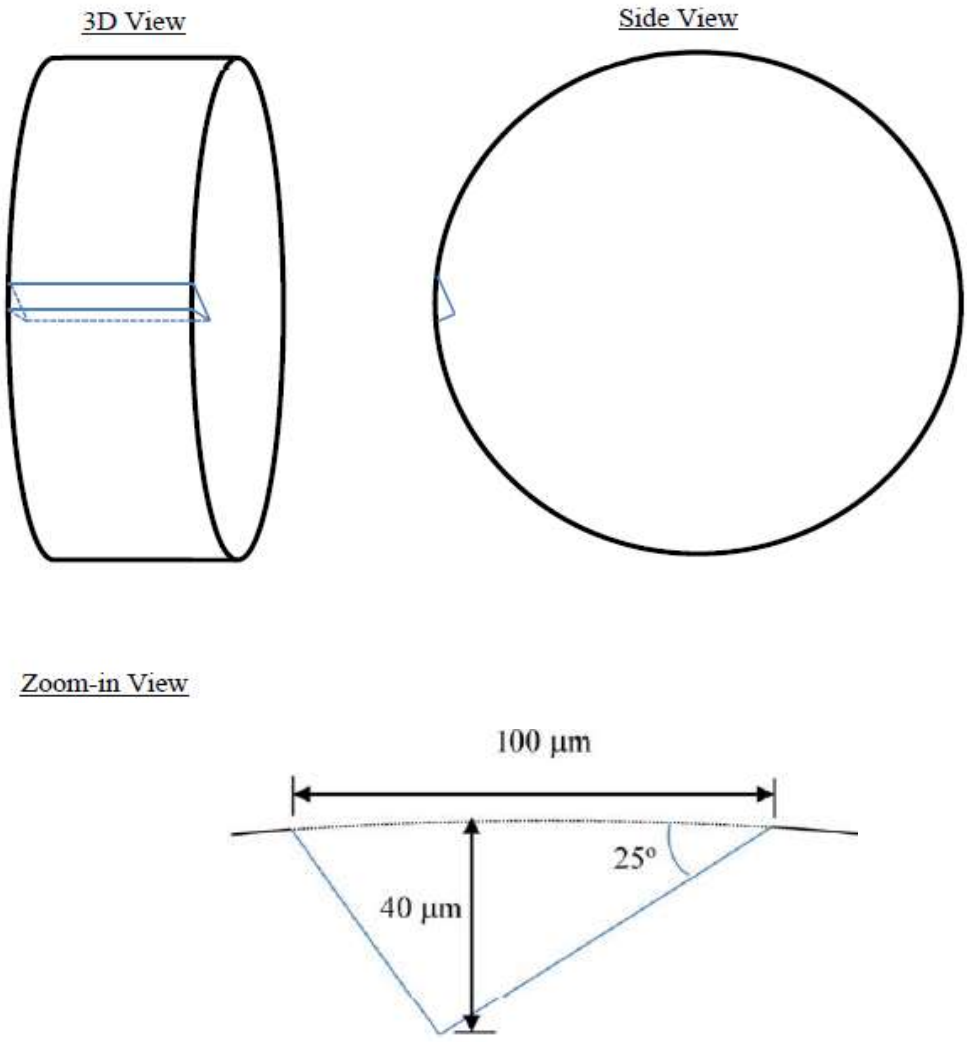

Figure 6 schematic of surface pits dimensions and its location on the surface

Table 1 Disk's dimensions, materials properties, and operating conditions

Disk radii (mm)	31.75
Disk width (mm)	6.35
Contact Force (N)	2800
Disk, shaft, and lock nut mass (kg)	3
Supporting bearing Stiffness (N/m)	7.8×10^{8}
Supporting bearing Damping (Ns/m)	1934
Oil temp (^{o}C)	80
Disk 1 speed ($\frac{m}{s}$)	6
Disk 2 speed ($\frac{m}{s}$)	10

the lubrication fluid flow through the film thickness equation and the Reynolds equation, playing an important role in the Tribo-Dynamic behavior of the line contact problem.

The phase plots of ($\dot{x}_1^d - \dot{x}_2^d$) versus ($x_1^d - x_2^d$) of the eight pit cases defined in Table 2 are constructed and compared in Figure 8.

Table 1 includes the operating condition for contacting rollers.

Supporting bearing stiffness and damping values are estimated based on a typical roller tester.

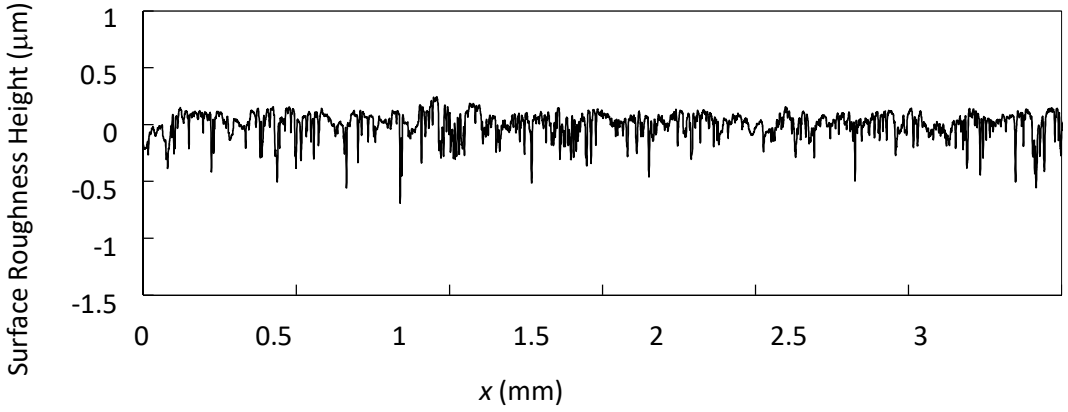

Figure 7 roughness profile measured from a polished surface

Table 2 Pits dimensions

Case #	w_P (μm)	d_P (μm)
I	0	0
II	100	38
III	200	77
IV	300	115
V	400	153
VI	500	192
VII	600	230
VIII	700	268

Table 2 summarizes the surface pits dimensions used in this model. Starting from no surface pits with zero-depth and width in case I, gradually pit size grows to $700\mu m$ width and $268\mu m$ depth in case *VIII*.

This test matrix is designed to capture the impact of surface defect size and depth, as in real operating conditions where pitting starts to generate on surfaces, the size of surface defect may be small, and gradually with progressive pitting, size, and the number of surface defects grows in extreme conditions.

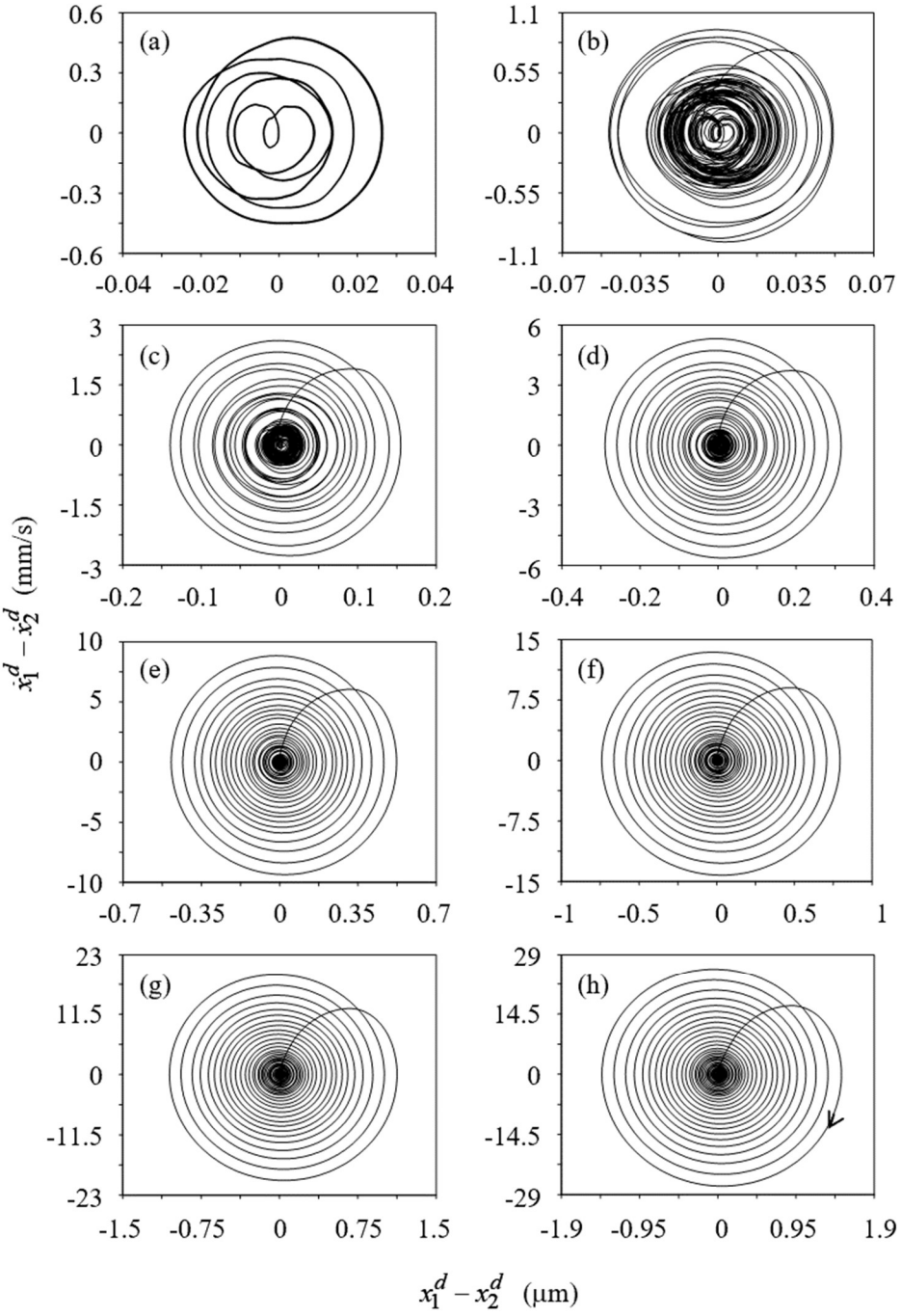

Figure 8 Approach-velocity versus approach-distance plot for pit dimension of (a) I, (b) II, (c) III, (d) IV, (e) V, (f) VI, (g) VII, (h) VIII as defined in Table 1.

It is shown, that as the pit grows, both the amplitudes of the approach displacement and the approach-velocity increase. When the pit enters and travels through the contact zone as in Case *II* – Case *VIII*, the envelope curve initiates from the center and spirals outwards to form the largest envelope and excite the vibration. An arrow is placed in Figure 8 (h) to show the direction of the spiral course. After the pit exits the EHL conjunction, the curve then spirals inwards owing to the damping effect, resulting in the continuous shrinking of the displacement and velocity amplitudes. for case *I,* where there is no pit on the surface, the magnitude of approach velocity and distance is not zero.

This is mainly because of the surface roughness effect. Roughness amplitudes, however small values when passing through the contact zone, generate a similar curve. Figure 8 also shows the order of magnitude in approach velocity increase for larger pit sizes, showing for the maximum pit size of Table 2 approach velocity can reach to ~ 40 times of normal condition without the presence of surface pits. The dynamic behavior of the approach of the two disks introduces oscillation in the lubrication film thickness, and leads to the fluctuation of the contact force, F_c. Such a relationship is visualized in Figure 9, where the contact force is plotted against the approach displacement. It is observed, that when no pit is present in Case *I*, the surface roughness induced dynamic vibration is negligibly small. The contact force remains almost constant at 2800 N with a fluctuation range of 15 N. In the meantime, the approach-displacement swings in a very small range of $0.05\ \mu m$. smooth surface roughness with a small variation of peaks and valleys keeps the load constant, indicating a healthy surface, where no pits exist at this stage. As gradually the pits size increases, the dynamic effect of pits on the surface begins to appear on contact force plots.

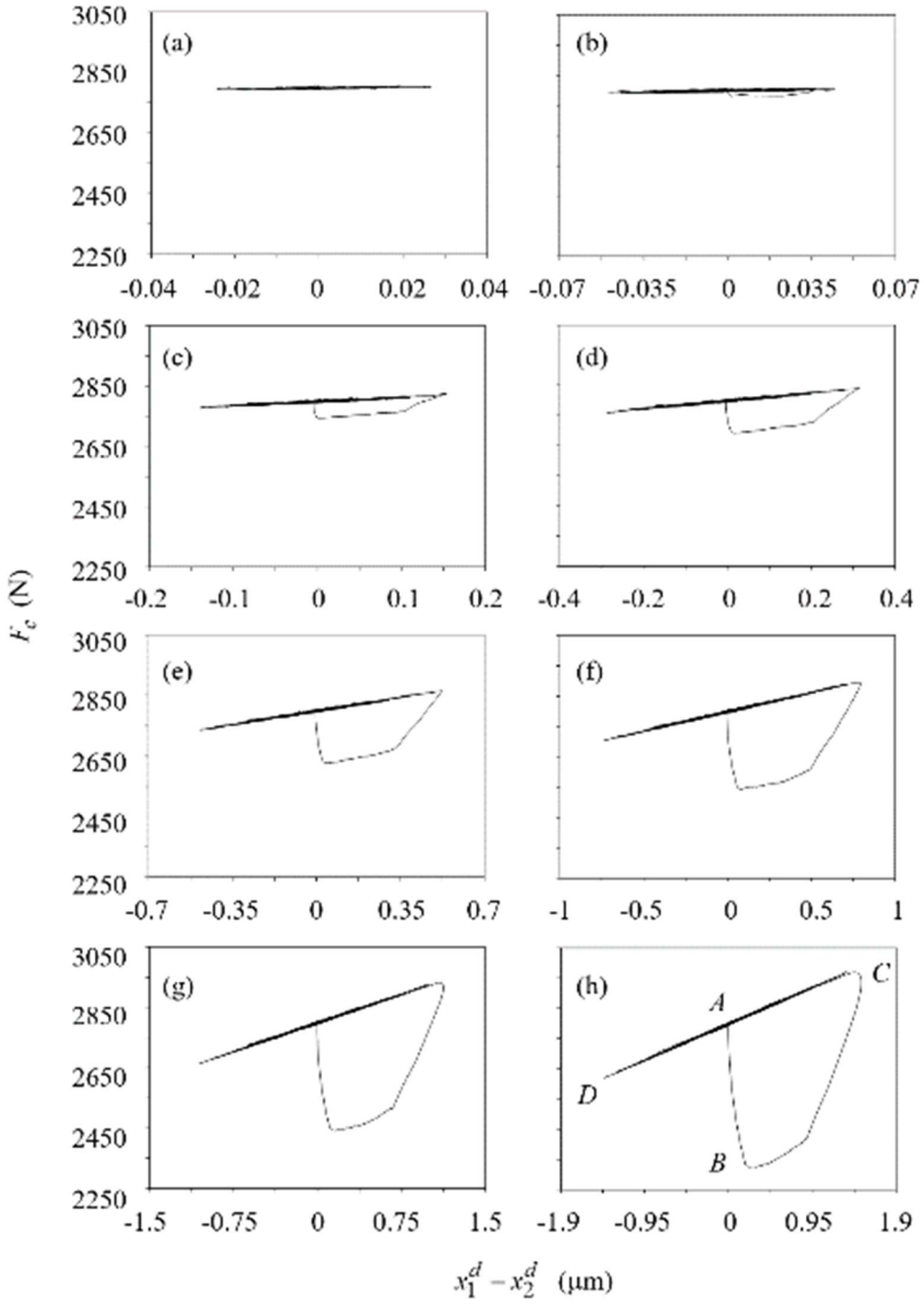

Figure 9 Contact force versus approach-distance plot for pit dimension of (a) I, (b) II, (c) III, (d) IV, (e) V, (f) VI, (g) VII, (h) VIII as defined in Table 1.

For the largest pit considered in Figure 9(h) , the contact force first decreases as the pit enters the contact zone along the path from *A* to *B*, where the large valley topography of the pit introduces large film thickness and results in the reduction of the contact force. The smaller F_c, in comparison with the applied normal load, F_0, breaks the equilibrium and leads to the movement of the two disks, i.e. the approach of the two disks, which decreases the film thickness and increases the contact force, along the path from *B* to *C*. After the pit leaves the EHL conjunction, the vibration continues between *C* and *D* with a maximum range of 350 N, which decreases over time due to damping till the pit reenters the contact zone. In between Case *I* and Case *VIII*, the variation of F_c follows the same pattern, while with a smaller fluctuation range. This fluctuation of load on the contact area in practice further accelerates the rate of pitting on the surface, alarming the importance of early diagnosis of pitting failure.

The fluctuation in contact load causes fluctuations in bearings as well. Bearing load calculation is of importance due to cyclic loading impact which can pass maximum permissible contact stress for which bearing is designed and causes premature failure.

When the disks vibrate, the bearing forces associated with the bearing stiffness and damping (k_1 and c_1 for Disk 1 support, and k_2 and c_2 for Disk 2 support, as illustrated in Figure 2-1) fluctuate. Using Disk 1 as an example, its bearing force $F_{b1} = F_0 - (c_1\dot{x}_1^d + k_1 x_1^d)$ is plotted against the disk dynamic approach in Figure 10. The amplitude of the bearing force is shown to elevate as the pit size increases.

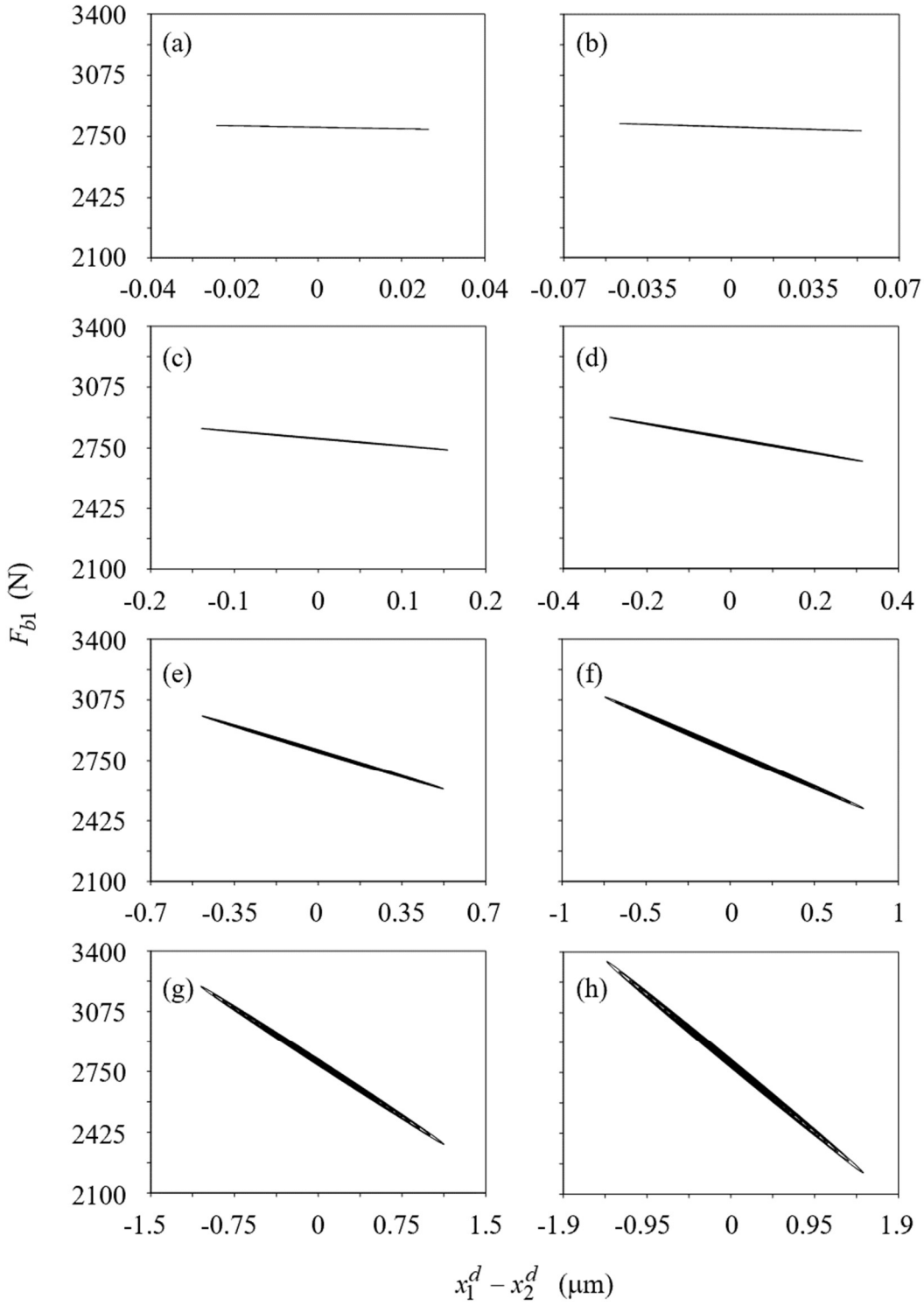

Figure 10 Disk 1 bearing force versus approach-distance plot for pit dimension of (a) I, (b) II, (c) III, (d) IV, (e) V, (f) VI, (g) VII, (h) VIII as defined in Table 2.

In comparison to the contact force, the slope in Figure 10 is opposite to the slope in Figure 9, indicating the bearing force decreases as the contact force increases.

This is due to the displacement and velocity rise of Disk 1 when it approaches Disk 2. The fluctuation range of F_{b1} is only 24 N when no pit is present in Case *I* and reaches 1140 N for the largest pit in Case *VIII*. It is thus concluded that the polished surface roughness introduces negligible bearing force amplitude. Once pitting failure takes place, it can exert significant dynamic force onto the supporting bearings and damage them.

This model can accurately calculate bearing forces under EHL conditions when surface pits are present. In applications where high-speed bearings are implemented such as EV gearboxes, bearing failure due to load fluctuation as a result of pitting on the gear surface is common.

The oscillations of the bearing forces and the contact force dictate the dynamic response of the contact pair as they roll against each other.

Acceleration results as caused by dynamic response impacted by surface pits also is of importance for NVH purposes.

The resultant acceleration of Disk 1, denoted as a_1, is plotted in Figure 11 for two consecutive rotation cycles, where the unit of acceleration is $\mathrm{g} = 9.8\ \mathrm{m/s^2}$. A zoomed-in view is also constructed in Figure 12 for better illustration, focusing on the passage of the pit through the contact zone. The period of the vibration signal is observed to be 0.338 milliseconds, which corresponds to a natural frequency of 2959 Hz.

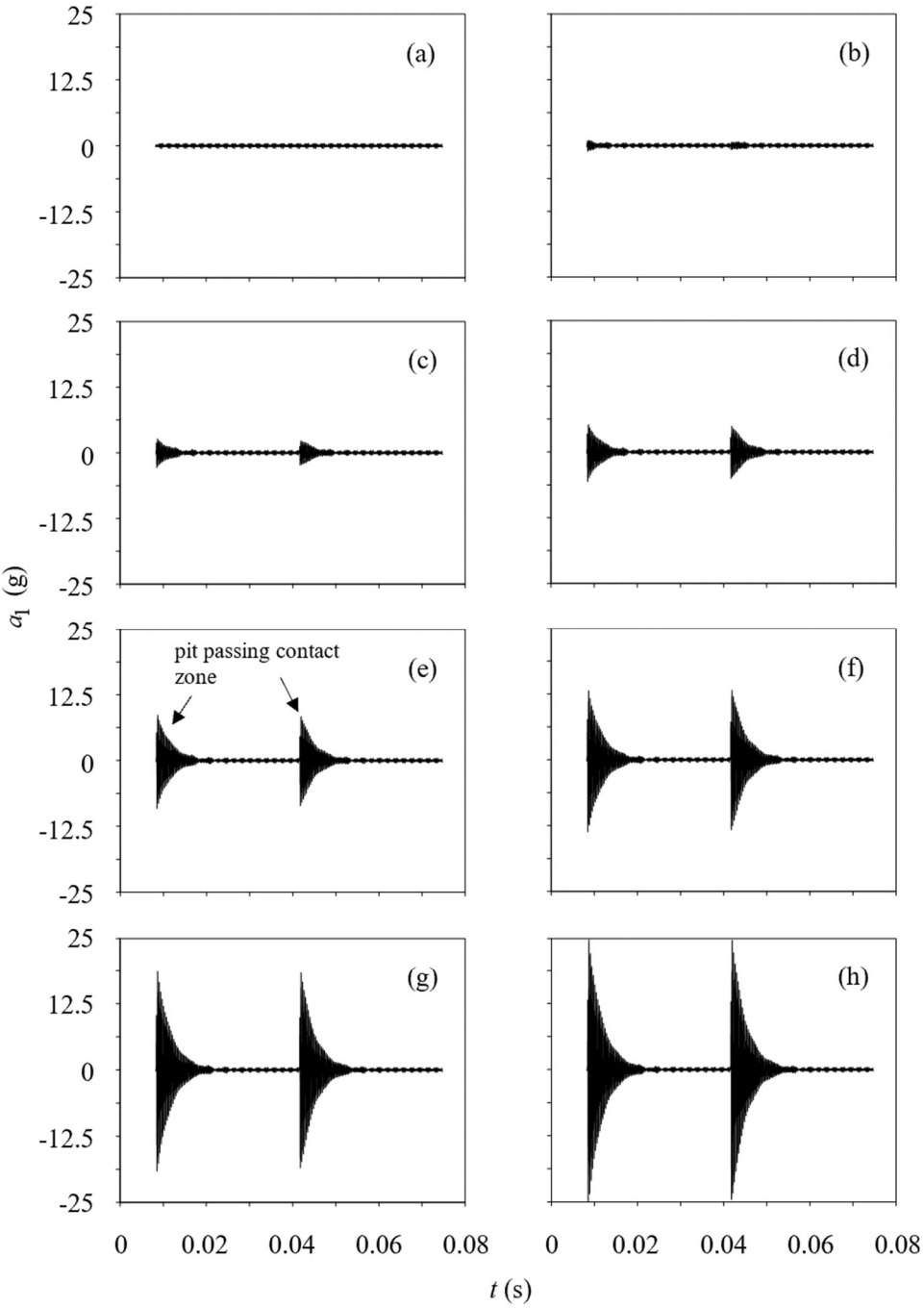

Figure 11 Acceleration response (two cycles) of disk 1 for pit dimension of (a) *I*, (b) *II*, (c) *III*, (d) *IV*, (e) *V*, (f) *VI*, (g) *VII*, (h) *VIII* as defined in Table 1 .

Comparing Case *I* with the others, the larger amplitude vibration at the beginning of each rotation, where the pit enters and travels through the EHL conjunction, is missing. The maximum amplitude of a_1 caused by surface roughness alone is 0.46 g. As the surface pit initiates and grows from Case *II* to Case *VIII*, the maximum amplitude of the acceleration elevates accordingly. As shown in Figure 11, with the uniform increment of w_P, the rise in the acceleration amplitude escalates, indicating a good response of acceleration to surface pit formation. That is probably why accelerometers are frequently equipped in rolling contact fatigue test set-up for pitting failure detection [68]–[70].

The surface with the largest pit size introduces 25g acceleration momentarily between contacting surfaces as the surface pit comes into contact, this magnitude is nearly 50 times more than the condition where there is no surface pits presence. this phenomenon follows by noise in the entire system as the pit size grows large. And suppresses bypassing the defected surface from the contact zone.

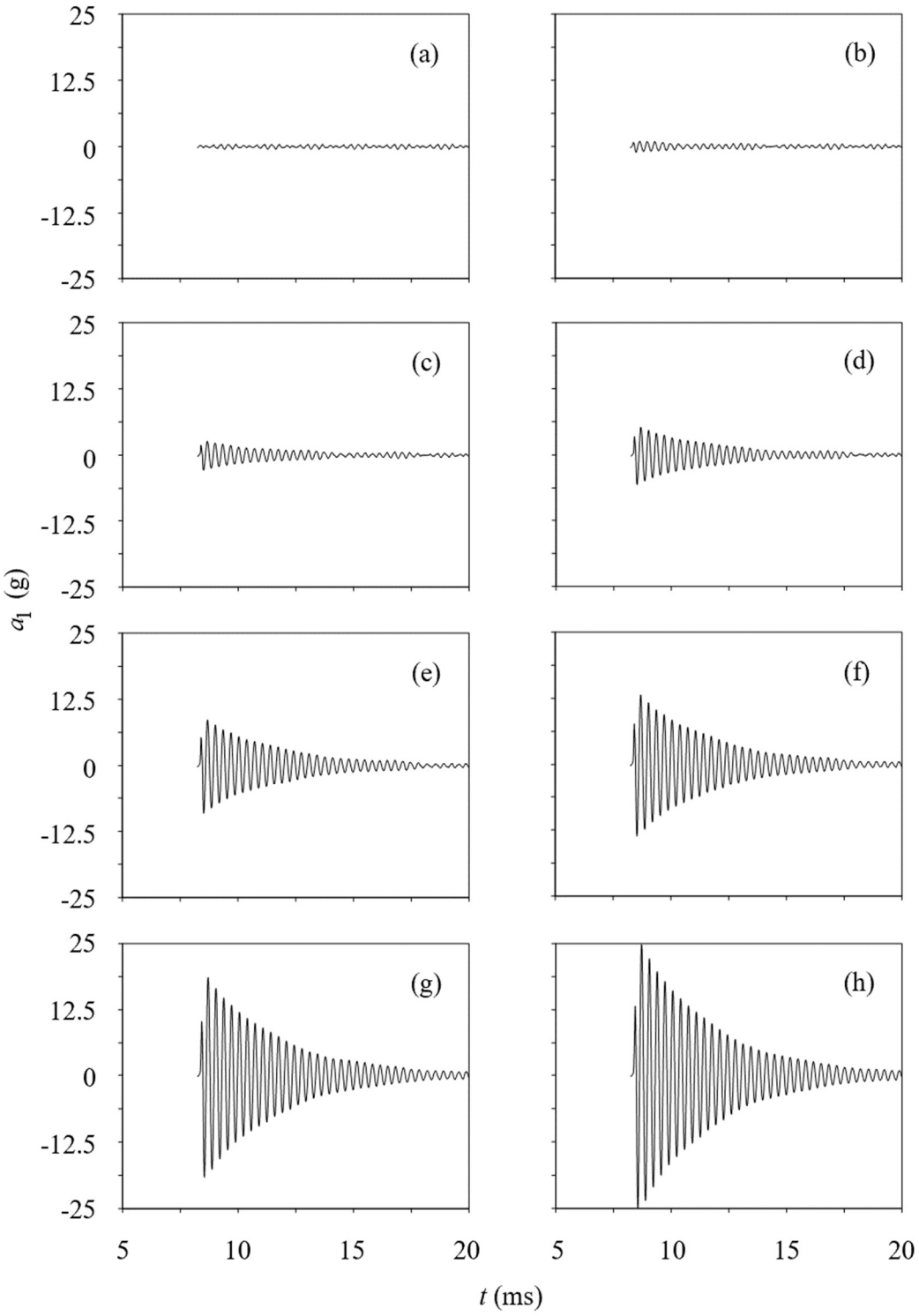

Figure 12 Acceleration response (zoomed in) of disk 1 for pit dimension of (a) I, (b) II, (c) III, (d) IV, (e) V, (f) VI, (g) VII, (h) VIII as defined in Table 2.

the Tribo-Dynamic analyses are compared with their quasi-static counterparts for pitting case *VII* in Figure 13 as an example, where the pit width is comparable to the nominal Hertzian zone size, and significant dynamic responses have been observed above. The left column of Figure 13 illustrates the pressure distribution as the pit passes through the EHL conjunction under the Tribo-Dynamic condition, and the right column displays the corresponding quasi-static simulation results.

The start and end of the pit topography are marked in the figure as *A* and *B*, respectively. In Figure 13(a), the pit has not fully entered the contact zone yet. Negligible pressure is developed within the pitted region, where the deep valley feature results in significant lubrication film thickness. Outside the pitted region, the contact pressure is established. However, this pressure is evidently smaller in comparison with the quasi-static simulation result in Figure 13(b).

The reason for this difference is that the quasi-static simulation enforces the equilibrium condition of Eq. (2). In the process, the reference film thickness, h_0, in Eq. (5) is decreased to introduce thinner lubrication film, and thus larger contact pressure and contact force to balance the applied normal force [71], [72], maintaining the quasi-static condition.

Without the implementation of Eq. (2) in the Tribo-Dynamic simulations, the smaller contact pressure and contact force (in comparison with the applied normal force) lead to the dynamic responses of the contact pair.

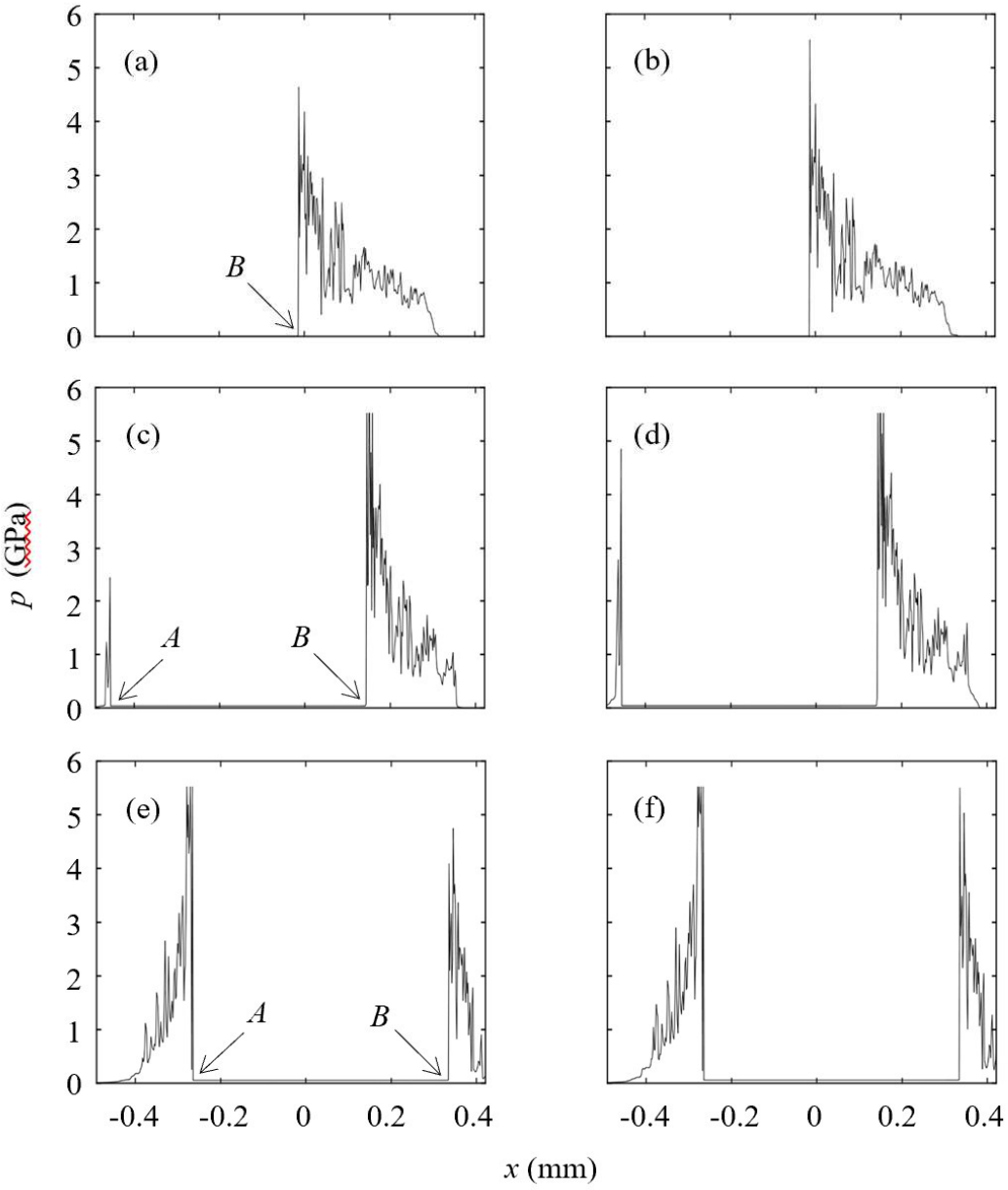

Figure 13 Comparison of pressure distribution between Tribo-Dynamic simulations [(a), (c), and (e)], and quasi-static simulations [(b), (d), and (f)] as pit passes through EHL conjunction for pit dimension of Case VII as defined in Table 2. A and B denotes the start and end of pit topography

As the pit passes through the contact zone in the second and third rows of Figure 13, similar observations can arrive. These clear deviations of the contact pressure under the Tribo-Dynamic condition from that under the quasi-static condition point to the important role of the dynamic behavior of the contact bodies in the tribological description.

Figure 14 displays the maximum amplitude of vibration as a function of pit size, for the large pit size $w_p = 700\mu m$ maximum acceleration amplitude, can rise to 25g, this jump indicates the sensitivity of dynamic response to pit sizer in crack initiation investigation.

A large rise of acceleration in vibration response tests of rolling elements is a way of quality controlling bearing, gears for the existence of surface cracks. In applications prone to surface pitting, constant control of vibration is required in order to ensure components will meet the designed life.

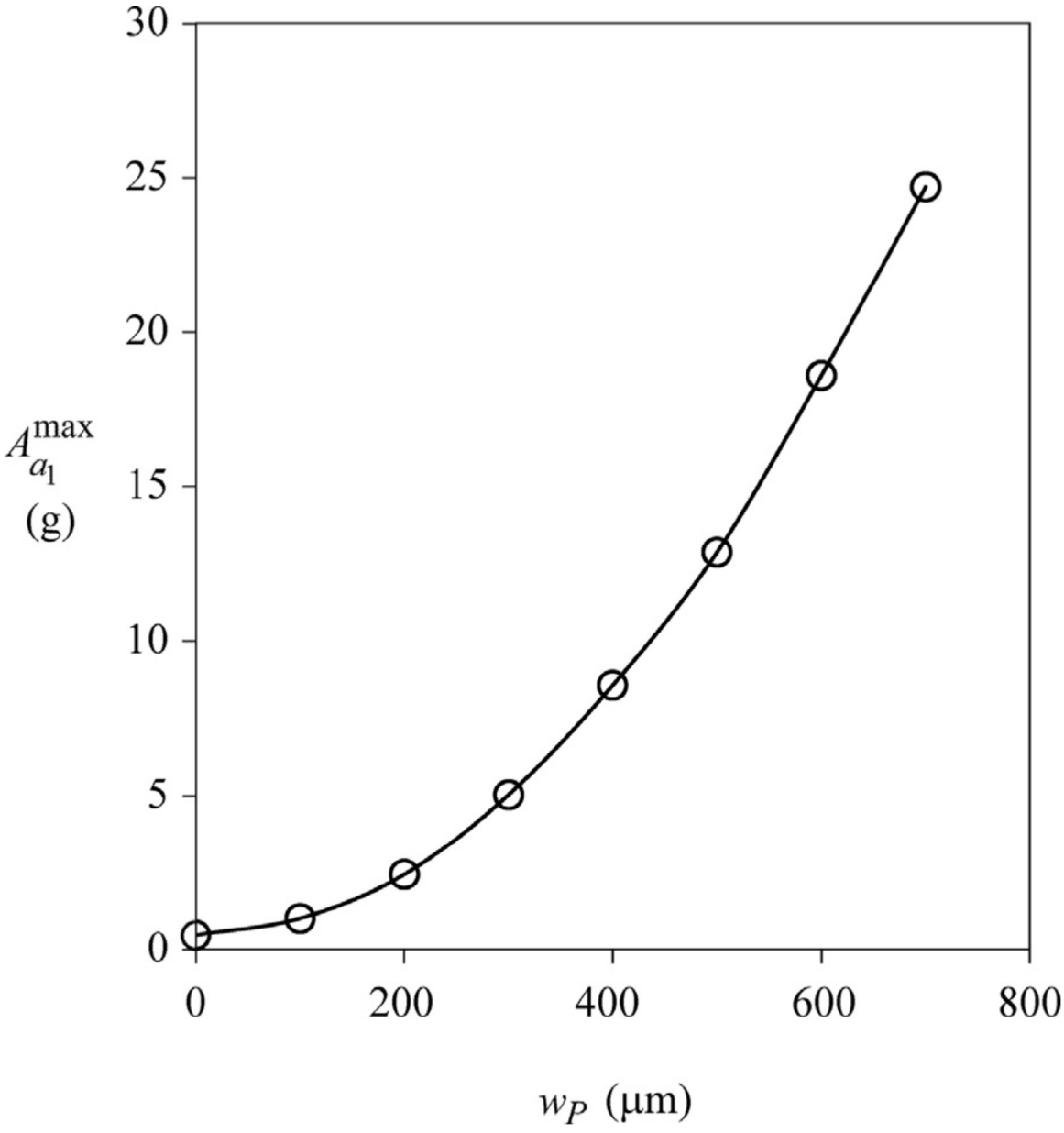

Figure 14 maximum amplitude of Disk1 acceleration versus surface pit width

4.3 Fatigue life model

This section uses the results of contact fatigue modeling and runs the analysis under two different loading conditions of $W = 637.5$ N/mm and 835 N/mm to produce low and high Hertzian contact pressures as $p_h = 1.75$ GPa and 2.0 GPa, respectively.

To investigate lubricant viscosity effect on contact fatigue under starved lubrication conditions, two inlet lubricant temperatures are implemented as $T_{in} = 100\ ^\circ\mathrm{C}$ and $50\ ^\circ\mathrm{C}$. Considering a Turbine fluid, MIL-L23699, its ambient low-shear viscosity, η_0, is increased from 4.64 mPas to 17.17 mPas when the temperature is reduced from $100\ ^\circ\mathrm{C}$ to $50\ ^\circ\mathrm{C}$. The lubricant viscosity dependences on pressure, temperature, and shear rate were determined through experimental measurements[73].

speed condition of the contact, variation is excluded in this study. The rolling velocity is kept constant at $u_r = 10$ m/s, and the sliding velocity that is defined as $u_s = u_1 - u_2$, is set at -5 m/s, resulting in a slide-to-roll ratio of $SR = u_s / u_r = -0.5$.

The negative u_s indicates surface 1 is moving slower than surface 2, representing the negative sliding condition that occurs in the dedendum of driving gear of gear contacts, where pitting failure takes place. To vary starvation extent, supplied inlet lubrication film thickness, h^{in}, is set to range from 0.2 μm to 10 μm. These low and high bounds selected correspond to severe starvation and no starvation conditions, respectively. Lastly, the surface roughness effect is examined by using two roughness profiles measured from ground gear tooth surfaces along the profile direction as displayed in Figure 15.

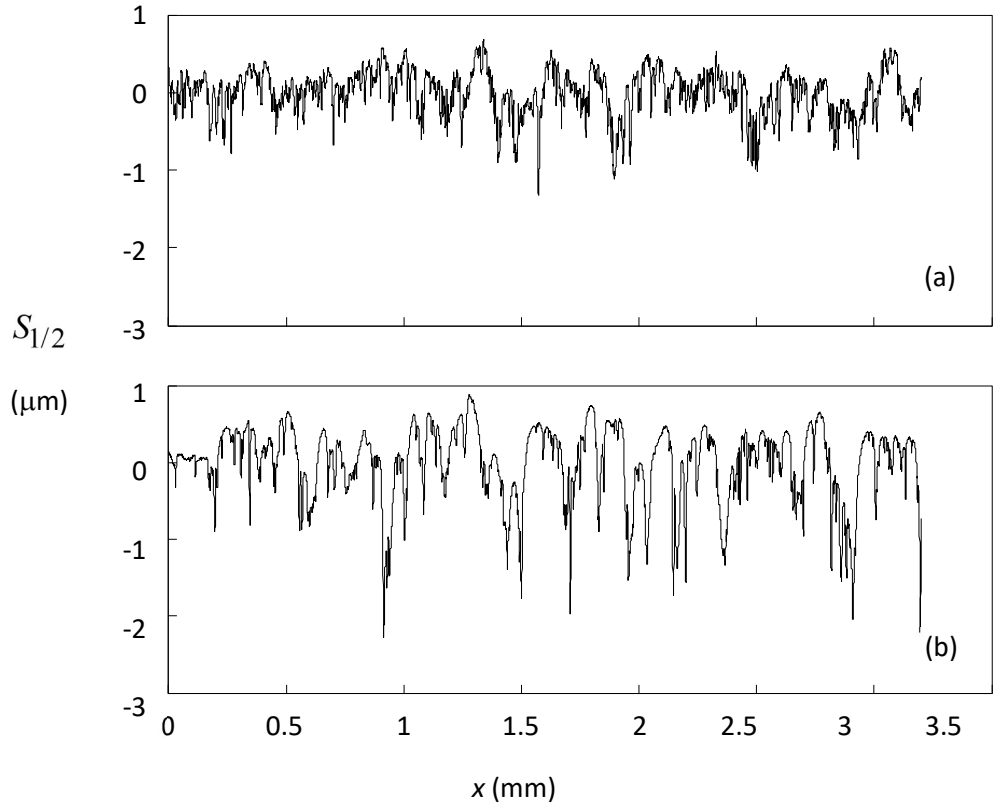

Figure 15 Measured surface roughness profiles of (a) $R_q = 0.3\mu m$, and (b) $R_q = 0.5\mu m$.

As displayed in Figure 15, the smoother ground surface has the root-mean-square (RMS) roughness amplitude of $R_q = 0.3\mu m$, and the rougher one is characterized as $R_q = 0.5\mu m$ .Summarized in Table 3, the above operating and surface conditions yield a total of 80 combinations, which are representative of typical automotive high-speed gearing applications that are subject to potential contact fatigue failure.

It is noted that the values taken are slightly different for the two surface roughness profiles as listed in Table 3. This is for the purpose of a better description of the non-linear relationship between fatigue life and starvation under different roughness conditions. These h^{in} values are determined according to the number of tryouts.

Defining the baseline simulation to be the smoother rough surface ($R_q = 0.3\mu m$) operates under the lower pressure ($p_h = 1.75$ GPa with $W = 637.5$ N/m), lower viscosity ($\eta_0 = 4.64$ mPas at $T_{in} = 100\ ^\circ\mathrm{C}$), and fully flooded ($h^{in} = 10\mu m$) condition, its tribological characteristics in terms of contact pressure, tangential shear, lubrication film thickness, and lubrication film fraction parameter are plotted in the left column of Figure 16. In the right column of the figure, the counterparts, where the inlet lubricant temperature is reduced to produce higher viscosity ($\eta_0 = 17.17$ mPas) while leaving the other parameters unchanged, are shown for comparison. It is expected that the film thickness increases with the increase of the lubricant viscosity. Consequently, the normal pressure and tangential shear are effectively decreased. The last row of Fig. 2, $\theta = 1$ in the vicinity of the inlet, indicates a non-starved lubrication condition. It should be noted the tribological behavior as shown in Figure 16 is time-dependent due to the movement of the surface roughness profiles.

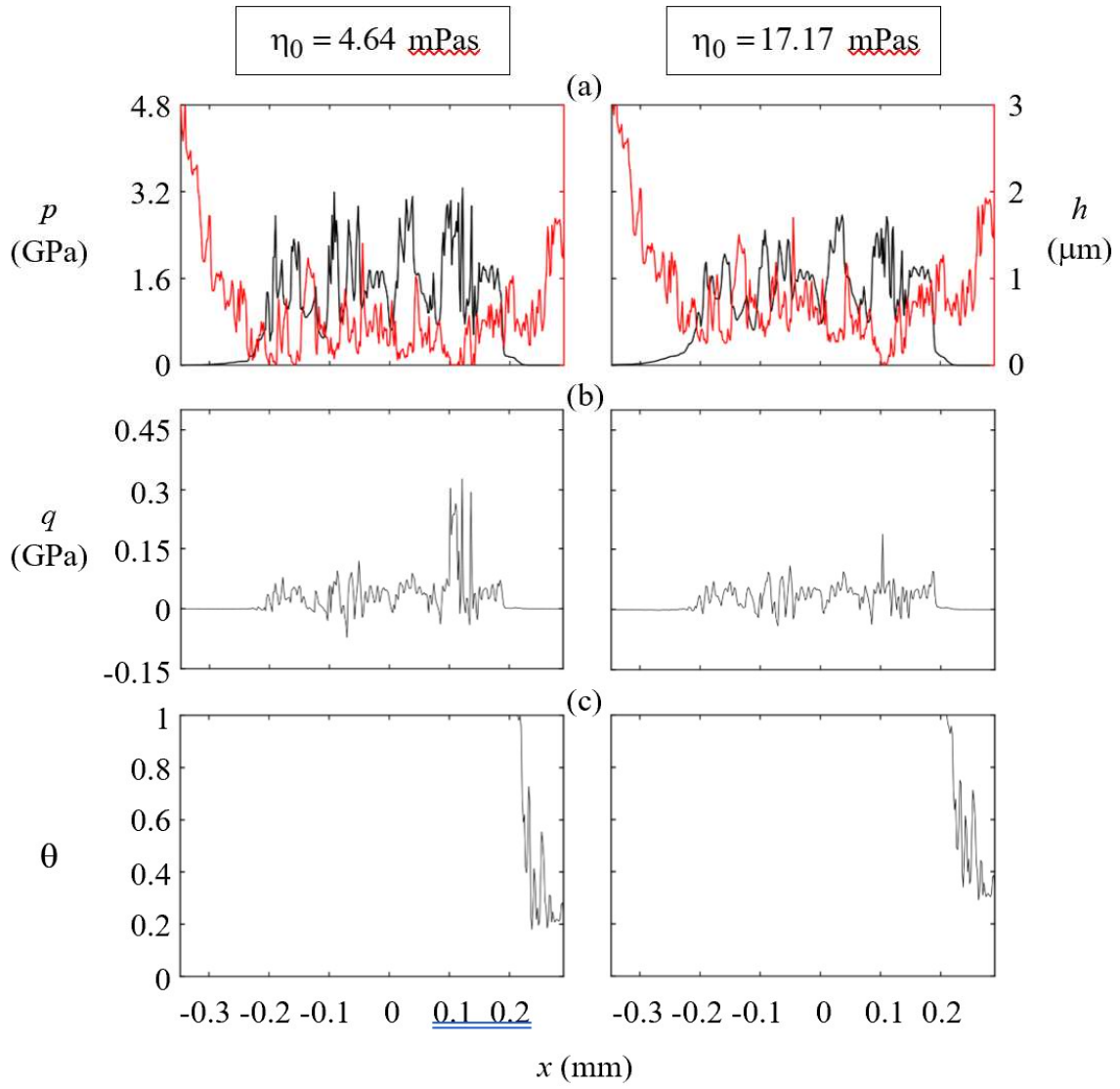

Figure 16 Transient distributions of (a) contact pressure (black) and lubrication film thickness (red), (b) surface shear, and (c) film fraction parameter for surface of $R_q = 0.3\mu m$ operating under $p_h = 1.75$ GPa and $h^{in} = 10\mu m$.

Table 3 Simulation matrix.

Hertzian Pressure, p_h, (GPa)		1.75, 2.0
Hertzian Half-Width, a_h, (mm)		0.23, 0.27
Ambient Low-shear Viscosity, η_0, (mPas)		4.64, 17.17
Rolling Velocity, u_r, (m/s)		10
Slide-to-roll Ratio, SR		-0.5
RMS Roughness Amplitude, R_q, (μm)		0.3, 0.5
Supplied Inlet Film Thickness, h^{in}, (μm)	$R_q = 0.3 \ \ \mu m$	0.2, 0.4, 0.6, 1.0, 1.4, 1.8, 2.3, 3.0, 6.0, 10.0
	$R_q = 0.5 \ \ \mu m$	0.2, 0.4, 0.6, 1.0, 1.8, 2.3, 3.0, 4.0, 6.0, 10.0

As shown in Figure 17, both the maximum contact pressure, $p_{\max}$, and the average film thickness within the nominal Hertzian zone, which is defined as $h_{avg} = \int_{-a_h}^{a_h} (\theta h) dx \Big/ (2a_h)$ with a_h representing the half Hertzian width, fluctuate with time largely. Considering this period in Figure 17, the median maximum contact pressure, $\overline{p}_{\max}$, and the median average film thickness, $\overline{h}_{avg}$, are observed to decrease from 3.95 GPa to 3.29 GPa and increase from 0.386 μm to 0.603 μm, respectively, when the lubricant viscosity is raised from the baseline.

Calculation of average film thickness is later used to monitor starvation initiating.

The amount of lubrication at the inlet is not a correct parameter to define starvation, as in the inlet region even with a lower value of h^{in} still lubrication film thickness is high. therefore, the average value of lubrication thickness throughout the entire contact zone is considered. As displayed in Figure 17 this average value is relatively constant with time, enabling simulation to be done based on average film thickness. As displayed in the last row of Figure 16 lubrication film thickness in the vicinity of the inlet is at its maximum of $10\mu m$, moving away from inlet θ starts to become below 1, with film thickness reduction in the x-direction .

As the loaded contact pair rolls against each other, material points, P_i ($i = 1, M$), at a certain depth, *y*, pass through the computational domain at the velocity u_1, for contact body 1, as illustrated in Figure 6

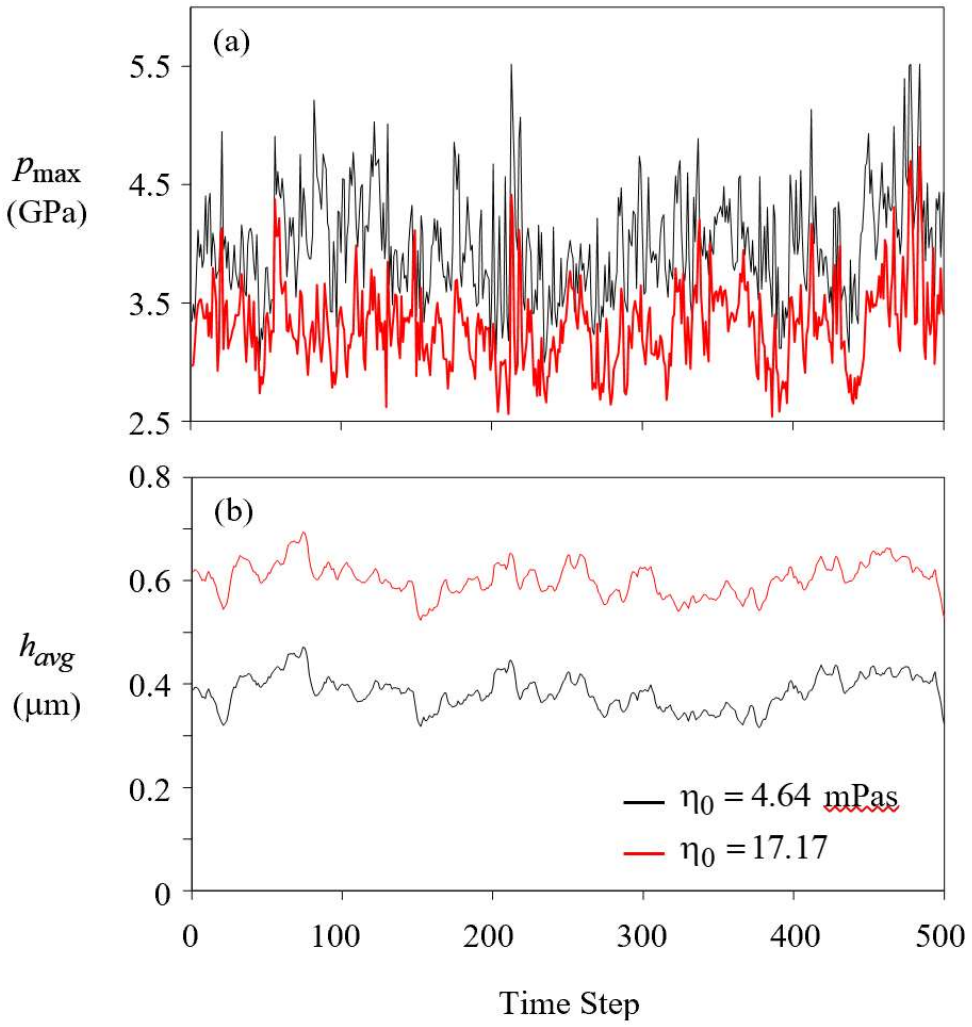

Figure 17 Variations of (a) maximum contact pressure, and (b) Hertzian zone average film thickness with time for the surface of $R_q = 0.3\mu m$ operating under $p_h = 1.75$ GPa and $h^{in} = 10\mu m$.

Owing to the time-varying contact pressure and tangential shear, each material point experiences different histories of multi-axial stress components. The associated fatigue damages and fatigue lives are, thus, different as well, although located at the same depth, and were observed to follow a normal distribution [74]. As shown in Figure 17, the pressure and shear peaks are significant for rough surface contacts, which lead to severe near-surface stress concentrations as depicted in Figure 18 at one example time instant under the baseline condition The stress amplitudes are seen to reach maxima at the surface for the normal components. As for the shear stress, σ_{xy}, local maximum amplitudes appear at both the surface and the subsurface location at $y = 0.5$ mm. This roughness-induced near-surface stress concentration has been shown to be responsible for the surface-breaking crack nucleation [54], [65], [73], [74]. In this study, the median fatigue life at the surface, $\bar{N}_{f0} = \bar{N}_f\big|_{y=0}$, is also found to be the minimum along the depth direction, and, therefore, used to represent the crack nucleation life.

With the reduction of temperature under baseline conditions, however, lubrication film thickness for the flooded condition will increase.

Unlike rough surface contact where asperities create surface stress, in the case of polished surfaces maximum amplitude of shear stress begins in the subsurface leading to subsurface-initiated failure.

Therefore, its lubrication and surface roughness that decides whether pits initiate from the subsurface or on the surface, they are two competing parameters on fatigue life calculation.

For the 80 simulations defined in Table 3, the predicted crack nucleation fatigue lives are compared in Figure 19, where both axes are on the $\log_{10}$ scale, showing the relationship between $\bar{N}_{f0}$ and h^{in}. The left and right columns of the figure represent the simulation results with surface roughness amplitudes of $R_q = 0.3 \ \mu m$ and $0.5 \ \mu m$, respectively.

and the top and bottom rows correspond to the low and high loading conditions, respectively. For all the four roughness and load combinations, it is seen the fatigue life is not largely impacted initially as the supplied inlet lubrication film thickness decreases until h^{in} reaches a sufficiently small value, which is referred to as the first threshold, h_1^{in} (displayed for the curve under $R_q = 0.3 \ \mu m$, $p_h = 1.75$ GPa, and $\eta_0 = 4.64$ mPas).

The linearity of fatigue life before h^{in} indicates the importance of average film thickness calculation for the simulation. as the indicator of overall lubrication film thickness for the entire contact surface. And explains for this operating condition how much inlet lubrication is needed to initiate starvation.

In experimental studies, the amount of lubrication needed to simulate starvation is often difficult to measure and requires trials to create different lubrication region essentially when variable like surface roughness is involved. The steep increase of friction coefficient is used by the reduction of lubricant flow to contact position. This method involves trials for different speed and loading conditions and is specified under each running condition.

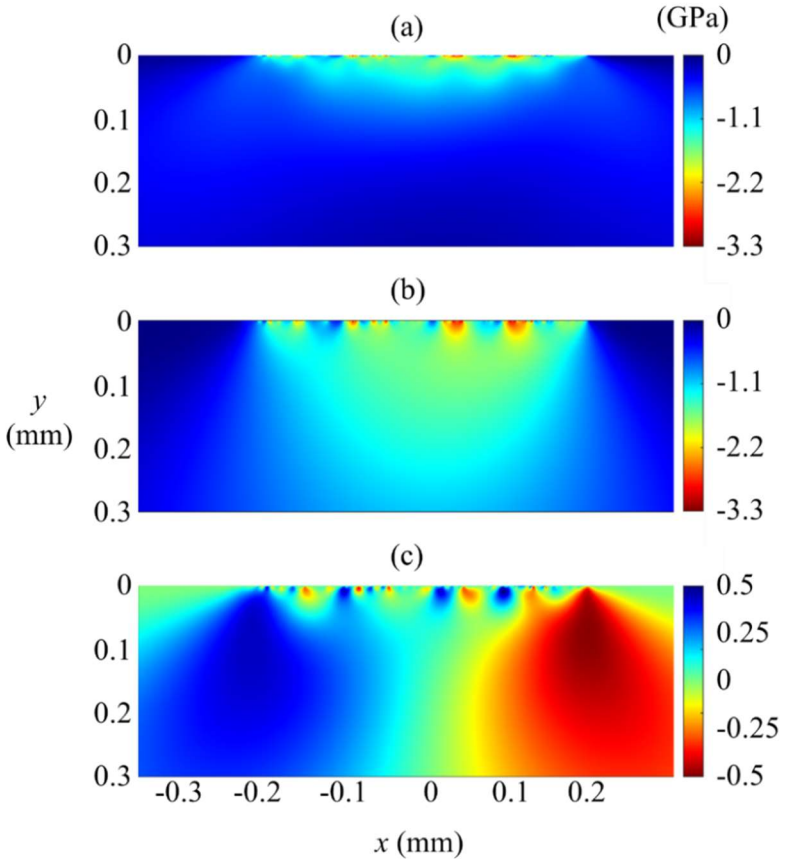

Figure 18 Distributions of (a) σ_x, (b) σ_y, and (c) σ_{xy}, under surface pressure and shear conditions defined in the left column of Figure 16.

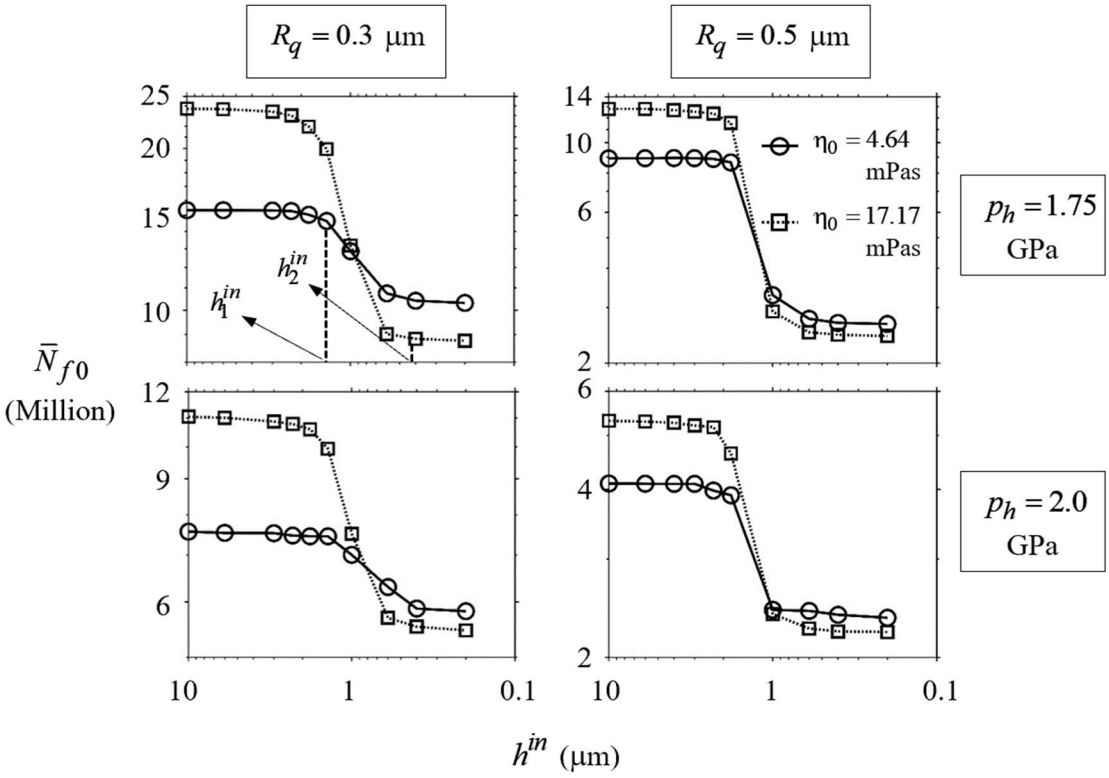

Figure 19 Variations of median fatigue life, $\bar{N}_{f0}$, with supplied inlet film thickness, h^{in}

Left and right columns represent simulations with low and high roughness amplitudes, respectively. Top and bottom rows represent simulations with low and high pressures, respectively

Below this first threshold, a sharp reduction in $\bar{N}_{f0}$ is initiated. However, this steep trend does not continue after h^{in} drops below a smaller second threshold, h_2^{in} (displayed for the same curve as for h_1^{in}). This behavior is in line with the experimental observation of Ref. [75]

The reason for such a non-linear relationship is explored utilizing Figure 20 where the median of Hertzian zone average film thickness, $\bar{h}_{avg}$, is plotted against h^{in}. Considering the baseline simulation, i.e. the first data point of the solid curve in the top left plot, the Hertzian zone average film thickness under this fully flooded lubrication condition is $\bar{h}_{avg}^{\text{fld}} = \bar{h}_{avg}\big|_{h^{in}=10\ \mu\text{m}} = 0.386\mu m$ .under lower temperature where viscosity is higher average lubrication film thickness is almost $0.2\mu m$ more than film thickness at the higher temperature, and this trend continues till fist threshold for h^{in}, indicating the impact of viscosity on lubrication regime.

By getting closer to starvation where h^{in} reaches the second threshold, this trend does not follow anymore. Under different viscosities average film thickness for higher and lower viscosity merge, indicating the insufficient lubricant flow to the region. This transition occurs close to when $h_1^{in} = 1$

Such behavior is the result of asperity contact for both cases of smooth and rough surfaces. As h^{in} decreases from its baseline value of 10 μm while still being above the first threshold of $h_1^{in} = 1.4\ \mu m$, $\bar{h}_{avg}$ is barely affected, since the supplied film thickness, h^{in}, is much larger than $\bar{h}_{avg}^{\text{fld}}$ and thus no starvation is induced

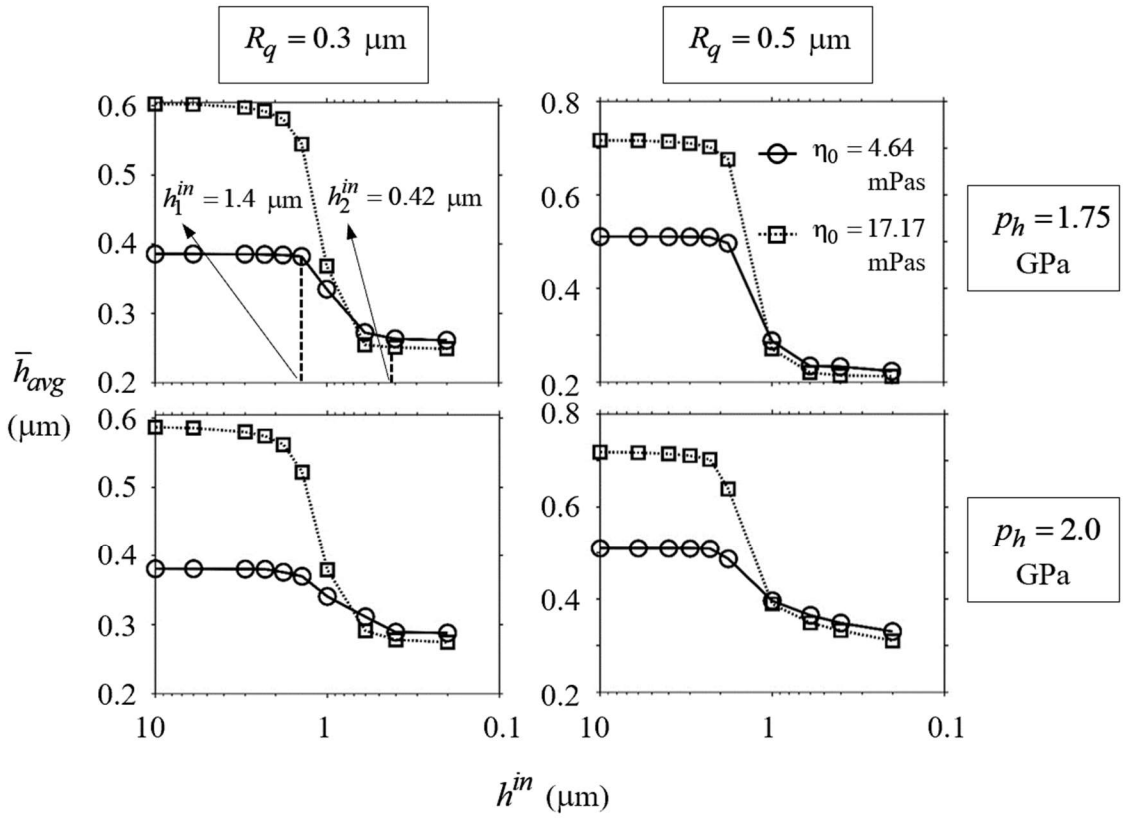

Figure 20 Variations of median Hertzian zone average film thickness, $\bar{h}_{avg}$, with supplied inlet film thickness, h^{in}. Left and right columns represent simulations with low and high roughness amplitudes, respectively. Top and bottom rows represent simulations with low and high pressure respectively

When h^{in} drops below h_1^{in}, it becomes more comparable to the fully flooded average film thickness, under which circumstance, starvation was reported to start to impact the lubrication film thickness within the contact zone [76]–[78]

For h_2^{in}, below which the curves return to their initial flatness, it was found to be closely related to the composite surface roughness RMS amplitude, R_q^c [79]. In this study, $R_q^c = 0.42\ \mu m$ and $0.71\ \mu m$ for the two roughness profiles considered. The left and right columns of Figure 20, h_2^{in} is observed to be in the vicinity of $0.42\ \mu m$ and $0.71\ \mu m$, respectively.

Below this second threshold that is defined by roughness, the two surfaces in contact do not allow further large rigid body approach to ensure the equilibrium of Eq (29) is maintained [79]Consequently, the Hertzian zone average film thickness decreases very slightly after h^{in} drops below h_2^{in}.

Value of h_2^{in} .also provides insight to starvation condition comparison of smooth and rough surface, for smooth surface with $R_q = 0.3\ \mu m$ second flatness occurs farther away from $h^{in} = 1\mu m$ whereas for $R_q = 0.5\mu m$ flatness happens closer to $h^{in} = 1\mu m$. At higher pressure, this phenomenon is more evident than at lower pressure, where $\overline{h}_{avg}^{\text{fld}}$ is above $0.2\mu m$ providing h_1^{in} of the approximately same value. This trend emphasizes the importance of surface finish on the starvation threshold.

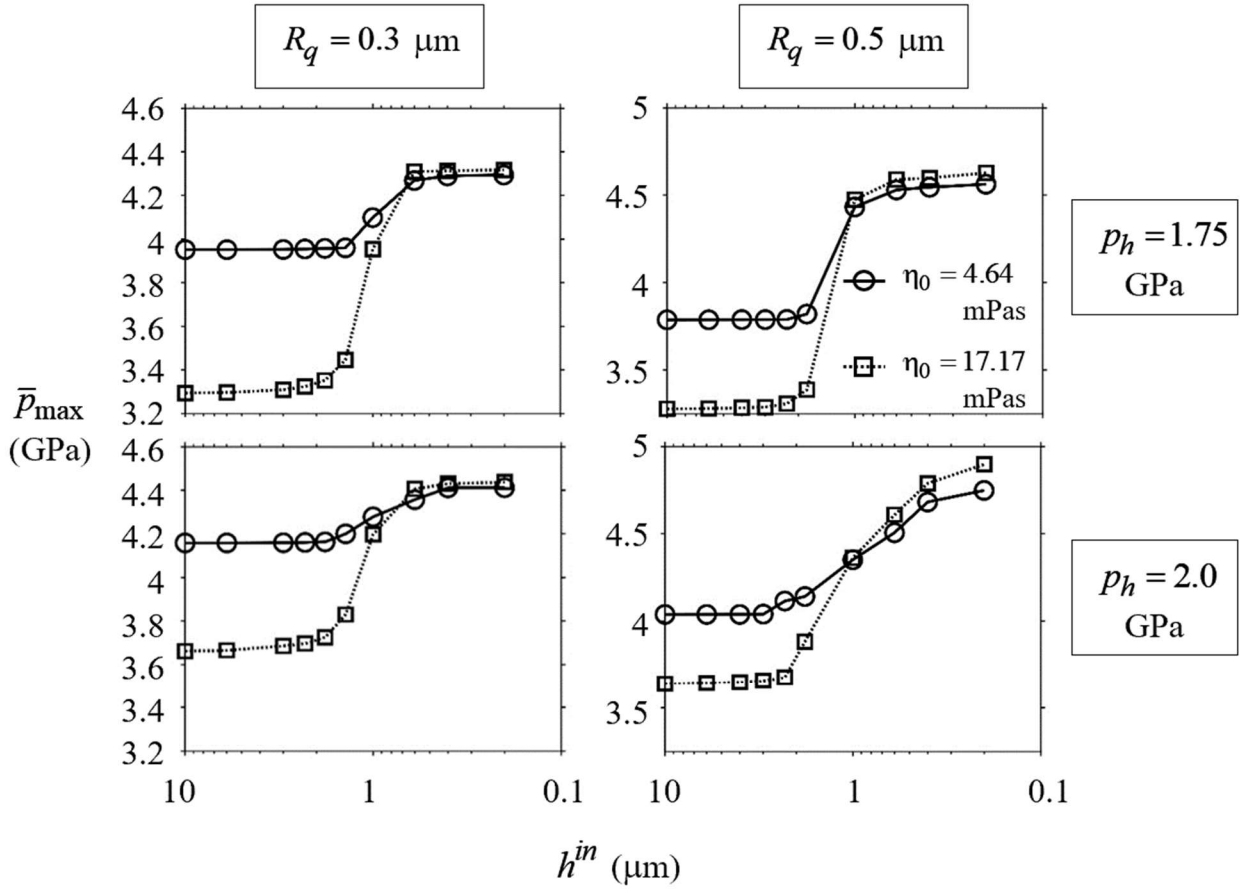

Figure 21 Variations of median maximum contact pressure, $\bar{p}_{max}$, with supplied inlet film thickness, h^{in}. Left and right columns represent simulations with low and high roughness amplitudes, respectively. Top and bottom rows represent simulations with low and high pressure respectively.

Recognizing the inverse relationship between contact pressure and lubrication film thickness, as well as between surface shear and film thickness, the variation of $\overline{h}_{avg}$ within Figure 20 leads to the patterns of pressure dependence and friction dependence on h^{in}, as shown in Figure 21 and Figure 22, respectively.

As shown in figure Figure 21 for smooth surfaces, in flooded conditions the gap between maximum contact pressure between high viscosity oil and low viscosity oil is more evident than in starved conditions. Under the fully flooded condition, lubrication film develops and further separates contact surfaces, avoiding asperity contact. whereas, at higher temperatures with lower viscosity lubrication film is thinner for the same amount of inlet, increasing the probability of more asperity contacts.

As the h_{in} approaches 1 the gap between contact pressure for both high and low viscosity oil reduces, this phenomenon is in line with experimental results under highly starved conditions.

A similar trend is valid for rough surface contact with only one difference at higher pressure where maximum contact pressure tends to rise with the severity of starvation as opposed to the smooth surface under high pressure. this is a result of asperity contact, starvation, and contact pressure.

An increase in contact pressure initiates more asperity contact and when the lubrication is starved this occurrence further is encouraged, escalating contact pressure value in the contact zone as opposed to other cases.

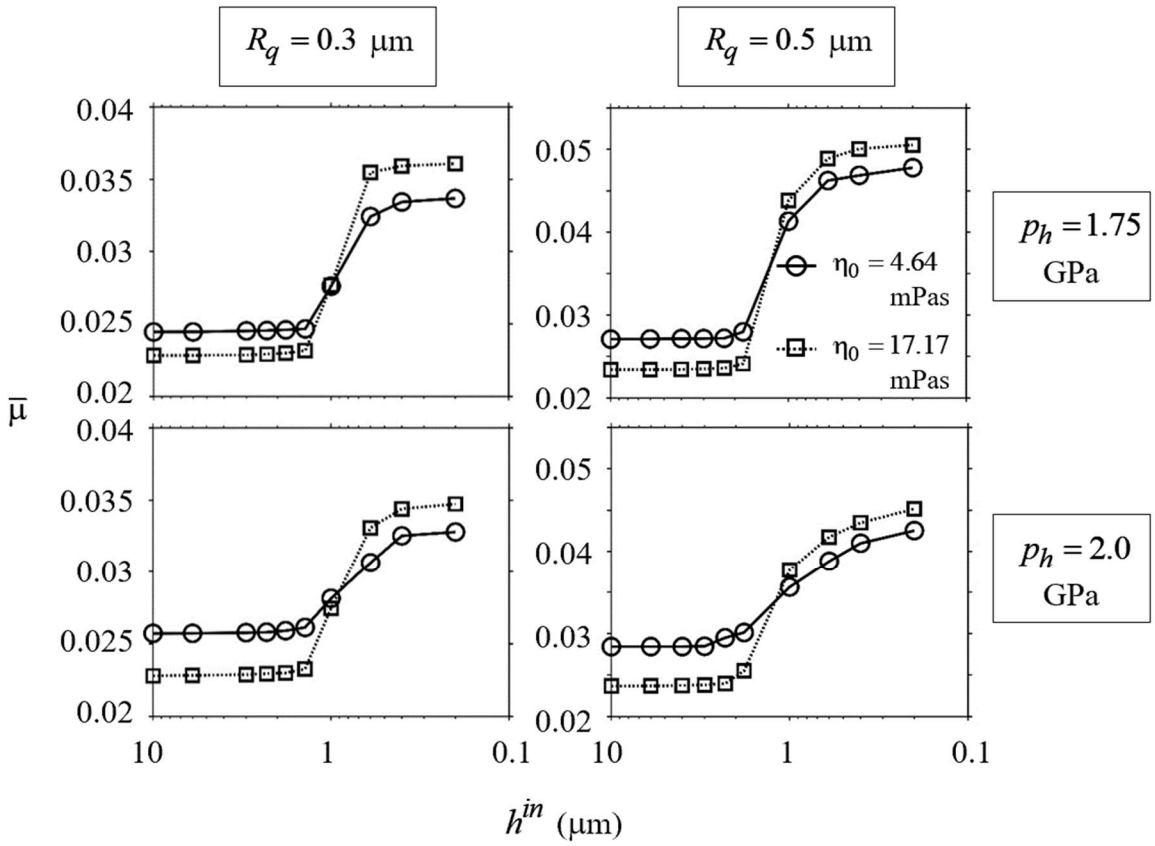

Figure 22 Variations of median friction coefficient, $\bar{\mu}$, with supplied inlet film thickness, h^{in} . Left and right columns represent simulations with low and high roughness amplitudes, respectively. Top and bottom rows represent simulations with low and high pressure

Similarly, the same trend follows with friction coefficient data, with an interesting flip of COF under flooded conditions compared to starved lubrication conditions.

In all cases with the increase of starvation level bypassing the second threshold h_{in} of friction coefficient value reverses for the oil with higher viscosity. Under the sufficiently lubricated condition, the oil with a higher viscosity friction coefficient is lower than the oil with lower viscosity, which is in line with the fact that thicker oil provides better lubrication.

However, under starved lubrication conditions, thicker oil doesn't perform better than thinner oil in terms of friction coefficient. And surprisingly the trend is reversed, the friction coefficient gets larger for more viscous oil at starvation. This phenomenon is in line with data shown in Figure 19 , for the fatigue life of rollers under starved lubrication conditions. Further explains the reverse trend in fatigue life under two different viscosity levels when starvation is in progress.

Similarly, as explained in Figure 21 for median contact pressure under starved lubrication and high pressure, in Figure 22 friction coefficient keeps its positive sloop. At higher contact pressure and starved level, the friction coefficient curve tends to rise with starvation level increase. As explained for median pressure conditions, the impact of higher contact pressure and starvation together creates more asperity contact in the contact zone, as compared to other case scenarios. Both the median of maximum contact pressure, $\overline{p}_{\max}$, and the median of friction coefficient, $\overline{\mu}$, are raised sharply only between the two thresholds of the supplied inlet lubrication film thickness, therefore, resulting in the fatigue life behavior in Figure 19.

Table 4 Median fatigue life, $\bar{N}_{f0}$, summary for viscosity effect comparison

$\bar{N}_{f0}$ (Million)			$R_q = 0.3\mu m$			$R_q = 0.5$		
			η_0 (mPas)		$\bar{N}_{f0}$ Improvement (%)	η_0 (mPas)		$\bar{N}_{f0}$ Improvement (%)
			4.64	17.17		4.64	17.17	
$p_h = 1.75$ (GPa)	h^{in} μm	10	15.34	23.71	54.6	8.92	12.80	43.5
		0.2	10.31	8.77	-14.9	2.66	2.44	-8.2
$p_h = 2.0$ (GPa)	h^{in} μm	10	7.56	11.05	46.2	4.10	5.31	29.5
		0.2	5.82	5.46	-6.2	2.36	2.22	-5.9

For example, under the surface condition of $R_q = 0.3 \ \mu m$ and low load condition of $p_h = 1.75$ GPa, the fatigue life is effectively increased from 15.34 million cycles to 23.71 million cycles (a 54.6 % rise) under a fully flooded lubrication condition at $h^{in} = 10$ mm, by implementing a higher viscosity. However, at $h^{in} = 0.2 \ \mu m$, where the lubrication is severely starved, the life is reduced from 10.31 million cycles to 8.77 million cycles, leading to a 14.9 % decline, when η_0 is raised from 4.64 mPas to 17.17 mPas. The fatigue life changes under the other three roughness and load combinations are recorded and compared in Table 4.

To find the underlying physical cause of the reverse effect of lubricant viscosity on fatigue under lubrication starvation, Figs. 18,19,20 are reviewed for the behavior of film thickness, pressure, and friction when viscosity is varied. Adopting a higher viscosity, it is seen the film thickness is generally higher before severe starvation takes place, however, becomes

lower afterward. This lower film thickness leads to the higher pressure as shown in Figure 21, and contributes to the higher surface shear (more asperity interactions) as shown in Figure 22. Additionally, the higher viscosity directly affects the friction by increasing the viscous shear within the fluid areas. For a more detailed illustration, the transient tribological behavior under the two viscosity conditions is compared, in Figure 23, for the smoother rough surface operating under the low load and the most starved lubrication condition, i.e. $p_h = 1.75$ GPa and $h^{in} = 0.2\mu m$. More asperity contacts are observed when are increased from 4.64 mPas to 17.17 mPas to introduce sharp increases in both pressure and surface shear peaks.

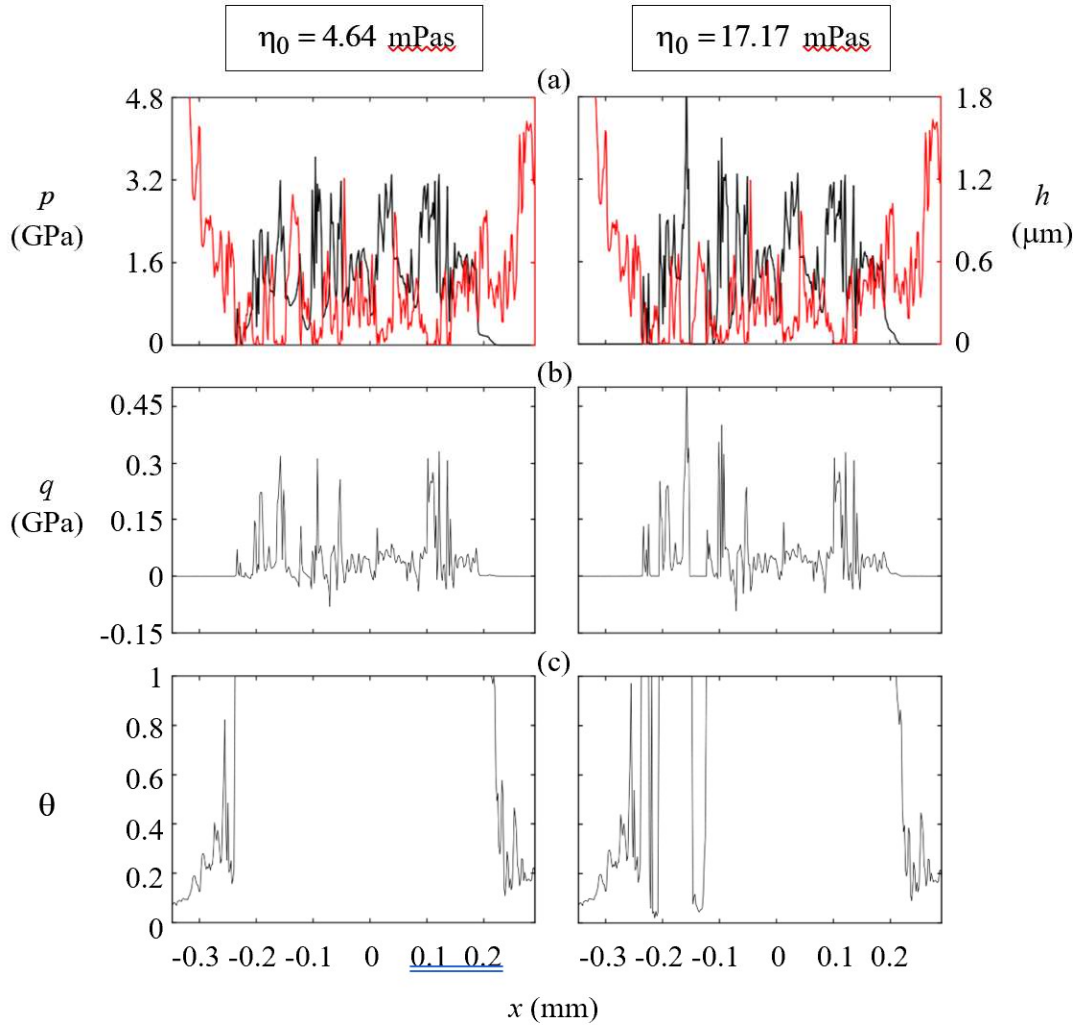

Figure 23 Transient distributions of (a) contact pressure (black) and lubrication film thickness (red), (b) surface shear, and (c) film fraction parameter for surface of $R_q = 0.3\mu m$ operating under $p_h = 1.75$ GPa and $h^{in} = 0.2\mu m$.

The local cavitation at $x = -0.135$ mm, in the right plot of Figure 23, is responsible for the highest *p* and *q* peaks when $\eta_0 = 17.17$ mPas is implemented. The elevated *p* and *q* directly impact the multi-axial stress fields and thus lead to lower fatigue lives in Figure 19, under highly starved lubrication conditions.

These reverse effects of lubricant viscosity on film thickness, pressure, shear, and fatigue life, under lubrication starvation, contradict the widely accepted EHL rules under fully flooded lubrication conditions, which state higher viscosity leads to better lubrication performance in terms of film thickness and failure prevention [74].

In light of the experimental measurements of film thickness by Cann [50], this contradiction seems to be valid. It was shown by the experiments that absolute film thickness was actually increased by moving from high viscosity base oil to a lower one when starvation was in effect [50]. It is postulated the supplied inlet lubrication film thickness, h^{in}, may not be a good measure of the extent of starvation. Instead, the ratio of the supplied film thickness to the fully flooded lubrication film thickness, $\chi_h = h^{in} / \bar{h}_{avg}^{\text{fld}}$, maybe a better indicator.

For instance, considering the low load and low roughness amplitude combination in Figure 19, the fully flooded lubrication condition leads to the Hertzian zone average film thickness $\bar{h}_{avg}^{\text{fld}} = 0.386 \mu m$ and 0.603 μm for $\eta_0 = 4.64$ mPas and 17.17 mPas, respectively. It can be stated, alternatively, that $\bar{h}_{avg}^{\text{fld}} = 0.386$ μm and 0.603 μm are required for fully flooded lubrication under the low and high viscosity conditions, respectively. Thus, with the same supplied fluid film thickness of $h^{in} = 0.2$ μm, χ_h yields 0.52 for the low viscosity case,

which is much higher than $\chi_h = 0.33$ for the high viscosity condition. The higher χ_h ratio means more lubricant supply about the required amount of lubricant for fully flooded lubrication, leading to thicker $\overline{h}_{avg}$ in Figure 20, lower $\overline{p}_{\max}$ in Figure 21 lower friction in Figure 22, and therefore higher fatigue life in Figure 19.

Another interesting behavior of the film thickness, recorded in Figure 20 (upper row versus lower row), is that, under fully flooded conditions, the film thickness under lower load is slightly higher than that under higher load, which is as expected; however, under starved lubrication condition, the film thickness becomes smaller when the load is decreased. This reverse phenomenon can be explained in a similar way that explains the reverse film thickness behavior under low and high lubricant viscosities. The average film thickness under fully flooded conditions for the low load case is higher than that for the high load case, indicating the former requires more lubrication fluid than the latter. Thus, with the same amount of limited lubricant supply, the low load case experiences more severe starvation, resulting in lower average film thickness in the nominal Hertzian zone. Additionally, a higher load contributes to the faster establishment of pressurized EHD fluid film in the inlet zone when lubrication is starved.

As compared in Figure 24(c) for the rougher surface operating under $\eta_0 = 4.64$ mPas and $h^{in} = 1.0\mu m$, for instance, the fluid film fraction parameter, θ, climbs to the value of 1, i.e. pressurized EHD film is formed, at $x_{\text{menicus}} = -0.22$ mm for the low load case, and -0.32 mm for the high load scenario. Using the half Hertzian widths of the two loads of $a_h = 0.23$ mm and 0.27 mm, the normalized inlet meniscus location,

$\bar{x}_{\text{menicus}} = x_{\text{menicus}} / a_h = -0.96$, and -1.18, respectively, for the low and high load conditions. This more effective EHD film formation under higher load is believed to be also responsible for the higher film thickness when lubrication is starved. It is noted, although with the higher film thickness, the larger pressure and shear as shown in Figure 24(a) and (b) under higher load still leads to smaller fatigue lives as listed in Table 4 in comparison to the low load condition.

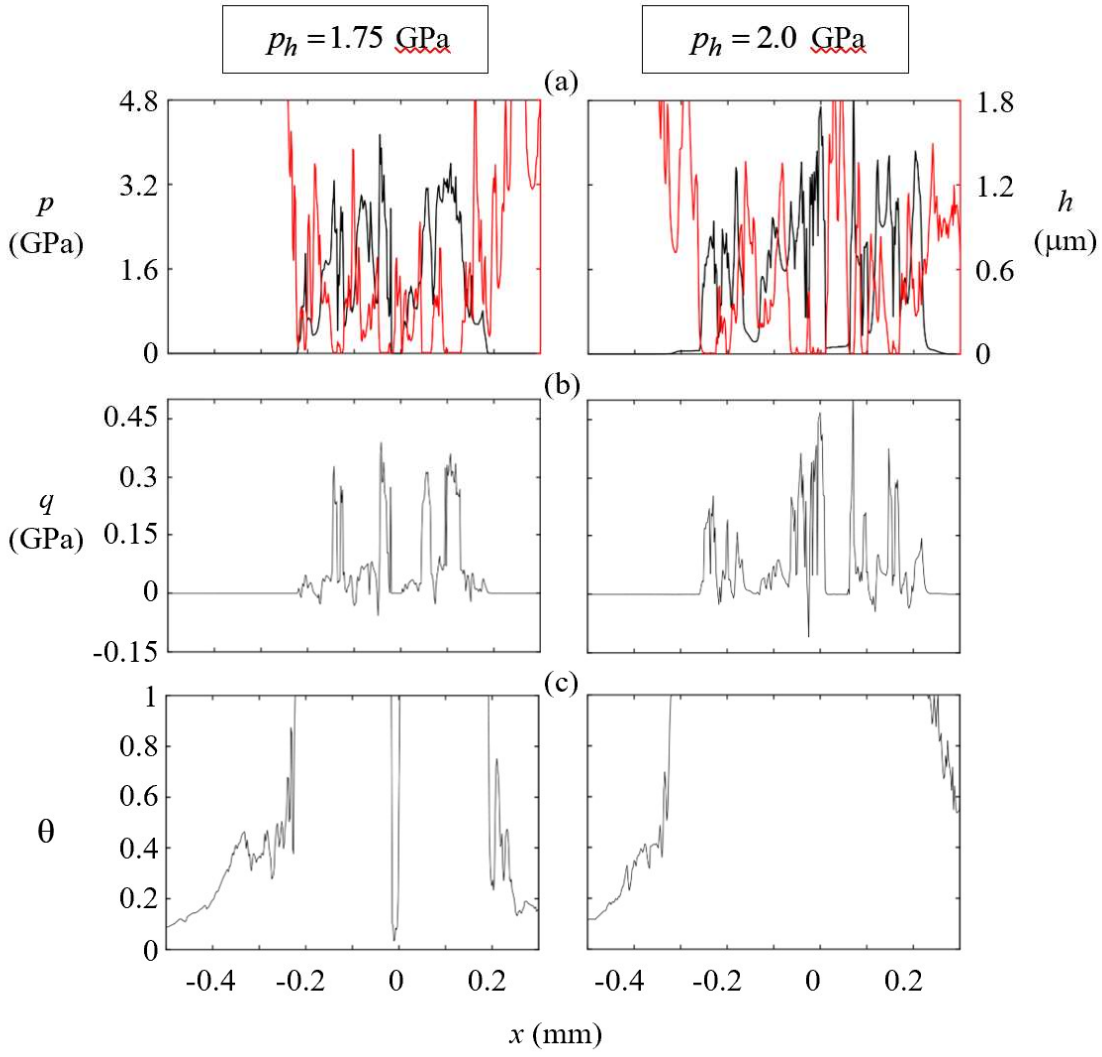

Figure 24 Transient distributions of (a) contact pressure (black) and lubrication film thickness (red), (b) surface shear, and (c) film fraction parameter for surface of $R_q = 0.5$ operating under $\eta_0 = 4.64$ mPas and $h^{in} = 1\mu m$.

Chapter 5. Conclusions and future work

5.1 Conclusions

This study contains two phases:

In the first phase, a Tribo-Dynamic model for line contact is proposed, linking dynamic response to the Tribology of contacting surfaces.

Reynolds equation was converged for each iteration of the equation of motion for contacting surfaces with the inclusion of surface pits.

The fluctuation of contact force caused by the surface pit excitation is used to determine the dynamic approach-displacement and approach-velocity. the values of approach velocity and approach distance are used in EHL simulation to get updated contact force values. New contact force values are used in the dynamic simulation for the next time instant.

Through sets of simulations in this phase, it is shown that large surface pits can create a large amplitude of excitation in the dynamic response of contacting bodies.

Displacement, contact force F_c, velocity, bearing force F_{b1}, and acceleration a_1 are compared for different pit sizes. as the pit size grows excitation amplitude has shown to become considerably large. When the pit size exceeds the nominal Hertzian zone, the maximum amplitude of approach displacement and approach velocity is observed to be $1.5\mu m$ and $26.5\frac{mm}{s}$, respectively. Leading to the following results:

- The maximum amplitude of F_c reaches 324 N, accounting for 12% of the nominal normal load, F_0. This significant dynamic contact force will accelerate the pit growth.
- The maximum amplitude of F_{b1} is seen to be 750 N that is 20% of F_0, even more significant in comparing to F_c, pointing to potential damage of supporting bearing under pitting failure.
- As for the acceleration signal the maximum amplitude is shown to approach 25g. In comparison with the other cases in Figure 14, the acceleration increment escalates substantially as the pit size increases. The very high sensitivity of a_1 to the surface pits dimension suggests an effective indicator of fatigue crack propagation. Figure 14 severs as a guideline on the relationship between pit size and acceleration amplitude.

In the second phase fatigue model for contacting roller under starved lubrication conditions is proposed. Incorporated with a film fraction parameter, a mixed lubrication formulation that is applicable for both fully flooded and starved lubrication conditions is employed to determine the surface normal pressure and tangential shear. The stress fields produced by these surface tractions are evaluated assuming a half-space contact problem since the contact zone is small in comparison to the body itself. Implementing a fatigue criterion, the amplitudes and mean of the multi-axial stress components are used to assess the fatigue damage.

Considering different surface roughness amplitudes, Hertzian contact pressures, and lubricant viscosities, parametric simulations are carried out within a range of supplied inlet

lubricant film thickness, which is varied to introduce different starvation severity. The observations are summarized as follows

- Significant fatigue life reduction occurs only when the supplied inlet lubrication film thickness is sufficiently small, say comparable to the average film thickness within the nominal Hertzian zone under fully flooded lubrication conditions.
- After the supplied inlet lubrication film thickness drops below the composite surface roughness RMS amplitude, further decreases in fatigue life become very limited.
- Regarding surface roughness and contact load effects on fatigue life, as expected, rougher surface and heavier load lead to lower fatigue life under both fully flooded and starved lubrication conditions.
- Surprisingly and interestingly, lower lubricant viscosity is shown to be able to elongate the fatigue life when lubrication is starved, which is opposite to the EHL rule under fully flooded lubrication conditions, stating higher viscosity results in thicker lubrication film and improved fatigue life. However, it is in line with the experimental observation [1], where film thickness was shown to increase when moving from high viscosity base oil to a lower one under starvation conditions.

It should be noted, that a constant boundary lubrication friction coefficient is assumed in this work. The dependence of this friction coefficient on the extent of starvation may be

tangible when starvation becomes very severe. Therefore, further fatigue life reduction may take place.

5.2 Future work

As an inseparable part of any numerical modeling, experimental validation is required to be performed for accuracy checking of the model.

The author only provides the approach required to perform these experiments in the lab along with the necessary equipment to capture vibration signals.

Tribometer

To perform the experimental validation of this study, a rolling tester tribometer is required. As displayed in Figure 25 , this tester has two spindles, upper and lower, powered by two electric motors capable of spinning up to $10^4(RPM)$. An axial force is applied with a hydraulic pump capable of generating $10^4\,N$ - which only can slide along designated racks and be kept at a constant set value. Calibrated standard compression-tension loadcell measures applied load and a built-in control unit keeps it constant at the desired value.

Specimens are kept in place using tapered holders both in the upper and lower spindle.

after setting up machine parameters (lubricant temperature, applied force, number of cycles, upper and lower disks diameter, spindles rpm, and sliding ratio) contacting bodies start engaging slowly while heated lubricant is injected between the two surfaces Figure 26.

The engagement process requires some time to stabilize for the load set value, data during this process is not recorded till the applied load reaches 95% of the set value, this will help to reduce measurement errors while monitoring the experiment process.

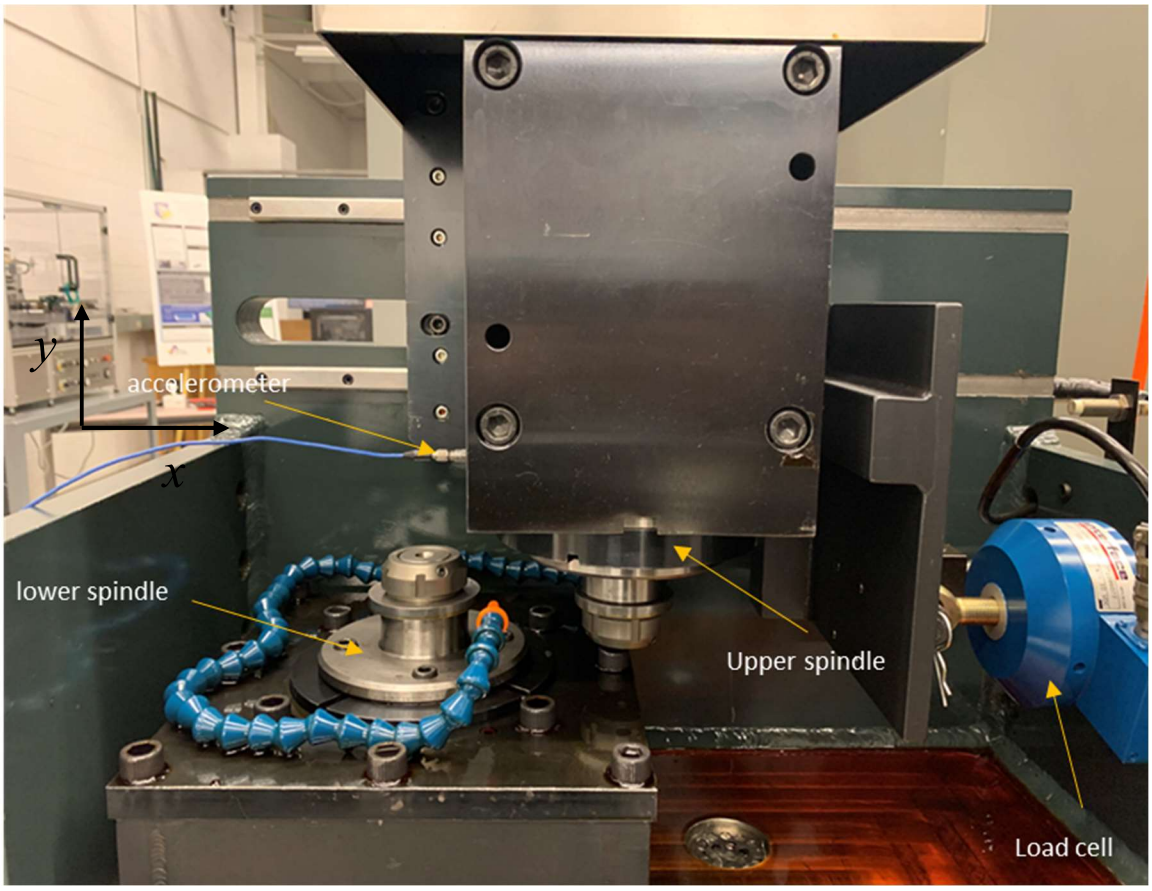

Figure 25 Rolling Tribometer

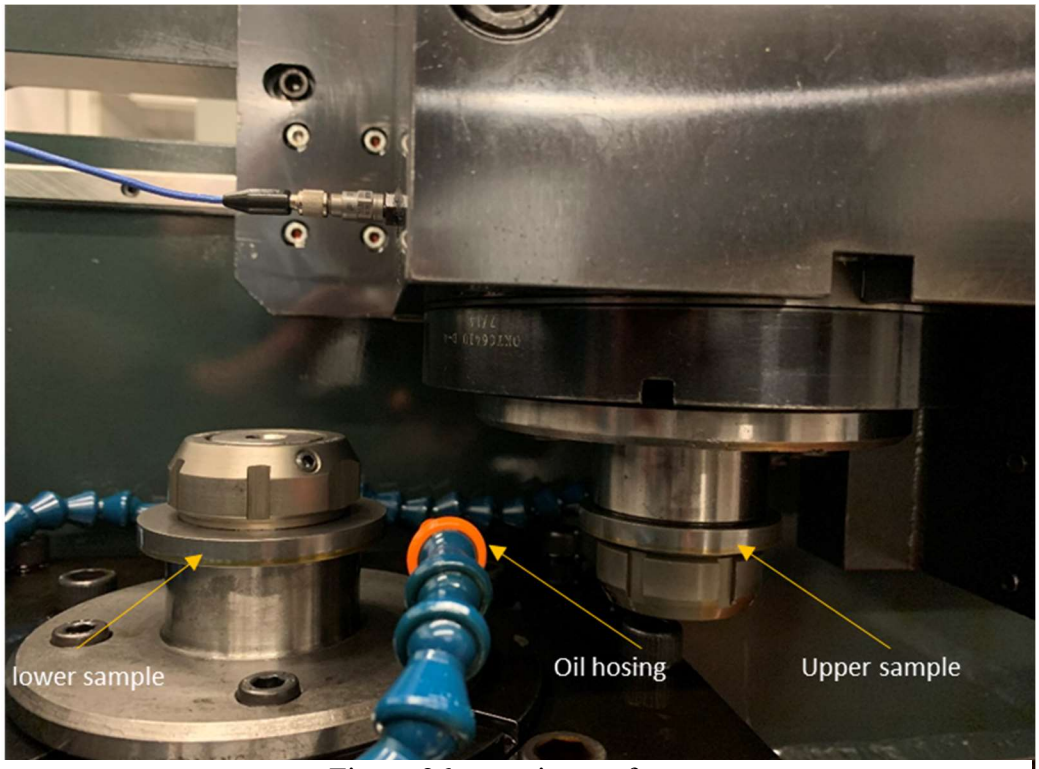

Figure 26 engaging surfaces

Lubricant is stored in a separate unit and kept at set up temperature-a liquid pump injects lubricant between surfaces-and it passes through filters to keep generated debris away from the lubricant

The lubrication flow rate is controlled by a flow valve which allows for simulating different lubrication conditions. To maintain hydrodynamic lubrication between contacting rollers, for example, the flow valve can be adjusted to the highest flow rate.

Specimens

Hardened steel (e.g., AISI 8620) is recommended for specimens' material. One specimen is axially crowned with a large axial radius while the conjugate part is flat. Creating a crown surface allows the starting contact to be point contact which by applying gradual load develops to line contact.

Figure 27 shows the recommended dimensions and geometry of the two contacting surfaces.

Disk Specimens are hardened to $60HRC$ and finished to $0.05\mu m$ using the ISF method. ISF, isotropic surface finishing, is an accelerated surface finish process in which a mixture of chemical components and hard mediums are used to remove surface peaks uniformly. Depending on the duration of the process and chemicals potency, the process may take a few minutes to hours.

undesirable waviness on surface topography can be reduced while surfaces are being polished during this process. A highly polished surface of $0.1\mu m$ is achievable with this process.

As the aim of this study is to model the vibration response of surfaces with defects, the main interest is to capture the vibration signals generated by surface pits and compare them with the normal condition in which no surface pits is developed as done in Chapter 2. Therefore, for validation purposes, a test matrix with incrementing pit size is recommended.

Table 5 allows monitoring of the effect of load, rolling speed, and temperature on the vibration response of defected surfaces.

Recommended normal force provides low, medium, and high Hertzian contact pressure. Temperature variation at inlet lube is the bulk temperature, which is a machine set up.

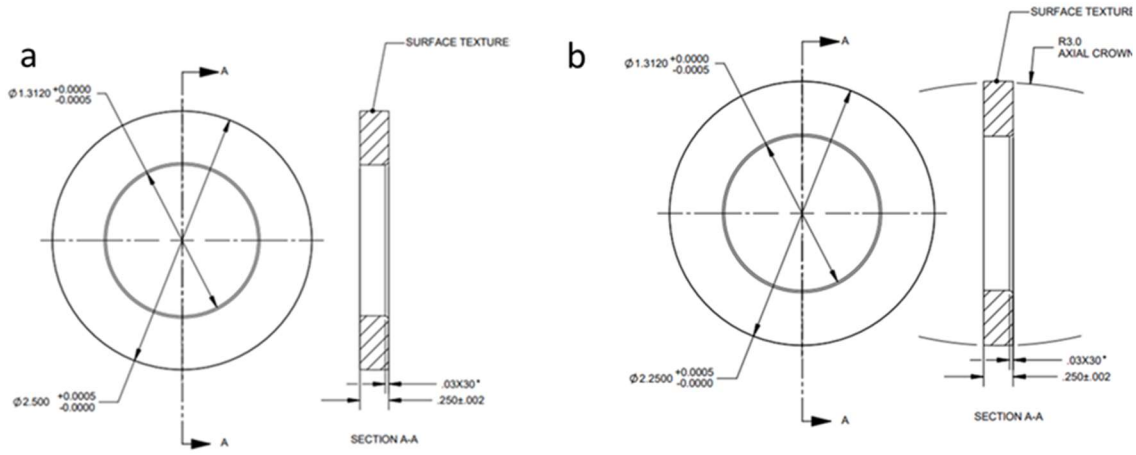

Figure 27 non-crowned disk specimen (a), crowned disk specimen (b)

Table 5 Recommended experiment test Matrix

Test #	Specimen SN		Pit Size (μm)	Rolling Speed (m/s)	Inlet Lub. Temperature (°C)	Hertzian Pressure, p_h (GPa)	Normal Force (N)
P1-T1-W1	NC-01	C-01	50	2, 4, 6, 8	50	1.3	900
P1-T1-W2	NC-02	C-02				1.5	1300
P1-T1-W3	NC-03	C-03				1.6	1700
P1-T2-W1	NC-04	C-04			70	1.3	900
P1-T2-W2	NC-05	C-05				1.5	1300
P1-T2-W3	NC-06	C-06				1.6	1700
P2-T1-W1	NC-07	C-07	100	2, 4, 6, 8	40	1.3	900
P2-T1-W2	NC-08	C-08				1.5	1300
P2-T1-W3	NC-09	C-09				1.6	1700
P2-T2-W1	NC-10	C-10			80	1.3	900
P2-T2-W2	NC-11	C-11				1.5	1300
P2-T2-W3	NC-12	C-12				1.6	1700
P3-T1-W1	NC-13	C-13	200	2, 4, 6, 8	50	1.3	900
P3-T1-W2	NC-14	C-14				1.5	1300
P3-T1-W3	NC-15	C-15				1.6	1700
P3-T2-W1	NC-16	C-16			70	1.3	900
P3-T2-W2	NC-17	C-17				1.5	1300
P3-T2-W3	NC-18	C-18				1.6	1700

accurate measurement of lubricant temperature at contact point requires more sophisticated measurement tools.

In order to capture the effect of different pit sizes, the dimension of pits must be controlled.

The experiment requires accurate dimensions for different pit sizes to be compared with model results. To create different surfaces with different pit sizes, several manufacturing methods can be implemented.

Wire EDM cutting method is a useful method for its accuracy and low cost. It allows controlling geometry to cut desired triangular shapes as discussed inChapter 2 while controlling the depth and width of pits based on Table 5.

One example pair of samples made of AISI 8620 is manufactured and the surface profile is measured for demonstration.

Figure 28 is a stereo microscope image of the pair $\#C-07, NC-07$ with $10X$ and $20X$ magnification at the applied pit location. The surface roughness of sample pair is imaged before and after embedding the surface pits. Figure 29 is the sample topography before the inclusion of the pit and Figure 30 is the sample's topography after embedding the surface pit with $30\mu m$ depth.

As Figure 30 shows, the EDM process deposits removed materials and creates two small bumps around the pit location. these bumps are a source of error in vibration analysis because they introduce extra waviness to the topography of the contacting surface.

Removing bumps is possible with one extra step of surface polishing, which is expected to produce closer results to simulation.

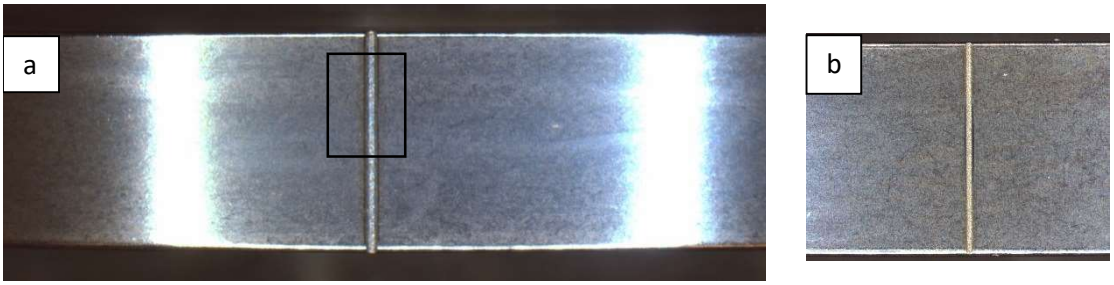

Figure 28 stereo image of generated pit taken with 10X lens (a), Stereo image of sample pit with 20X lens (b)

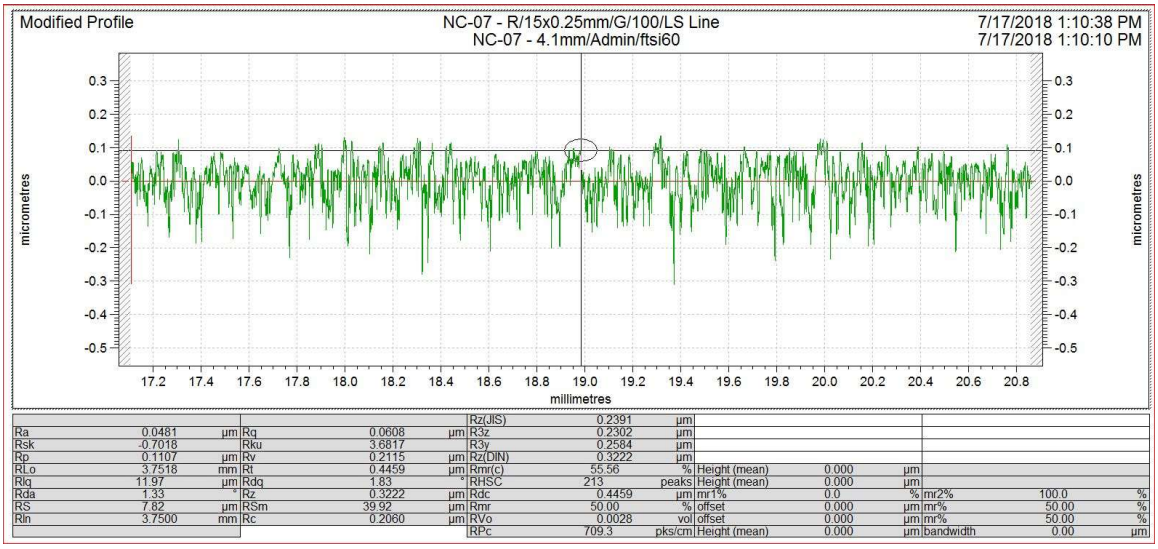

					Rz(JIS)	0.2391	µm						
Ra	0.0481	µm	Rq	0.0608	µm	R3z	0.2302	µm					
Rsk	-0.7018		Rku	3.6817		R3y	0.2584	µm					
Rp	0.1107	µm	Rv	0.2115	µm	Rz(DIN)	0.3222	µm					
RLo	3.7518	mm	Rt	0.4459	µm	Rmr(c)	55.56	%	Height (mean)	0.000	µm		
Rlq	11.97	µm	Rdq	1.83	°	RHSC	213	peaks	Height (mean)	0.000	µm		
Rda	1.33	°	Rz	0.3222	µm	Rdc	0.4459	µm	mr1%	0.0	%	mr2%	100.0 %
RS	7.82	µm	RSm	39.92	µm	Rmr	50.00	%	offset	0.000	µm	mr%	50.00 %
Rln	3.7500	mm	Rc	0.2060	µm	RVo	0.0028	vol	offset	0.000	µm	mr%	50.00 %
						RPc	709.3	pks/cm	Height (mean)	0.000	µm	bandwidth	0.00 µm

Figure 29 Roughness measurement of sample NC-07 before placing pit

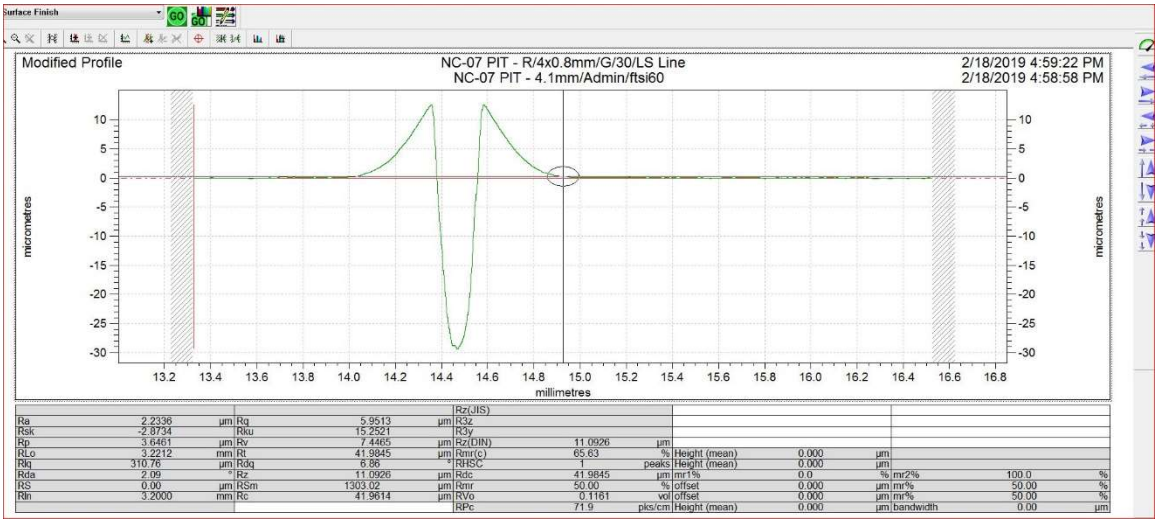

Figure 30 roughness measurement of sample NC-07 after placing pit

Data acquisition device

Embedded surface pits on the disk's surface generate different power spectrums for the rollers. The power spectrum is expected to be a function of machine and surface parameters: pit size, rolling speed, and load.

Each test number in Table 5, should provide a unique power spectrum that is used for modeling validation.

A portable signal analyzer (e.g., SingalCacl Ace Figure 31) is sufficient to record the power spectrum of rolling bodies, which is composed of the power of each signal as a function of frequency. In Figure 31, connected to the output channel of the device is a calibrated, single-axis piezoelectric accelerometer.

contacting rollers generate a frequency response of multiple degrees of freedom which is a superposition of a single degree of freedom modes as shown in forced vibration equations (1). Therefore, the signal of interest (resultant by pits) is extracted by comparing power spectrum signals before and after the creation of pits on rollers' surfaces.

Figure 31 SignalCalc Ace

Proposed models in this study numerically simulate the dynamic response of rolling surfaces with surface defects and fatigue life calculation under starved lubrication conditions.

Each model can be extensively used in Gears and bearing dynamic analysis and fatigue life calculation.

For the Tribo-Dynamic model.

- With the use of roller testers (tribometers) and under different operating conditions with speed, load, surface roughness, and lubrication change generated signals are recorded using data acquisition devices. Signals can be used for the validation of the model through sets of full factorial experiments.

Experimental validation of the model will provide sufficient information to check the accuracy of the model and apply modifications if needed.

- Proposed model then can be served as a tool to investigate the impact of parameters that experimentally is difficult to change or expensive to make.

Infinitesimal surface defects for example are difficult to generate experimentally on the surface and may need expensive processes. harsh operating conditions including very high temperature, high speed, or large contacting load are difficult to perform in laboratory conditions, whereas this model can be used for such conditions.

- Provided approach with minor modifications can be extended to journal bearings and cams experiencing vibration as a result of surface pits.

For fatigue life model

- Validation will require a roller tester with adjustable lubricant flow.
- Model can be extended to journal bearings, ball bearings, gears, and cams with minor modifications using a similar approach.
- Crack propagation also can be added to the model.

Appendix A. Surface parameters

different methods of surface roughness measurement (contact based, non-contact based) are Parameters associated with each measurement are described along with their corresponding equations.

Stylus Surface measurement

Stylus profilers are contact-based machines whose surface topography is measured by physical contact with samples. The stylus tip touches the specimen surface and topography along the line is measured while the stage moves Figure 32. depending on the probe diameter used for measurement this method can be somewhat inaccurate compared to the optical method. The accuracy of this method is highly sensitive to the selection of probe size and using correct filter values.

in order to reduce surface measurement errors, samples should be washed with alcohol-based cleaners before measurement and air-dried. Small particles or fingerprints on the surface can highly affect measurement accuracy.

Among different surface parameters, Surface roughness R_a and R_q are universally used to address the smoothness of surface topography.

$$R_a = \frac{1}{L}\int_0^L \left|Z(x)\right| dx \tag{41}$$

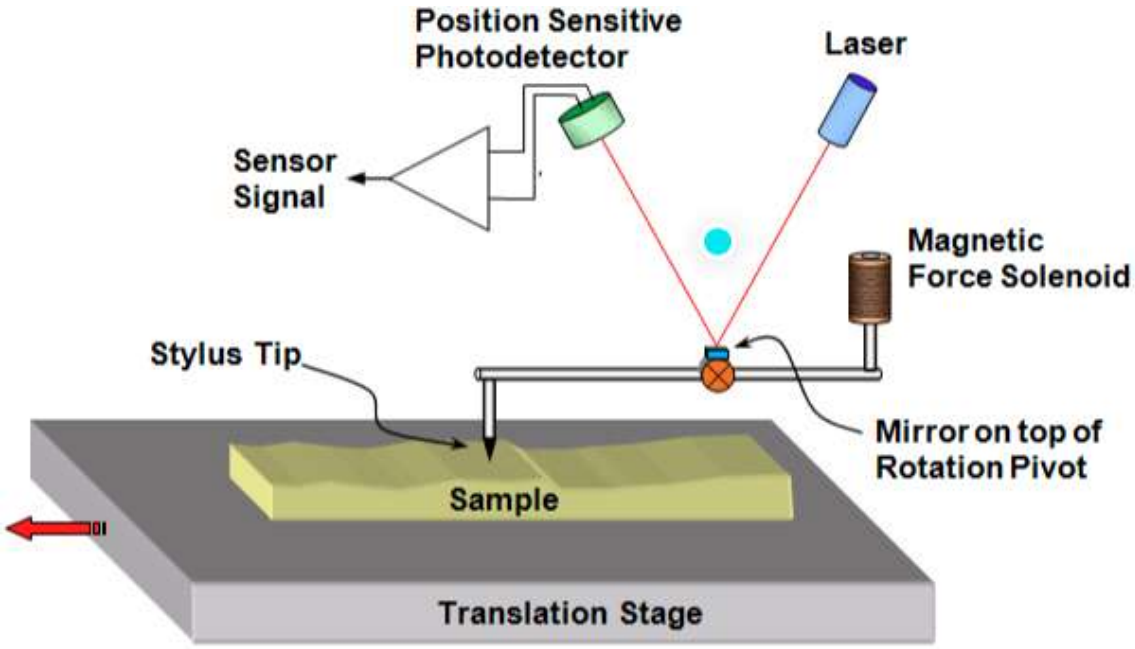

Figure 32 schematic of stylus topography measurement

As shown in Eq. (41) R_a represents the arithmetic mean of the absolute coordinate $z(x)$ within the sampling length, L. R_a provides stable results as the parameters are not significantly influenced by scratches contamination and measurement noise.

$$R_q = \sqrt{\frac{1}{L}\int_0^L Z^2(x)dx} \tag{42}$$

Whereas R_q represents the root mean square for $Z(x)$ within the sampling length, L .Both surface parameters are used interchangeably as a quantitative value for surface polishing. However, R_q due to the square term is less affected by surface defects. Surface defects can be the results of different types of surface failure or machining processes.

$$R_z = \frac{1}{n}\left(\sum_{i=1}^{n} p_i - \sum_{i=1}^{n} v_i\right) \tag{43}$$

As The international ISO system defines Ten-point height (R_z)the difference is in the average of five heigh peaks and five lowest valleys. This parameter is more sensitive to occasional high peaks. p_i and v_i are the ith peak and valley and n is the number of selected points.

Skewness (R_{sk}) of a profile addressed the surface valleys and peaks distribution. R_{sk} is positive for surfaces governed by valleys and negative for surfaces governed by peaks.

$$R_{sk} = \frac{1}{NR_q^{\,3}}\left(\sum_{i=1}^{N} Z_i^{\,3}\right) \tag{44}$$

This parameter is useful in friction assessment of applications where starvation is in progress. and often used on different surfaces with similar values R_a which may have different valley and peak distributions. In Eq (44), N is the number of samples , and Z_i is the height of the i-th sample point.

modification of surface parameters in starved lubrication conditions involves the generation of more valleys. This is to ensure the surface will have micro-level valleys for oil reserve.

Kurtosis (R_{ku}) of a surface profile addresses the sharpness of peaks on the surface. for values above 3, the surface is governed by sharp peaks and for values below 3 surface is not considered sharp.

$$R_{ku} = \frac{1}{NR_q^{\,4}}\left(\sum_{i=1}^{N} Z_i^{\,4}\right) \tag{45}$$

R_{ku} is used in applications where surface treatment is required to remove sharp peaks.

Tribo-conditioning of component surfaces in applications with severe wear issues includes removing peaks off the surfaces. This parameter is frequently measured during the process in time intervals to ensure the smoothness of peaks is achieved.

Optical surface measurement

Optical profilers are non-contact profilers in which $3D$ surface image is taken with the aid of objective lenses. Depending on desired resolution and surface features, different objectives ranging from $10X$ magnification to $50X$ magnification are commonly used.

Calculated surface parameters using optical profilers are more reliable than the stylus, primarily because surface features are calculated over a surface area than a line and surface topography can visually be observed for possible inconsistency.

However, the topography of the surface is impacted by the cleanness of the surface.

Counterparts of R_a and R_q which are 2-dimensional surface parameters are S_a and S_q with a similar equation. The only difference is these parameters are calculated over the entire surface, therefore more data points are involved in the calculation.

$$S_a = \frac{1}{A}\iint_A \left|Z\left(x,y\right)\right| dxdy \tag{46}$$

As shown in Eq.(46) this parameter expands the profile parameter R_a three-dimensionally.it represents the arithmetic mean of the absolute $z\left(x,y\right)$ within the evaluation area.

$$S_q = \sqrt{\frac{1}{A}\iint_A Z^2\left(x,y\right) dxdy} \tag{47}$$

As Eq.(47) shows, this parameter expands the profile parameter R_q three-dimensionally. It represents the root square for $Z\left(x,y\right)$ within the evaluation area.

$$S_{sk} = \frac{1}{S_q^{\,3}}\left[\frac{1}{A}\iint_A Z^3(x,y)dxdy\right] \tag{48}$$

Skewness (S_{sk}) of a surface is defined by Eq (48) . where A is the area of measurement, x and y are locations of the points in the x and y coordinate and Z is the corresponding height

. Similar to Eq (44) , Eq (48) is a metric for the distribution of height and valleys n the surface. With positive values for surfaces governed by valleys and negative values for surfaces governed by peaks. As this parameter is calculated over an area, the value is more accurate than its counterpart in the 2D dimension.

$$S_{ku} = \frac{1}{S_q{}^4}\left[\frac{1}{A}\iint_A Z^4(x,y)dxdy\right] \tag{49}$$

Kurtosis (S_{ku}) is defined by Eq(49), and is used as a metric to evaluate the sharpness of peaks similar to Eq (45). Surfaces with values above 3 are considered sharp and surfaces with values below 3 are considered non-sharp surfaces[80].

Bibliography

[1] T. H. Patel and A. K. Darpe, “Experimental investigations on vibration response of misaligned rotors,” *Mechanical Systems and Signal Processing*, vol. 23, no. 7, pp. 2236–2252, Oct. 2009, doi: 10.1016/j.ymssp.2009.04.004.

[2] V. K. Tamminana, A. Kahraman, and S. Vijayakar, “A Study of the Relationship Between the Dynamic Factors and the Dynamic Transmission Error of Spur Gear Pairs,” *Journal of Mechanical Design*, vol. 129, no. 1, pp. 75–84, Feb. 2006, doi: 10.1115/1.2359470.

[3] A. Kahraman and G. W. Blankenship, “Effect of Involute Tip Relief on Dynamic Response of Spur Gear Pairs,” *Journal of Mechanical Design*, vol. 121, no. 2, pp. 313–315, Jun. 1999, doi: 10.1115/1.2829460.

[4] A. Kahraman and G. W. Blankenship, “Interactions between commensurate parametric and forcing excitations in a system with clearance,” *Journal of Sound and Vibration*, vol. 194, no. 3, pp. 317–336, Jul. 1996, doi: 10.1006/jsvi.1996.0361.

[5] S. Li and A. Kahraman, “A tribo-dynamic model of a spur gear pair,” *Journal of Sound and Vibration*, vol. 332, no. 20, pp. 4963–4978, Sep. 2013, doi: 10.1016/j.jsv.2013.04.022.

[6] S. Li, “A thermal tribo-dynamic mechanical power loss model for spur gear Pairs,” *Tribology International*, vol. 88, pp. 170–178, Aug. 2015, doi: 10.1016/j.triboint.2015.03.022.

[7] S. Li and D. Masse, “On the flash temperature under the starved lubrication condition of a line contact,” *Tribology International*, vol. 136, pp. 173–181, Aug. 2019, doi: 10.1016/j.triboint.2019.03.038.

[8] S. Li and A. Anisetti, “A tribo-dynamic contact fatigue model for spur gear pairs,” *International Journal of Fatigue*, vol. 98, pp. 81–91, May 2017, doi: 10.1016/j.ijfatigue.2017.01.020.

[9] X. Liang, M. J. Zuo, and Z. Feng, “Dynamic modeling of gearbox faults: A review,” *Mechanical Systems and Signal Processing*, vol. 98. Academic Press, pp. 852–876, Jan. 01, 2018. doi: 10.1016/j.ymssp.2017.05.024.

[10] D. S. Shah and V. N. Patel, “A Review of Dynamic Modeling and Fault Identifications Methods for Rolling Element Bearing,” *Procedia Technology*, vol. 14, pp. 447–456, Jan. 2014, doi: 10.1016/j.protcy.2014.08.057.

[11] Lewicki, D. G., Dempsey, P. J., Heath G. F., and Shanthakumaran, “Gear fault detection effectiveness as applied to tooth surface pitting fatigue damage,” *NASA/TM*, vol. 215667, 2009.

[12] H. Öztürk, M. Sabuncu, and I. Yesilyurt, “Early Detection of Pitting Damage in Gears using Mean Frequency of Scalogram,” *Journal of Vibration and Control*, vol. 14, no. 4, pp. 469–484, Apr. 2008, doi: 10.1177/1077546307080026.

[13] C. K. Sung, H. M. Tai, and C. W. Chen, “Locating defects of a gear system by the technique of wavelet transform,” *Mechanism and Machine Theory*, vol. 35, no. 8, pp. 1169–1182, Aug. 2000, doi: 10.1016/S0094-114X(99)00045-2.

[14] A. Yoshida, Y. Ohue, and H. Ishikawa, “Diagnosis of tooth surface failure by wavelet transform of dynamic characteristics,” *Tribology International*, vol. 33, no. 3–4, pp. 273–279, Apr. 2000, doi: 10.1016/S0301-679X(00)00042-6.

[15] F. Elasha, C. Ruiz-Cárcel, D. Mba, G. Kiat, I. Nze, and G. Yebra, “Pitting detection in worm gearboxes with vibration analysis,” *Engineering Failure Analysis*, vol. 42, pp. 366–376, Jul. 2014, doi: 10.1016/j.engfailanal.2014.04.028.

[16] S. Li and A. Kahraman, “A fatigue model for contacts under mixed elastohydrodynamic lubrication condition,” *International Journal of Fatigue*, vol. 33, no. 3, pp. 427–436, Mar. 2011, doi: 10.1016/j.ijfatigue.2010.09.021.

[17] F. K. Choy, V. Polyshchuk, J. J. Zakrajsek, R. F. Handschuh, and D. P. Townsend, “Analysis of the effects of surface pitting and wear on the vibration of a gear transmission system,” *Tribology International*, vol. 29, no. 1, pp. 77–83, Feb. 1996, doi: 10.1016/0301-679X(95)00037-5.

[18] F. Chaari, W. Baccar, M. S. Abbes, and M. Haddar, “Effect of spalling or tooth breakage on gearmesh stiffness and dynamic response of a one-stage spur gear transmission,” *European Journal of Mechanics, A/Solids*, vol. 27, no. 4, pp. 691–705, Jul. 2008, doi: 10.1016/j.euromechsol.2007.11.005.

[19] X.-H. Liang, Z.-L. Liu, J. Pan, and M. J. Zuo, “Spur Gear Tooth Pitting Propagation Assessment Using Model-based Analysis,” *Chinese Journal of Mechanical Engineering*, vol. 30, no. 6, pp. 1369–1382, 2017, doi: 10.1007/s10033-017-0196-z.

[20] S. Li and A. Anisetti, “On the flash temperature of gear contacts under the tribo-dynamic condition,” *Tribology International*, vol. 97, pp. 6–13, May 2016, doi: 10.1016/j.triboint.2016.01.027.

[21] S. Li and A. Anisetti, “A tribo-dynamic contact fatigue model for spur gear pairs,” *International Journal of Fatigue*, vol. 98, pp. 81–91, May 2017, doi: 10.1016/j.ijfatigue.2017.01.020.

[22] S. Li, A. Kahraman, and M. Klein, “A Fatigue Model for Spur Gear Contacts Operating Under Mixed Elastohydrodynamic Lubrication Conditions,” *Journal of Mechanical Design*, vol. 134, no. 4, Mar. 2012, doi: 10.1115/1.4005655.

[23] G. Hoffmann, R. H. Slattery, and F. G. Hanejko, “Crack Initiation and Propagation in RCF – A New Approach to Understanding Pitting Failure of Highly Loaded Gears,” Apr. 2006. doi: https://doi.org/10.4271/2006-01-0383.

[24] S. Li and A. Kahraman, “A fatigue model for contacts under mixed elastohydrodynamic lubrication condition,” *International Journal of Fatigue*, vol. 33, no. 3, pp. 427–436, Mar. 2011, doi: 10.1016/J.IJFATIGUE.2010.09.021.

[25] S. Li and A. Kahraman, “A mixed EHL model with asymmetric integrated control volume discretization,” *Tribology International*, vol. 42, no. 8, pp. 1163–1172, Aug. 2009, doi: 10.1016/J.TRIBOINT.2009.03.020.

[26] D. Zhu, N. Ren, and Q. J. Wang, “Pitting Life Prediction Based on a 3D Line Contact Mixed EHL Analysis and Subsurface von Mises Stress Calculation,” *Journal of Tribology*, vol. 131, no. 4, Sep. 2009, doi: 10.1115/1.3195040.

[27] D. Epstein, L. M. Keer, Q. J. Wang, H. S. Cheng, and D. Zhu, “Effect of Surface Topography on Contact Fatigue in Mixed Lubrication,” *Tribology Transactions*, vol. 46, no. 4, pp. 506–513, 2003, doi: 10.1080/10402000308982657.

[28] S. Li and A. Kahraman, “A Transient Mixed Elastohydrodynamic Lubrication Model for Spur Gear Pairs,” *Journal of Tribology*, vol. 132, no. 1, Nov. 2009, doi: 10.1115/1.4000270.

[29] M. R. Riggs, N. K. Murthy, S. P. Berkebile, and A. L. Korenyi-Both, “Scuffing Resistance and Starved Lubrication Behavior in Helicopter Gear Steels Coated with Nanocomposite Surface Coatings with and without a Hard Sublayer,” *Tribology Transactions*, vol. 63, no. 4, pp. 610–620, Jul. 2020, doi: 10.1080/10402004.2020.1725205.

[30] J. Enthoven and H. A. Spikes, “Infrared and Visual Study of the Mechanisms of Scuffing,” *Tribology Transactions*, vol. 39, no. 2, pp. 441–447, Jan. 1996, doi: 10.1080/10402009608983550.

[31] F. Ali, I. Křupka, and M. Hartl, “Analytical and experimental investigation on friction of non-conformal point contacts under starved lubrication,” *Meccanica*, vol. 48, no. 3, pp. 545–553, 2013, doi: 10.1007/s11012-012-9614-6.

[32] S. R. Lewis, R. Lewis, G. Evans, and L. E. Buckley-Johnstone, “Assessment of railway curve lubricant performance using a twin-disc tester,” *Wear*, vol. 314, no. 1–2, pp. 205–212, Jun. 2014, doi: 10.1016/J.WEAR.2013.11.033.

[33] E. Querlioz, F. Ville, H. Lenon, and T. Lubrecht, “Experimental investigations on the contact fatigue life under starved conditions,” *Tribology International*, vol. 40, no. 10–12, pp. 1619–1626, Oct. 2007, doi: 10.1016/J.TRIBOINT.2006.11.002.

[34] A. Labiau, F. Ville, P. Sainsot, E. Querlioz, and T. Lubrecht, “Effect of sinusoidal surface roughness under starved conditions on rolling contact fatigue,” *Proceedings of the Institution of Mechanical Engineers, Part J: Journal of Engineering Tribology*, vol. 222, no. 3, pp. 193–200, 2008, doi: 10.1243/13506501JET326.

[35] B. J. Hamrock and D. Dowson, “Isothermal Elastohydrodynamic Lubrication of Point Contacts: Part III—Fully Flooded Results,” *Journal of Lubrication Technology*, vol. 99, no. 2, pp. 264–275, Apr. 1977, doi: 10.1115/1.3453074.

[36] P. Yang, J. Wang, and M. Kaneta, “Thermal and Non-Newtonian Numerical Analyses for Starved EHL Line Contacts,” *Journal of Tribology*, vol. 128, no. 2, pp. 282–290, Jul. 2005, doi: 10.1115/1.2164465.

[37] W. Pu, D. Zhu, and J. Wang, “A Starved Mixed Elastohydrodynamic Lubrication Model for the Prediction of Lubrication Performance, Friction and Flash Temperature With Arbitrary Entrainment Angle,” *Journal of Tribology*, vol. 140, no. 3, Oct. 2017, doi: 10.1115/1.4037844.

[38] S. Li and D. Masse, “On the flash temperature under the starved lubrication condition of a line contact,” *Tribology International*, vol. 136, pp. 173–181, Aug. 2019, doi: 10.1016/J.TRIBOINT.2019.03.038.

[39] H. G. Elrod, “A Cavitation Algorithm,” *Journal of Lubrication Technology*, vol. 103, no. 3, pp. 350–354, Jul. 1981, doi: 10.1115/1.3251669.

[40] S. Li, A. Kahraman, N. Anderson, and L. D. Wedeven, “A model to predict scuffing failures of a ball-on-disk contact,” *Tribology International*, vol. 60, pp. 233–245, Apr. 2013, doi: 10.1016/J.TRIBOINT.2012.11.007.

[41] S. Li and A. Kahraman, “A scuffing model for spur gear contacts,” *Mechanism and Machine Theory*, vol. 156, p. 104161, Feb. 2021, doi: 10.1016/J.MECHMACHTHEORY.2020.104161.

[42] S. Li, “A thermal tribo-dynamic mechanical power loss model for spur gear Pairs,” *Tribology International*, vol. 88, pp. 170–178, Aug. 2015, doi: 10.1016/j.triboint.2015.03.022.

[43] S. Li, “LUBRICATION AND CONTACT FATIGUE MODELS FOR.”

[44] X. Ai and L. Zheng, “A General Model for Microelastohydrodynamic Lubrication and Its Full Numerical Solution,” *Journal of Tribology*, vol. 111, no. 4, pp. 569–576, Oct. 1989, doi: 10.1115/1.3261979.

[45] X. Ai, H. S. Cheng, and L. Zheng, “A Transient Model for Micro-Elastohydrodynamic Lubrication With Three-Dimensional Irregularities,” *Journal of Tribology*, vol. 115, no. 1, pp. 102–110, Jan. 1993, doi: 10.1115/1.2920961.

[46] X. Ai, “Numerical analyses of elastohydrodynamically lubricated line and point contacts with rough surfaces by using semi-system and multigrid methods (volumes 1 and 2),” Northwestern Univ., Evanston, IL., 1993.

[47] Y.-Z. Hu and D. Zhu, “A Full Numerical Solution to the Mixed Lubrication in Point Contacts,” *Journal of Tribology*, vol. 122, no. 1, pp. 1–9, Jun. 1999, doi: 10.1115/1.555322.

[48] Y. Z. Hu, H. Wang, W. Z. Wang, and D. Zhu, “A computer model of mixed lubrication in point contacts,” *Tribology International*, vol. 34, no. 1, pp. 65–73, Jan. 2001, doi: 10.1016/S0301-679X(00)00139-0.

[49] S. Li, “LUBRICATION AND CONTACT FATIGUE MODELS FOR ROLLER AND GEAR CONTACTS.” [Online]. Available: http://rave.ohiolink.edu/etdc/view?acc_num=osu1234822355

[50] P. M. Cann, “Starved Grease Lubrication of Rolling Contacts,” *Tribology Transactions*, vol. 42, no. 4, pp. 867–873, 1999, doi: 10.1080/10402009908982294.

[51] S. Li and A. Kahraman, “A Transient Mixed Elastohydrodynamic Lubrication Model for Spur Gear Pairs,” *Journal of Tribology*, vol. 132, no. 1, Nov. 2009, doi: 10.1115/1.4000270.

[52] S. Bair, “Comment on ‘new experimental data and reference models for the viscosity and density of squalane,’” *Journal of Chemical and Engineering Data*, vol. 60, no. 4, pp. 1211–1212, Apr. 2015, doi: 10.1021/JE501147A.

[53] K. A. G. Schmidt, D. Pagnutti, and J. P. M. Trusler, “Reply to ‘Comment on “New Experimental Data and Reference Models for the Viscosity and Density of Squalane,”’” *Journal of Chemical and Engineering Data*, vol. 60, no. 4, pp. 1213–1214, Apr. 2015, doi: 10.1021/ACS.JCED.5B00157.

[54] S. Li and A. Anisetti, “A tribo-dynamic contact fatigue model for spur gear pairs,” *International Journal of Fatigue*, vol. 98, pp. 81–91, May 2017, doi: 10.1016/J.IJFATIGUE.2017.01.020.

[55] K. L. Johnson and K. L. Johnson, *Contact mechanics*. Cambridge university press, 1987.

[56] S. Li, A. Kahraman, and M. Klein, “A Fatigue Model for Spur Gear Contacts Operating Under Mixed Elastohydrodynamic Lubrication Conditions,” *Journal of Mechanical Design*, vol. 134, no. 4, Mar. 2012, doi: 10.1115/1.4005655.

[57] S. Li, “A boundary element model for near surface contact stresses of rough surfaces,” *Computational Mechanics*, vol. 54, no. 3, pp. 833–846, 2014, doi: 10.1007/s00466-014-1037-x.

[58] T. MATAKE, “An Explanation on Fatigue Limit under Combined Stress,” *Bulletin of JSME*, vol. 20, no. 141, pp. 257–263, 1977, doi: 10.1299/jsme1958.20.257.

[59] D. L. McDiarmid, “A SHEAR STRESS BASED CRITICAL-PLANE CRITERION OF MULTIAXIAL FATIGUE FAILURE FOR DESIGN AND LIFE PREDICTION,” *Fatigue & Fracture of Engineering Materials & Structures*, vol. 17, no. 12, pp. 1475–1484, 1994, doi: https://doi.org/10.1111/j.1460-2695.1994.tb00789.x.

[60] P. LAZZARIN and L. SUSMEL, “A stress-based method to predict lifetime under multiaxial fatigue loadings,” *Fatigue & Fracture of Engineering Materials & Structures*, vol. 26, no. 12, pp. 1171–1187, 2003, doi: https://doi.org/10.1046/j.1460-2695.2003.00723.x.

[61] Y. Liu and S. Mahadevan, “A unified multiaxial fatigue damage model for isotropic and anisotropic materials,” *International Journal of Fatigue*, vol. 29, no. 2, pp. 347–359, Feb. 2007, doi: 10.1016/J.IJFATIGUE.2006.03.011.

[62] E. v Zaretsky, “Fatigue Criterion to System Design, Life and Reliability-A Primer.”

[63] D. Zhu, N. Ren, and Q. J. Wang, “Pitting Life Prediction Based on a 3D Line Contact Mixed EHL Analysis and Subsurface von Mises Stress Calculation,” *Journal of Tribology*, vol. 131, no. 4, Sep. 2009, doi: 10.1115/1.3195040.

[64] D. Epstein, L. M. Keer, Q. J. Wang, H. S. Cheng, and D. Zhu, “Effect of Surface Topography on Contact Fatigue in Mixed Lubrication,” *Tribology Transactions*, vol. 46, no. 4, pp. 506–513, 2003, doi: 10.1080/10402000308982657.

[65] S. Li and A. Kahraman, “Micro-pitting fatigue lives of lubricated point contacts: Experiments and model validation,” *International Journal of Fatigue*, vol. 48, pp. 9–18, Mar. 2013, doi: 10.1016/J.IJFATIGUE.2012.12.003.

[66] Y. Liu and S. Mahadevan, “A unified multiaxial fatigue damage model for isotropic and anisotropic materials,” *International Journal of Fatigue*, vol. 29, no. 2, pp. 347–359, Feb. 2007, doi: 10.1016/J.IJFATIGUE.2006.03.011.

[67] G. Fajdiga and M. Sraml, “Fatigue crack initiation and propagation under cyclic contact loading,” *Engineering Fracture Mechanics*, vol. 76, no. 9, pp. 1320–1335, Jun. 2009, doi: 10.1016/J.ENGFRACMECH.2009.02.005.

[68] A. Yoshida, Y. Ohue, and H. Ishikawa, “Diagnosis of tooth surface failure by wavelet transform of dynamic characteristics,” *Tribology International*, vol. 33, no. 3–4, pp. 273–279, Apr. 2000, doi: 10.1016/S0301-679X(00)00042-6.

[69] S. Bair and W. O. Winer, “A New High-Pressure, High-Shear Stress Viscometer and Results for Lubricants,” *Tribology Transactions*, vol. 36, no. 4, pp. 721–725, 1993, doi: 10.1080/10402009308983216.

[70] S. BAIR, “A Rough Shear-Thinning Correction for EHD Film Thickness,” *Tribology Transactions*, vol. 47, no. 3, pp. 361–365, 2004, doi: 10.1080/05698190490455519.

[71] S. Li and D. Masse, “On the flash temperature under the starved lubrication condition of a line contact,” *Tribology International*, vol. 136, pp. 173–181, Aug. 2019, doi: 10.1016/J.TRIBOINT.2019.03.038.

[72] M. J. Handschuh, S. Li, A. Kahraman, and D. Talbot, “An Experimental–Theoretical Methodology to Develop Scuffing Limits for Relatively Smooth High-Speed Contacts,” *Tribology Transactions*, vol. 63, no. 5, pp. 781–795, 2020, doi: 10.1080/10402004.2020.1715519.

[73] S. Li and A. Kahraman, “A scuffing model for spur gear contacts,” *Mechanism and Machine Theory*, vol. 156, p. 104161, Feb. 2021, doi: 10.1016/J.MECHMACHTHEORY.2020.104161.

[74] S. Li and A. Kahraman, “A fatigue model for contacts under mixed elastohydrodynamic lubrication condition,” *International Journal of Fatigue*, vol. 33, no. 3, pp. 427–436, Mar. 2011, doi: 10.1016/J.IJFATIGUE.2010.09.021.

[75] E. Querlioz, F. Ville, H. Lenon, and T. Lubrecht, “Experimental investigations on the contact fatigue life under starved conditions,” *Tribology International*, vol. 40, no. 10–12, pp. 1619–1626, Oct. 2007, doi: 10.1016/J.TRIBOINT.2006.11.002.

[76] S. R. Lewis, R. Lewis, G. Evans, and L. E. Buckley-Johnstone, “Assessment of railway curve lubricant performance using a twin-disc tester,” *Wear*, vol. 314, no. 1–2, pp. 205–212, Jun. 2014, doi: 10.1016/J.WEAR.2013.11.033.

[77] F. Chevalier, A. A. Lubrecht, P. M. E. Cann, F. Colin, and G. Dalmaz, “Film Thickness in Starved EHL Point Contacts,” *Journal of Tribology*, vol. 120, no. 1, pp. 126–133, Jan. 1998, doi: 10.1115/1.2834175.

[78] P. Svoboda, D. Kostal, I. Krupka, and M. Hartl, “Experimental study of starved EHL contacts based on thickness of oil layer in the contact inlet,” *Tribology International*, vol. 67, pp. 140–145, Nov. 2013, doi: 10.1016/J.TRIBOINT.2013.07.019.

[79] S. Li and D. Masse, “On the flash temperature under the starved lubrication condition of a line contact,” *Tribology International*, vol. 136, pp. 173–181, Aug. 2019, doi: 10.1016/J.TRIBOINT.2019.03.038.

[80] S. Li, A. Kolivand, and J. Wei, “Determination of Critical Temperature of Scuffing for AISI 8620 Steel Gear Contacts Lubricated by Dexron 6 Through Computational Simulation of Experiment,” *Journal of Tribology*, vol. 144, no. 8, Feb. 2022, doi: 10.1115/1.4053702.